

Study of Nonlinear Optical Effects in Silicon Waveguides

by

Lianghong Yin

Submitted in Partial Fulfillment

of the

Requirements for the Degree

Doctor of Philosophy

Supervised by

Professor Govind P. Agrawal

The Institute of Optics
Arts, Sciences and Engineering
Edmund A. Hajim School of Engineering and Applied Sciences

University of Rochester
Rochester, New York

2009

Curriculum Vitae

The author was born in Xuancheng, Anhui, China in August 1978. Her most favorite course was Nature in primary school, and Physics in high school. She began her undergraduate studies in September 1995 in the Physics department at Anqing Teachers College, Anqing, Anhui, China, and received her Bachelor of Science degree in Physics with high honors in July 1999. She began her graduate studies in September 1999 in the Physics department at the University of Science and Technology of China, Hefei, Anhui, China. Her research was to build donut-mode optical tweezers and compare their mechanical properties with those of Gaussian-mode optical tweezers. She received her Master of Science degree in Optics in July 2002. She then started her doctoral studies in January 2003 in the Institute of Optics at the University of Rochester, Rochester, NY, USA. She has carried out her doctoral research under the supervision of Professor Govind P. Agrawal since June 2004. Her research interests focus on nonlinear silicon photonics, nonlinear optics, ultrafast optics, waveguide optics, mode-locked fiber lasers, and optical communications. She will receive her Ph. D. degree in Optics in March 2010.

Publications

Journal Articles

L. Yin, J. Zhang, P. M. Fauchet, and G. P. Agrawal, "Optical switching using nonlinear polarization rotation inside silicon waveguides," *Opt. Lett.* **34**, 476–478 (2009)

L. Yin and G. P. Agrawal, "Impact of two-photon absorption on self-phase modulation in silicon waveguides," *Opt. Lett.* **32**, 2031–2033 (2007).

L. Yin, Q. Lin, and G. P. Agrawal, "Soliton fission and continuum generation in silicon waveguides," *Opt. Lett.* **32**, 391–393 (2007).

L. Yin, Q. Lin, and G. P. Agrawal, "Dispersion tailoring and soliton propagation in silicon waveguides," *Opt. Lett.* **31**, 1295–1297 (2006).

L. Yin, Y. Li, L. Lou, Da Zhang, and H. Chen, "Experimental Research of Donut Mode, a New Kind of Optical Trap," *Chinese Journal of Lasers* **30**, 211–215 (2003).

L. Yin, Y. Li, L. Lou, and Da Zhang, "Multiple Methods of Forming Ring Optical Trap and the Resultant Comparison," *Chinese Journal of Lasers* **A29**, 678–680 (2002).

Presentations

L. Yin, J. Lee, P. M. Fauchet, and G. P. Agrawal, “Realization of an Ultrafast Silicon Kerr Switch,” in *Frontiers in Optics*, OSA Technical Digest (CD) (Optical Society of America, 2009), paper FML4.

J. Lee, **L. Yin**, G. P. Agrawal, and P. M. Fauchet, “Ultrafast Kerr Switching in a Silicon Waveguide,” in *The 6th International Conference on Group IV Photonics*, IEEE Photonics Society, Sept 2009, paper ThC3.

L. Yin, J. Zhang, P. M. Fauchet, and G. P. Agrawal, “Design of an Optical Kerr Shutter Using Silicon Waveguides,” in *Frontiers in Optics*, OSA Technical Digest (CD) (Optical Society of America, 2008), paper FThF3.

G. P. Agrawal, **L. Yin**, J. Zhang, and P. M. Fauchet, “Nonlinear Silicon Photonics,” invited presentation in *The 15th annual Symposium of European Materials Research Society*, Strassbourg, France, May 16, 2008.

L. Yin, Q. Lin, and G. P. Agrawal, “Soliton Fission and Continuum Generation in Silicon Waveguides,” in *Frontiers in Optics*, OSA Technical Digest (CD) (Optical Society of America, 2006), paper FWM5.

L. Yin, Q. Lin, and G. P. Agrawal, “Dispersion Tailoring and Soliton Propagation in Si Waveguides,” in *Conference on Lasers and Electro-Optics/Quantum Electronics and Laser Science Conference and Photonic Applications Systems*

Technologies, Technical Digest (CD) (Optical Society of America, 2006), paper CMEE7.

L. Yin, J. Bently, “The Design of a CCD Barcode Reader Imaging Lens System for an Improved Depth of Field,” OPT 444 Lens Design final project, 2004.

Acknowledgements

University of Rochester is the school where I have spent more than six years studying. It's the longest so far and may even be so eventually. The previous record was Xuancheng middle school where I spent two months less than six years. Six-year of study at the Institute of Optics is such a precious experience that has trained me from a young student into a researcher. This change into maturity is so vivid that I feel it and can even touch it. I am so grateful toward the legacy of the Institute, toward all the professors, staff, and students that have made it such a wonderful palace for pursuing and creating knowledge.

I would like to express my gratitude specifically to these who helped me to complete this thesis. First and foremost, I would like to thank my advisor, Professor Govind P. Agrawal. His encyclopedic knowledge of fiber optics, numerical techniques, and scientific literature is a great asset to us. He introduced me to this wonderful field of nonlinear optics in guided mode. He gave me the freedom to do whatever I am interested in. It's very interesting that he also introduced me to new programming languages and software packages. One legacy of his group is that everyone writes beautifully in Latex. He encourages me to set up equipment in the lab, he also helps me to figure out my problems in the lab. He not only teaches me how to do scientific research, but he also teaches me how to think and write coherently. His serious and scientific attitude always drives me to understand more of the physical essence of the research I do. This thesis is another accomplishment of his.

Many thanks to Professor Fauchet for guidance and supervision in my research. I should give very big thanks to Jonathan Y. Lee. We collaborated wonderfully in the lab. He brought a lot of the equipment together with Labview programs into the lab. He put in a lot of efforts in optimizing the fabrication of the waveguides we use for the experiments. Special thanks to Jidong Zhang. We had wonderful cooperation. I wouldn't be able to do any meaningful experiment without their cooperations. I would also thank Qiang Lin for his broad knowledge and helpful discussions. He, Nick Usechak and Fatih Yaman were extremely helpful when they read papers and discussed problems in our group meetings. I also thank Doctor George, Wanli Chi, and Kaiqin Chu for letting me use their equipment. Thank Professor Zavislan, Zhao Wang, and Christopher Glazowski for letting me use their silicon APD to set up the optical autocorrelator. I am very grateful to Professor Wayne H. Knox for his invaluable advice about academic careers, for his inspiring discussions about research. Thank Liping Cui and Li Ding for letting me use their equipments. And Thank Liping for discussion of research problems that enables me to practice my knowledge in four-wave mixing and supercontinuum generation. Thank Prashant Baveja, Brian Daniel, and Yuzhe Xiao, they are very nice groupmates to work with.

I am also indebted to all these professors for serving as my references during my search for a postdoctoral position. They are Professors Agrawal, Fauchet, and Wicks. Many thanks to Professors Brown, Fauchet, and Wicks for being my committee members.

I greatly appreciate the help that the staff in the Institute of Optics have provided during my graduate studies. I thank Gina Kern, Lissa Cotter, Betsy Benedict, Gayle Thompson, Marie Banach, Noelene Votens, Brian McIntyre, Lori Russell, and Joan Christian for their help. In particular, I would like to thank Per Adamson for his tremendous support with much of the equipment.

Finally, I would like to thank my parents, sisters, and brother, who have given me their continuous and unconditional love, support and encouragement. I would like to

thank my husband's parents Cindy and Bob Easterly for their love and perpetual support. They helped to print out my thesis in color. I would like to thank my husband Dan Easterly for all of his love and support. He also proof read this thesis.

Abstract

This thesis is devoted to investigate optical properties of silicon-on-insulator (SOI) waveguides with an emphasis on third-order nonlinearities of silicon waveguides. The objective is to understand the nonlinear effects inside SOI waveguides, the possible applications of SOI waveguides, and the intrinsic difficulties this structure faces for some of the real applications. We first discuss the types of SOI waveguides used in our laboratory, and present the measurements of propagation loss, total insertion loss and coupling loss using Fabry-Perot resonances, cutback, and scattering methods. Three mathematical tools for calculating the modes and dispersion properties of SOI waveguides are compared from the standpoint of accuracy and efficiency. The importance of dispersion tailoring of SOI waveguides in order to realize anomalous dispersion at wavelength around $1.5 \mu\text{m}$, and the possibility of soliton propagation in such a tailored waveguide are discussed next. Chapter 5 provides a general theoretical model for pulse propagation inside an SOI waveguide. The general formalism includes both the electronic and Raman responses. The self-phase modulation process in SOI waveguides is discussed next with an emphasis on the effects of two-photon absorption and the consequent free-carrier effects. The maximum allowed repetition rate of pulse trains is presented to serve as a general guideline of using self-phase modulation effect in real situations. We also present our experimental work on self-phase modulation in an SOI waveguide for both the TE and TM modes. In chapter 7 we describe supercontinuum generation in SOI waveguides from a theoretical standpoint. We next consider cross-phase modulation and nonlinear polarization rotation for realizing an SOI-waveguide

based optical Kerr shutter. The theoretical work is given first followed with our experimental results that show successful all-optical switching of a CW probe light by a pulsed pump light. Sub-pico-second switching window is realized using this switching scheme. The last chapter deals with the laser sources we used in our experiments with SOI waveguides, and discusses the measurements of pulse widths.

Table of Contents

Curriculum Vitae	ii
Publications	iii
Acknowledgements	vi
Abstract	ix
List of Tables	xv
List of Figures	xvi
1 Introduction	1
1.1 Historical Review of Previous Work	2
1.1.1 Structures for Making SOI Waveguides	2
1.1.2 Low-loss SOI Waveguide Manufacturing	4
1.1.3 Linear Applications	6
1.1.4 Nonlinear Applications	8
1.2 Thesis Objective	10
1.3 Thesis Outline	10

2	Waveguide Structure and Linear Loss Measurements	12
2.1	Waveguides Used in the Laboratory	12
2.2	Loss Measurements	14
2.2.1	Fabry-Perot Resonances	15
2.2.2	Cutback Method	17
2.2.3	Scattered Light Measurement	18
2.3	Specialty of Inverse Tapering for SOI Waveguides	20
2.4	Summary	22
3	Mode and Dispersion Calculations	23
3.1	Material Dispersion of Silicon	23
3.2	Methods for Calculating Waveguide Modes	25
3.2.1	FDFD Mode Solver	26
3.2.2	Finite-Difference Beam Propagation Method	28
3.2.3	Effective Index Method	32
3.3	Summary	34
4	Dispersion Tailoring and Soliton Propagation	36
4.1	Dispersion Tailoring	36
4.2	Soliton Propagation	40
4.3	Summary	43
5	Theoretical Framework for Nonlinear Interactions in Silicon Waveguides	44
5.1	General Formalism	44
5.2	Stimulated Raman Scattering	48
5.3	Nonlinear Refractive Index of Silicon	51
5.4	Summary	52

6	Self-phase Modulation in the Presence of Two-Photon Absorption	53
6.1	Self-phase Modulation: Theoretical	54
6.1.1	Theoretical Model	54
6.1.2	Single-Pulse Approximation	55
6.1.3	Pulse Trains with Different Repetition Rates	59
6.2	Self-phase Modulation: Experimental	61
6.3	Summary	66
7	Supercontinuum Generation	67
7.1	Physics of Supercontinuum Process	67
7.2	Dispersion Properties	70
7.3	Numerical Simulations	71
7.4	Experiment	75
7.5	Summary	75
8	Cross-phase Modulation and Nonlinear Polarization Rotation	77
8.1	Implementation of a Kerr Shutter	78
8.2	Theoretical Analysis	79
8.3	Numerical Simulations	81
8.4	Experimental Realization of a Silicon Kerr Shutter	85
8.5	Experiments with Optimized SOI waveguides	89
8.6	Summary	92
9	Mode-locked Fiber Laser and Pulse Width Measuring	94
9.1	Home-Built Mode-locked Fiber Laser	94
9.2	Pulse-Width Measured using Auto-Correlation	98

9.2.1	Interferometric Auto-Correlation using TPA inside Si APD . . .	99
9.2.2	Intensity Auto-Correlation using SHG	101
9.3	Summary	103
10	Summary	104
	Bibliography	106

List of Tables

2.1	Measurements of propagation losses for three normally tapered waveguides using the method of Fabry-Perot resonances.	17
2.2	Measurements of coupling losses and propagation losses for waveguides with normal tapering using the combination of cutback method and Fabry-Perot resonances.	19
5.1	Measurements of n_2 , β_{TPA} and the corresponding nonlinear figure of merit of silicon by different research groups.	52
6.1	The relationship between the driving current of the EDFA and the estimated input power at the input end of the SOI waveguide.	63
9.1	The correspondence between the driving current of the EDFA and the estimated FWHM of the pulses.	102

List of Figures

1.1	Four configurations for making waveguides in silicon: (a) Channel waveguides; (b) Rib waveguides; (c) Photonic-crystal waveguides; (d) Slot waveguides. (From Ref. [3].)	3
1.2	Schematic of a slot SOI waveguide. The slot is filled with air. The TE mode is strongly confined in the low-index slot region. (From Ref. [10].)	4
1.3	Schemes for fiber-to-waveguide coupling: (a) Edge coupling; (b) Normal taper; (c) Inverse taper; (d) Schematic of a mode-field converter; (e) SEM image of a mode-field converter. (From Ref. [3].)	6
2.1	(a) SEM (scanning electron microscope) picture of one of the channel waveguides used in the laboratory. (b) Microscope image of a ridge waveguide used in the laboratory, the normal tapering feature is visible.	13
2.2	Diagram of a single-mode tapered fiber lens. (From Ref. [48].)	14
2.3	F-P resonance for three waveguides (2, 3, and 4 mm long) with normal tapering. Blue curves are for TE modes and red curves are for TM modes; dotted curves are measurements and solid curves are numerical fits to the transmission equation Eq. (2.1).	16

2.4	Measurements of total insertion loss using cutback method. Discrete points are measured data, curves are fitting for the corresponding data points using the relationship of total insertion loss (dB) is equal to coupling loss (dB) plus propagation loss (dB/cm) times waveguide length (cm).	18
2.5	Log-scale intensity of light scattered vertically from the SOI waveguide for TM (red curves) and TE (blue curves) polarized light. Propagation losses are estimated by linear curve fitting technique.	20
2.6	Fabry-Perot resonances for three waveguides with inverse tapering. The first waveguide is 2 mm long with a facet width of 100 nm; the second waveguide is 3 mm long with a facet width of 200 nm; the third waveguide is 4 mm long with a facet width of 300 nm.	21
2.7	An interference pattern seen from the scattering of TE mode propagation inside an inversely tapered waveguide.	21
3.1	Sketch of an SOI rib waveguide fabricated on the (1 0 0) surface of the silicon crystal.	27
3.2	Field profiles for the fundamental (a) quasi-TE and (b) quasi-TM modes. All of the six field components of the electromagnetic field are shown.	28
3.3	Calculation of dispersion for a waveguide with width $W = 1 \mu\text{m}$, height $H = 0.6 \mu\text{m}$, and etch thickness $h = 0.3 \mu\text{m}$	29
3.4	Field profiles for the fundamental (a) quasi-TE and (b) quasi-TM modes.	30
3.5	Calculation of dispersion for a waveguide with width $W = 1 \mu\text{m}$, height $H = 0.6 \mu\text{m}$, and etch thickness $h = 0.3 \mu\text{m}$	31
3.6	Calculation of dispersions for a waveguide with width $W = 1 \mu\text{m}$, height $H = 0.6 \mu\text{m}$, and etch thickness $h = 0.3 \mu\text{m}$ using 1D effective index method.	33

3.7	Calculation of dispersions for a waveguide with width $W = 1 \mu\text{m}$, height $H = 0.6 \mu\text{m}$, and etch thickness $h = 0.3 \mu\text{m}$ using 2D effective index method.	33
4.1	Modal refractive indices of the TE_0 (dashed line) and TM_0 (solid line) modes for $W = 1.5 \mu\text{m}$, $H = 1.55 \mu\text{m}$, and $h = 0.7 \mu\text{m}$. The material dispersion of silicon is shown by a dashed line.	38
4.2	Dependence of ZDWL on (a) W , (b) H , and (c) h for the TE_0 (dotted lines) and TM_0 (solid lines) modes; (d) Contours of optimum h in the range of 0.3 to 1.1 μm in W - H plane for the TM_0 mode.	39
4.3	Contours of constant ZDWL as a function of W and H in the range of $\lambda_0 = 1.4$ to 2 μm ; etch thickness h is optimized for each set of W and H and is in the range of $h/H = 0.4$ to 0.8.	40
4.4	Output (a) pulse shape and (b) spectrum with different loss mechanisms included, third order dispersion is included in all cases; dotted curves show input profiles. The curve marked path-averaged shows that the loss-induced pulse broadening can be compensated to some degree by increasing the input peak power suitably.	42
5.1	Raman spectrum of crystalline silicon. The experimental data also shows high-order Raman scattering. (From Ref. [74].)	49
5.2	Real part and Imaginary part of $H_R(\frac{\Omega}{2\pi})$	50
6.1	Reduction in nonlinear phase shift at the pulse center because of TPA inside a silicon waveguide for $\phi_{\text{max}} = \pi$, 2π , and 3π . The inset shows ϕ_0 as a function of ϕ_{max} using $r = 0.25$; dashed curve shows the $r = 0$ case.	56

- 6.2 SPM-broadened pulse spectra (solid curves) at the end of a 2-cm-long SOI waveguide at three input intensities such that $\phi_{\max} = 1.5\pi, 7.5\pi,$ and 15.5π . Dashed curves include TPA but neglect FCA and FCD effects; dotted curves neglect TPA as well. The nonlinear phase profiles in the three situations are shown in the last plot for $\phi_{\max} = 15.5\pi$ 58
- 6.3 Pulse spectra at the same three intensity levels as in Fig. 6.2 except that all effects are included and three repetition rates are considered. The nonlinear phase shift at three different repetition rates is shown in part (d) at $I_0 = 12.5 \text{ GW/cm}^2$ 60
- 6.4 Experimental setup for SPM. A 50-cm long tapered fiber lens is used for coupling light into the waveguide. A polarization controller placed on the input side of the tapered fiber is used to control the input as a TE mode or a TM mode of the SOI waveguide. Another setup on the other side of the waveguide is for the purpose of testing if the input is a TE mode or a TM mode. 62
- 6.5 SPM spectra at low input power levels. SPM experiment using a 35-cm long tapered fiber lens for coupling: (a) Spectrum after the EDFA and the 35-cm long fiber; (b) Spectrum after the SOI waveguide. 63
- 6.6 SPM spectra at low input power levels. SPM experiment using a 50-cm long fiber lens for coupling: (a) Spectrum after the EDFA of the laser source; (b) Spectrum after the EDFA and the 50-cm long single mode fiber; (c) Spectrum of TE mode after the SOI waveguide; (d) Spectrum of TM mode after the SOI waveguide. 64
- 6.7 SPM spectra when the driving current is 500 mA. solid red line: spectrum after the 3-mm SOI waveguide in TM mode using the 50-cm long fiber; solid blue line: spectrum after the 3-mm SOI waveguide in TE mode using the 50-cm long fiber. 65

7.1	Wavelength dependence of n_{Si} (dotted), n_{eff} (dashed), and β_2 (solid) for the fundamental TE mode using the waveguide shown in the inset with $W = 0.8 \mu\text{m}$, and $H = 0.7 \mu\text{m}$	71
7.2	Temporal and spectral profiles at the output of 1.2-cm-long SOI waveguide when a 50-fs pulse propagates as a third order soliton. Dotted curves shows, for comparison, the corresponding input profiles.	74
7.3	Supercontinuum created in a 3-mm long SOI waveguide under the conditions of Fig. 7.2. The dashed curve shows the spectrum when the effects of TPA and FCA are ignored. The dotted curve shows the input pulse spectrum.	75
7.4	SCG spectra at high input power levels. SCG experiment using a 50-cm long fiber lens for coupling: (a) Spectrum after the EDFA of the laser source; (b) Spectrum after the EDFA and the 50-cm long single mode fiber; (c) Spectrum of TE mode after the SOI waveguide; (d) Spectrum of TM mode after the SOI waveguide. Very broad spectra are obtained at high input power levels.	76
8.1	Schematic setup of the proposed optical Kerr shutter. The probe undergoes nonlinear polarization rotation inside the silicon waveguide when a pump pulse is present. An optical filter is used to block the pump light. A polarizer works as a polarization analyzer to set the transmission of the system in two output states.	79
8.2	Switching windows for 4 different pump-pulse widths. The thinner red curves mark the numerical results while the thicker blue curves show the analytical prediction neglecting the free-carrier effects.	82
8.3	Switching windows for the same 4 pump-pulse widths and the same operating conditions used in Fig. 8.2. The only difference is that a square-shape silicon waveguide is employed to minimize walk-off effects.	83

8.4	Nonlinear phase shift and switching windows at three different input peak powers of 3 W, 6 W, and 9 W in the case of using a square-shape waveguide ($400 \times 400 \text{ nm}^2$). The width of the pump pulses is 1 ps. . . .	84
8.5	Experimental setup used for realizing Kerr switching in silicon waveguides. EDFA: Er-doped fiber amplifier; PC: polarization controller; CWDM: coarse wavelength-division multiplexer.	85
8.6	Result of the experiment of a silicon Kerr shutter. The data show the readings of the output power of the CW signal in the oscilloscope in four different situations.	87
8.7	Result of the experiment of a silicon Kerr shutter. The data show the readings in the OSA in four different situations.	88
8.8	Result of the experiment of a silicon Kerr shutter. Measured oscilloscope traces of the probe output at ϕ_{\parallel} and ϕ_{\perp} using a 20-GHz optical sampling oscilloscope.	90
8.9	Switching amplitude as a function of input pump peak power at ϕ_{\parallel} and ϕ_{\perp} using a 20-GHz optical sampling oscilloscope: (a) Experiment results; (b) Numerical simulations at low input pump peak power.	91
8.10	Autocorrelation traces of the probe output at ϕ_{\perp} : (a) Experiment results; (b) Numerical simulations.	92
9.1	Setup of a mode-locked all-fiber erbium laser. The mode-locking scheme is nonlinear polarization rotation.	95
9.2	Spectra of the home-made mode-locked all-fiber erbium laser: (a) mode-locked at 1532 nm; (b) mode-locked at 1561 nm.	96
9.3	Figure of pulse-train from oscilloscope. The period of pulses is 119 ns.	97
9.4	Wavelength-dependence of the polarization state of the mode-locked all-fiber laser.	97

9.5	Spectrum of the commercial mode-locked fiber laser (Mercury 1000 by PolarOnyx).	98
9.6	TPA-based auto-correlation trace and its fit using Gaussian pulse shape: (a) Experiment data with a fitting envelope using Gaussian pulse shape with $T_0 = 560$ fs, 460 fs, and 360 fs; (b) Numerically simulated data with $T_0 = 460$ fs	100
9.7	SHG-based auto-correlation trace. The curves represent pulses after the EDFA with pumping current changing from 50 mA to 500 mA.	101

1 Introduction

Silicon is one of the fundamental materials in the semiconductor industry. The techniques to fabricate silicon-based electronic devices are mature and cheap for mass production. With the advances in fabricating silicon electronic devices, it is now possible to fabricate silicon photonic devices using the same complimentary-metal-oxide-semiconductor (CMOS) technology, especially with the help of the mature silicon-on-insulator (SOI) wafer technique and nano-scale photolithography. The fact that silicon photonics is truly CMOS compatible, and that silicon is transparent in the wide spectral regions extending from near to mid infrared, make it very promising for making passive and active opto-electronic components [1–9]. Recent research papers show that silicon photonics enables applications in optical interconnects, data communications, telecommunications, specialized signal processing, switched networks, imaging, displays, radio frequency/wireless photonics, electronic warfare, photonics for millimeter-wave/microwave/radio-frequency systems, laboratory-on-a-chip, medical diagnosis, spectrometer-on-a-chip, photonic sensing of chemical/biological/physical variables, sensor fusion, neural networks, bionics, analog-to-digital conversion, optical storage, optical logic, electro-optical logic, and testing of CMOS circuits [5].

Other than linear applications, several kinds of nonlinear optical effects have also been observed using silicon waveguides in recent years. Comparing with fused silica, silicon is promising for making nonlinear optical devices for five reasons. First, silicon

is transparent in the spectral region beyond $1.1 \mu\text{m}$ up to $6 \mu\text{m}$. Second, the refractive index of silicon (around 3.5) is much larger than that of fused silica ($n = 1.45$). This implies a much stronger light confinement inside SOI waveguides, which is beneficial for both nonlinear light interactions and for controlling the size of optical devices. Third, the nonlinear refractive index n_2 of silicon is about 200 times larger than that of silica. Fourth, the Raman gain coefficient of silicon is about 3000 times larger than that of silica, and is strongly polarization dependent. Fifth, SOI waveguides are CMOS technology compatible and enable low-cost large-scale integration. However, comparing with silica, silicon has some additional complications, such as two-photon absorption, free-carrier absorption, and free-carrier-induced change in the refractive index. Also, the polarization properties of silicon are different from silica because of its lattice structure. These aspects have been studied extensively and can be easily incorporated into our theoretical model.

1.1 Historical Review of Previous Work

1.1.1 Structures for Making SOI Waveguides

The widely used SOI waveguides may take the form of a channel waveguide, ridge waveguide, photonic-crystal waveguide, or slot waveguide, as shown in Fig. 1.1 [3]. Researchers use channel waveguides to reduce the sidewall roughness resulting in reduced propagation losses. However for a waveguide with thickness and width of $1 \mu\text{m}$ or more the number of modes will be large. For single-mode operation in an SOI waveguide, for example at a wavelength of $1.55 \mu\text{m}$, its dimensions need to be less than or close to 240 nm [2]. The rib waveguides are a little bit different. Calculations show that a large rib waveguide can be single-moded if its aspect ratio satisfies the following equation:

$$\frac{a}{b} \leq 0.3 + \frac{r}{\sqrt{1-r^2}}, \quad (1.1)$$

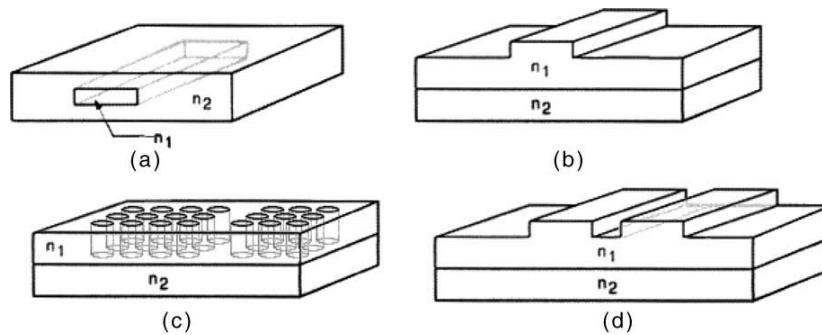


Figure 1.1: Four configurations for making waveguides in silicon: (a) Channel waveguides; (b) Rib waveguides; (c) Photonic-crystal waveguides; (d) Slot waveguides. (From Ref. [3].)

where a/b is the ratio between width and height, and $(1 - r)$ is the ratio of etch thickness and waveguide height. For a typical ridge waveguide where $r = 0.5$, the waveguide is single-mode as long as $a/b < 0.96$. A reasonable set of dimensions will be $b = 400$ nm, $a = 385$ nm. There are advantages of using rib waveguides. First, free carriers dissipate faster into the wings of the waveguide, which reduces the free-carrier effects. Second, a p-i-n structure with metal contacts is easily fabricated using this structure.

A photonic-crystal waveguide is another option for making SOI waveguides. The refractive indices of the left and right sides of the cladding in Fig. 1.1(c) can be flexibly engineered by varying the diameter of the holes and the lattice constants. The disadvantage is a high propagation loss due to the roughness of sidewalls. Recently, the slot waveguide has been proposed and fabricated as another candidate for silicon photonics [3, 10, 11]. In a slot waveguide, an ultra-thin low-refractive-index layer is sandwiched between two high-refractive-index layers, as shown in Fig. 1.2 [10]. In such a waveguide, the TE mode is strongly confined in the low-index slot region. Numerical simulations have demonstrated this abnormal light confinement. Fauchet's group at the University of Rochester has applied this structure in light-emission and bio-sensing areas [12, 13]. In one attempt, this research group built a multi-slot waveguide with alternating thin Si and SiO₂ layers, and proved that light was confined in the lower-index

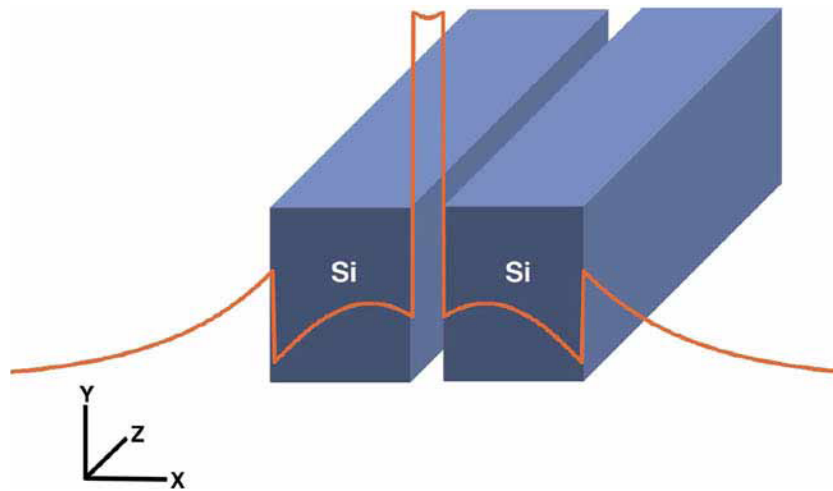


Figure 1.2: Schematic of a slot SOI waveguide. The slot is filled with air. The TE mode is strongly confined in the low-index slot region. (From Ref. [10].)

SiO_2 layers. This structure of slot waveguides combines the advantages of both silicon and silica to explore the promising nonlinear interactions of light in the waveguides, such as rare-earth material doping to provide optical gain [12]. In another attempt, they built a two-dimensional photonic-crystal slot microcavity sensor for virus-sized particle detection. The resonance of the cavity shifted when a particle was captured. Comparing with normal photonic crystal cavities, the slot cavity structure enhanced the sensitivity exponentially with the size of particles [13].

1.1.2 Low-loss SOI Waveguide Manufacturing

Silicon waveguides have great potential for use as nonlinear optical devices. However two manufacturing challenges are high propagation losses and high fiber-to-waveguide coupling losses [3, 4].

The main origin of the propagation loss in a silicon submicron waveguide is scattering at its sidewalls. By reducing the sidewall roughness, scattering losses can be reduced significantly. Lithography and etching are the keys to making a smooth silicon pattern. Researchers employ electron-beam lithography and plasma etching for the sil-

icon submicron-size waveguides. A relatively low propagation loss of 2.8 dB/cm for a $400 \text{ nm} \times 200 \text{ nm}$ core has been achieved [4]. An oxidation procedure can further improve the smoothness of sidewalls. For example, losses in channel waveguides typically range from 0.2 to 5 dB/cm. Losses in photonic crystal and slot waveguides are even higher. Rib waveguides have typically lower losses of less than 0.1 dB/cm due to their larger dimensions [3].

The most difficult problem with silicon waveguides is how to connect them to external circuits, where optical fibers are generally used. An SOI waveguide is very small, and its core is about 500 nm wide. On the other hand, the fundamental mode of single-mode fiber is about $9 \mu\text{m}$ in diameter. Moreover, the air gap between the facets causes interference and puts some wavelength dependent characteristics on top of the original spectra [4]. The coupling element can be either a microscope objective lens or a tapered fiber lens. The latter is widely used nowadays for convenience. The waveguide itself can be either un-tapered, or tapered with normal tapering or inverse tapering [3] as shown in Fig. 1.3. The advantage of inverse tapering is that the mode index at the narrow tip is much smaller than that of bulk silicon and the effective mode area is larger than that of the silicon region, both of which offer better mode matching and more efficient coupling. The disadvantages are that the coupling is very sensitive to environmental vibrations, and also a bigger portion of the optical field is propagating along the sidewalls so that scattering loss from the sidewalls is huge. Since the coupling of inverse tapering is not as stable as normal tapering, in our experiments, we used the waveguides with normal taperings.

Low-loss, low-reflection, mode-field converter can be used to solve the coupling problem even better. The converter has a silicon adiabatic taper that gradually becomes thinner toward the end, and a second low-index waveguide covers the taper. Coupling losses can be made as low as 0.5 dB per connection with this approach [4]. In our preliminary trial, mode-field converters improved the couplings significantly by reducing the coupling loss from around 20 dB to around 8 dB.

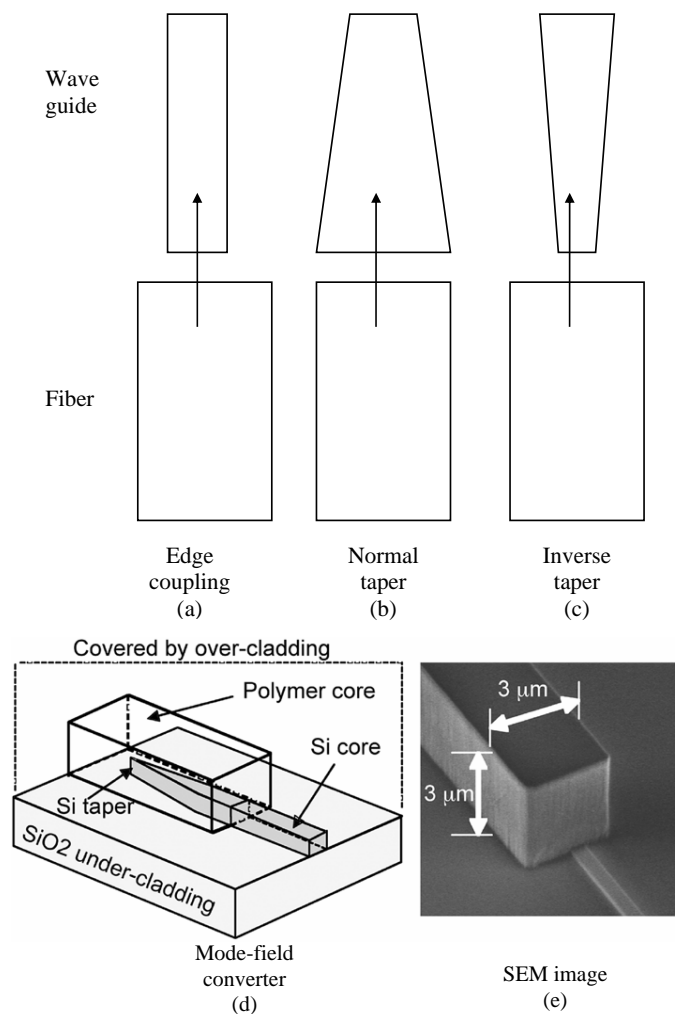


Figure 1.3: Schemes for fiber-to-waveguide coupling: (a) Edge coupling; (b) Normal taper; (c) Inverse taper; (d) Schematic of a mode-field converter; (e) SEM image of a mode-field converter. (From Ref. [3].)

1.1.3 Linear Applications

Using low-loss SOI waveguides, several passive devices have been demonstrated recently, including wavelength filters, multimode interference couplers, and WDM filters, etc [3,4]. These devices can be in the configuration of Mach–Zehnder interferometers, Bragg gratings, ring resonators and photonic crystal waveguides.

Other than passive devices, active devices have also been demonstrated to control

the flow of light, including modulators and switches. The basic idea is to change the transmission properties of the device through a change in the refractive index. Modulation of the refractive index of silicon can be done using either the thermo-optic effect or the electro-optic effect. However, the thermo-optic effect is relatively slow and can only be used for up to 1-MHz modulation frequencies [3]. For high-speed modulation, electro-optic devices are required. However, pure crystalline silicon does not exhibit a linear electro-optic (Pockels) effect. An effective mechanism for changing the refractive index in silicon at a high speed is the free-carrier plasma-dispersion effect. The refractive index of silicon varies with the free-carrier concentration, which can be manipulated through injecting or depleting carriers by applying an electric field to the device. However, free-carrier absorption is a disadvantage associated with this technique. Intel researchers used an MOS configuration embedded in silicon waveguides in a Mach–Zehnder geometry and were able to demonstrate high-frequency modulation with 3 dB bandwidth of 20 GHz and data transmission up to 30 Gb/s [14]. This performance is limited by the free-carrier's lifetime. The high speed is the result of a unique device design with a traveling-wave drive scheme allowing electrical and optical signal co-propagation along the waveguide. The traveling-wave electrode which is based on a coplanar waveguide was designed to match the velocity for both optical and electrical signals. As described in the paper, the speed was pushed even further up to 40 Gb/s by optimizing the device packaging [15].

Although a lot of optical devices have been developed with the silicon platform, a room-temperature, electrically pumped, silicon laser is still the missing piece for monolithic integration because silicon has a poor stimulated emission cross section due to its indirect band gap structure. There have been many efforts toward the goal of silicon lasers [16]. Silicon light-emitting diodes have also been demonstrated [17]. Another effort was carried out on the hybrid AlGaInAs-silicon evanescent laser [16]. The device is comprised of a multiple-quantum-well structure bonded to a silicon waveguide on the SOI wafer. The optical mode overlaps both the III-V material and the silicon waveg-

uide so that the mode can obtain electrically pumped gain from the III-V region while being guided by the silicon waveguide region. The device showed room temperature continuous-wave (CW) lasing with 65 mA threshold, 1.8 mW output power and overall differential efficiency of 12.7% [16]. Meanwhile, mode-locked silicon evanescent lasers have also been demonstrated [18, 19].

Besides silicon based light sources, an integrated germanium-on-silicon detector was also developed by Intel in 2007 that can operate at the speed of 40 Gb/s [20].

1.1.4 Nonlinear Applications

Silicon is also promising for making nonlinear optical devices, because of its high Kerr and Raman nonlinearities [9]. Nonlinear applications in SOI waveguides are based on self-phase modulation (SPM), cross-phase modulation (XPM), stimulated Raman scattering (SRS), and four wave mixing (FWM). In addition, two-photon absorption (TPA), free-carrier absorption (FCA) and free-carrier induced dispersion (FCD) should also be taken into consideration in silicon. These are the research areas this thesis is going to focus on.

Self-phase modulation is a very efficient process in SOI waveguides [21]. SPM-induced spectral broadening is found to be significant at coupled peak powers of even a few tens of milli-watts. In Refs. [22, 23], a twofold increase in the spectral width was observed.

XPM was used to demonstrate strong modulation instability in silicon waveguides in the pump-probe configuration [24]. The result showed modulation instability gain spectrum that is 2 to 3 orders of magnitude larger than that achieved in optical fibers [24]. XPM in a silicon Mach-Zehnder interferometer was shown to work as an optical modulator. The dependence of XPM on walk-off was also observed experimentally [25].

Raman amplification in an SOI waveguide is promising because the Raman gain

peak is about 3000 times stronger than in silica fibers. Using stimulated Raman scattering, many nonlinear optical functions have been demonstrated, including Raman amplification [26], optical modulation [32] and wavelength conversion [33]. Net Raman gain was observed by several groups [26, 27]. Silicon Raman lasers [28–30] and a cascaded silicon Raman laser [31] have also been demonstrated. They provide the ability to generate coherent light in wavelength regions that are not easily accessible with other conventional types of lasers.

Four wave mixing is promising for all-optical signal processing, and has been studied widely [34–39]. Applications of FWM include wavelength conversion [34, 35], parametric amplification [36, 37] and photon-pair generation [38, 39]. Kuo et al. demonstrated wavelength conversion at 40 Gb/s data rate in silicon waveguides [35]. Net gain from FWM is not promising when CW pumps are used to pump a signal in an SOI waveguide because of the effect of free-carrier absorption. However, net gain in the case of pulsed pumps is achievable [37]. Lin et al. even proposed to achieve highly tunable optical parametric oscillation using silicon micro-resonators [40]. The pump was chosen to be beyond $2.2 \mu\text{m}$ to get around the issues of two-photon absorption and the consequent free-carrier effects.

The carrier-induced plasma-dispersion effect makes use of an electric field applied across the waveguide [41]. An alternative way to generate free carriers is through photon-absorption process using optical pumps [42–44]. This is faster than using external electrical field because the free carriers are generated locally. Applications based on this effect include carrier-induced optical bistability in silicon ring resonators [42], all-optical switching [43], optical modulation [41, 44], wavelength conversion [45], and silicon photonic memory [46, 47].

1.2 Thesis Objective

This thesis is intended to provide a comprehensive study of the optical properties of SOI waveguides with an emphasis on nonlinear properties, including a theoretical model of nonlinear light-material interaction covering both electronic and Raman responses, coupling loss and propagation loss measurements, mode calculations, dispersion analysis and dispersion tailoring, self-phase modulation, two-photon absorption, free-carrier absorption, free-carrier induced index change, influence of pulse trains with high repetition rate, continuous spectral blue shift, supercontinuum generation, cross-phase modulation, birefringence and nonlinear polarization rotation.

1.3 Thesis Outline

This thesis is organized in the following manner. Chapter 1 gives a short introduction of the current state of research in silicon photonics. Chapter 2 discusses the SOI waveguides we used in our laboratory, and the measurements of propagation loss, total insertion loss, and coupling loss using Fabry-Perot resonances, cutback method, and scattered light method. Chapter 3 discusses three mathematical tools for calculating the modes and dispersion properties of SOI waveguides, and compares the three methods from the aspects of accuracy and efficiency. Chapter 4 discusses the importance of anomalous dispersion properties in SOI waveguides, dispersion tailoring of SOI waveguides in order to realize anomalous dispersion at a wavelength around $1.5 \mu\text{m}$, and the possibility of soliton propagation in such a tailored waveguide. Chapter 5 provides a theoretical model for light propagation inside an SOI waveguide. The general formalism includes both the electronic and Raman responses of nonlinear light-material interaction. Chapter 6 considers the self-phase modulation process in SOI waveguides, with the emphasis on the role of two-photon absorption and the consequent free-carrier effects. The maximum allowed repetition rate of pulse trains is presented to serve as

a general guideline for using the self-phase modulation effect in real situations. This chapter also presents our experimental work on self-phase modulation showing significant spectral broadening and continuous spectral blue shift of pulses propagating through an SOI waveguide. Chapter 7 describes supercontinuum generation in SOI waveguides. Chapter 8 considers cross-phase modulation and nonlinear polarization rotation for realizing an SOI waveguide based optical Kerr shutter. The theoretical work is given first. Our preliminary experiment results are given after the theory. They show that the experiment of all-optical switching based on nonlinear polarization rotation is successful. Sub-pico-second switching window is realizable using this technique. Modulation depth as high as 16% is achieved at an optimized pump peak power. The required peak power of the input pump pulses can be as low as a couple of watts. However walk-off effect broadens the switching window when the pump power is high. Finally Chapter 9 deals with the laser sources we used in our experiments on SOI waveguides. It first discusses a home-made mode-locked fiber laser and a commercial high-power mode-locked fiber laser, and then presents the measurements of the pulse widths. Both interferometric and intensity autocorrelation are used for the pulse width measurements.

2 Waveguide Structure and Linear Loss Measurements

2.1 Waveguides Used in the Laboratory

Four waveguide structures are commonly used for experiments as discussed in Chapter 1. Among them, rib waveguide is the one used most often. However the birefringence of quasi-TE mode and quasi-TM mode is large for this structure. Quasi-TE mode is defined as the mode for which the dominant electrical field component is parallel to the plane of the substrate, while quasi-TM mode is defined as the mode for which the dominant component is perpendicular to the plane of the substrate. ‘Quasi-’ is used because the other components of the electrical field are usually non-zero. In our laboratory, we use both channel waveguides and ridge waveguides (A ridge waveguide is a rib waveguide that is etched all the way down to the silica layer.). An advantage of using a channel waveguide is its lower scattering loss because of smoother sidewalls. Figure 2.1 shows the pictures of two SOI waveguides fabricated by Jidong Zhang and Jonathan Y. Lee in Professor Philippe Fauchet’s group. Both waveguides show normal tapering at the facet. Our experiments are done with the channel waveguides. These waveguides are typically 400 nm in height, and 600 or 800 nm in width. They are not single mode waveguides at 1550 nm. But the phase velocities and mode profiles differ substantially for the fundamental mode and the high-order modes. As a result,

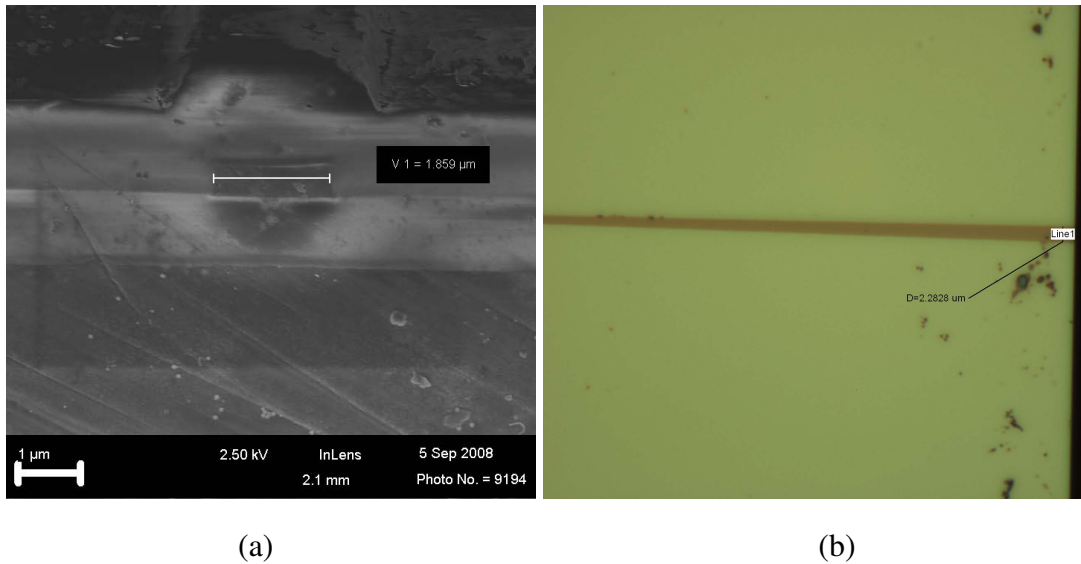


Figure 2.1: (a) SEM (scanning electron microscope) picture of one of the channel waveguides used in the laboratory. (b) Microscope image of a ridge waveguide used in the laboratory, the normal tapering feature is visible.

intermodal coupling is not likely to participate in the nonlinear processes that we are interested in.

We integrate both normal tapering and inverse tapering into the waveguides fabricated. The normal tapering is obviously seen in the microscope image in Fig. 2.1(b) which shows that the width of the waveguide becomes bigger toward the facet of the waveguide (right side of the picture). The slope is so small that we assume our taper to be adiabatic. The difference between these two waveguides is that the ridge waveguide (Fig. 2.1(a)) has no SiO_2 passivation on top while the channel waveguide (Fig. 2.1(b)) has the SiO_2 passivation on top. Most of our work is done on channel waveguides that has the SiO_2 passivation on top. In the case of waveguides with built-in mode-field converters, they take the structure of ridge waveguides.

We used two single-mode tapered fiber lenses (Nanonics Imaging Ltd.) to couple light into and out of the waveguides. Fig. 2.2 shows the structure of the fiber lens.

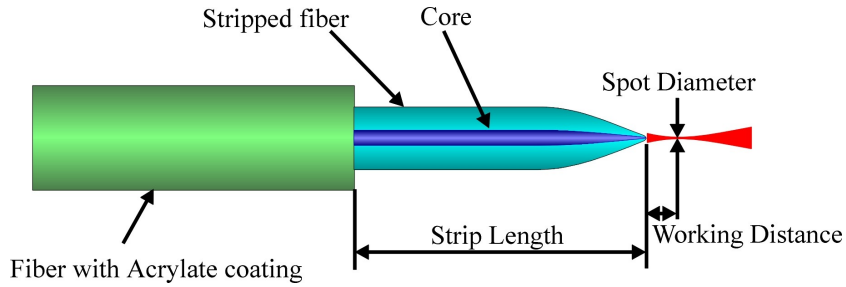


Figure 2.2: Diagram of a single-mode tapered fiber lens. (From Ref. [48].)

2.2 Loss Measurements

Linear losses need to be measured after the waveguides have been fabricated. Although the SOI waveguides are fabricated using undoped SOI wafer, there still may be some background doping that leads to free-carrier absorption that contributes to linear loss. The value of the doping concentration of the wafer we use is not directly specified. Normally the wafer is marked by resistivity ($\Omega\text{-cm}$). The bulk resistivity of silicon is related to the concentration of n-dopants, the electron mobility, or the concentration of p-dopants, and the hole mobility. And the resistivity is inversely proportional to the carrier concentration N , carrier mobility μ , and the electron/hole charge q by: $\rho = 1/(q\mu N)$ with $q = 1.6 \times 10^{-19}$ C. For intrinsic silicon, the electron mobility $\mu_e = 1500$ $\text{cm}^2/\text{V-s}$, the hole mobility $\mu_h = 450$ $\text{cm}^2/\text{V-s}$, and the carrier concentration is 1.5×10^{10} cm^{-3} [49]. The wafer we have been using are all with the very low resistivity of 20 $\Omega\text{-cm}$. In this case, the carrier concentration is $\sim 10^{14}$ cm^{-3} . And hence the linear absorption induced by background free carriers is $\alpha_f = \sigma N \sim 0.15$ $\text{m}^{-1} = 6 \times 10^{-3}$ dB/cm , where $\sigma = 1.45 \times 10^{-21}$ m^2 is the free carrier absorption coefficient for silicon. Another source of linear loss is the scattering loss due to the roughness of the side walls, which is on the order of $1 - 10$ dB/cm . So comparing with the scattering loss, the background free carriers induced linear loss is negligible. The third source of propagation loss is due to substrate leakage. However since the SiO_2 layer in our waveguide is typically greater than 1 μm , the leakage into

the substrate Si layer is also negligible.

There are three basic methods that can be used: the Fabry-Perot resonance method; the cut-back method; and the scattered light measurement method [2]. We use all three of them to measure the linear losses. For the first two methods, we use a tunable semiconductor laser (HP 8168F) as the light source, together with an InGaAs detector and a multi-meter (Keithley 2000) to read the output. For the third method, we use an infrared camera (SU320, Sensors Unlimited, Inc.) to capture the scattering pattern of the waveguides through a $20\times$ long-working-distance objective lens (Mitutoyo).

2.2.1 Fabry-Perot Resonances

A waveguide can be seen as a Fabry-Perot cavity with the two polished facets acting as two mirrors. So it is possible to measure the propagation loss using these Fabry-Perot resonances [2]. If we denote R as the facet reflectivity, the ratio of the output and the input powers is given by:

$$\frac{P_{\text{out}}}{P_{\text{in}}} = \frac{(1 - R)^2 e^{-\alpha L}}{(1 - R e^{-\alpha L})^2 + 4 R e^{-\alpha L} \sin^2(\phi/2)}, \quad (2.1)$$

where R for TM and TE modes is given by Fresnel's equations. For simplicity, we assume that light is coupled into the waveguide at normal incidence, then $R = (n - 1)^2 / (n + 1)^2$. A typical number of R is 0.31 since n is 3.5 for silicon at $\lambda = 1.55 \mu\text{m}$ at room temperatures [2]. $\phi = 2nkL \cos \theta + \phi_r$ is the phase difference associated with optical path difference of the resonator, and $\theta \approx 0$ is the incident angle. Writing $\zeta = I_{\text{max}} / I_{\text{min}} = [1 + R \exp(-\alpha L)]^2 / [1 - R \exp(-\alpha L)]^2$ as the ratio of the maximum intensity to the minimum intensity, the propagation loss α can be evaluated from Eq.(2.1). Since α decreases monotonically with increasing ζ , we obtain

$$\alpha = -\frac{1}{L} \ln \left(\frac{1}{R} \frac{\sqrt{\zeta} - 1}{\sqrt{\zeta} + 1} \right). \quad (2.2)$$

For all of our waveguides, a waveguide is composed of the waveguide region (2, 3, or 4 mm) and the two tapering regions ($150 \mu\text{m}$) with the dimension of $W \approx 2 \mu\text{m}$ at

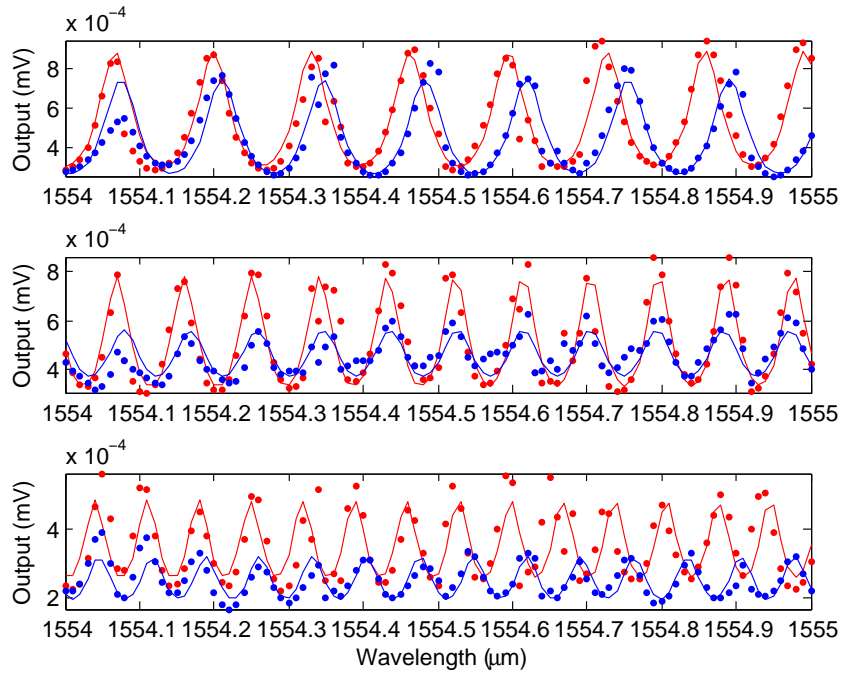


Figure 2.3: F-P resonance for three waveguides (2, 3, and 4 mm long) with normal tapering. Blue curves are for TE modes and red curves are for TM modes; dotted curves are measurements and solid curves are numerical fits to the transmission equation Eq. (2.1).

two ends. So the total lengths of the waveguides are 2.3, 3.3 and 4.3 mm respectively. The measurement and fitted curves for waveguides with normal tapering are shown in Fig. 2.3. The dotted curves represent experimental data, the solid curves represent numerical fitting using Eq. (2.1); the red curves represent TM mode, the blue curves represent TE mode. The refractive index used follows Eq. (3.5) which will be discussed in Chapter 3. Another thing to mention is that the successful fitting of the transmission curves requires that R is dispersive although the details are not shown here. The calculated α is shown in Table 2.1. The results show that the TM mode sees less propagation loss than the TE mode. As we will see later, the measurement using Fabry-Perot resonance is more stable than using the cutback method. We believe Fabry-Perot resonance is much more accurate. The results are shown in Table 2.1.

Length	Propagation loss (α)	
	TE (dB/cm)	TM (dB/cm)
2 mm	3.07 ± 1.10	3.05 ± 0.85
3 mm	13.75 ± 3.46	4.62 ± 1.78
4 mm	9.66 ± 2.39	5.56 ± 2.24

Table 2.1: Measurements of propagation losses for three normally tapered waveguides using the method of Fabry-Perot resonances.

2.2.2 Cutback Method

The cutback method is a simple way to estimate the propagation loss of a waveguide [2]. Literally it requires that we measure the output power P_1 of a waveguide with length L_1 , then cut the waveguide to length L_2 , and measure the output power P_2 . By assuming the same coupling and propagation losses, the propagation loss can be decided by the equation $\alpha = \ln(P_2/P_1)/(L_1 - L_2)$ [2]. A nondestructive alternative way is to measure the output from a set of waveguides with the same fabrication procedure but with different lengths. We assume that the coupling and propagation losses keep the same for different waveguides. If all the losses are expressed in the log scale, then we can use the linear fit of $\alpha_{\text{insertion}} = \alpha_{\text{coupling}} + \alpha_{\text{propagation}} \times L$ to find out the coupling loss α_{coupling} and propagation loss $\alpha_{\text{propagation}}$. Since the output power fluctuates at different input wavelength due to the Fabry-Perot resonances, we measured the power at the wavelengths that correspond to local maximum output. One set of the data points and fitted curves are shown in Fig. 2.4. The waveguides have the dimension of $600 \text{ nm} \times 400 \text{ nm}$. The lengths are $2 + 0.3 \text{ mm}$, $3 + 0.3 \text{ mm}$, and $4 + 0.3 \text{ mm}$ respectively. The coupling efficiencies will vary for different trials of measurement. However we have no better choice but to assume the same coupling efficiencies if we use the cutback method to estimate the linear losses. From Fig. 2.4, we see that the data points fluctuate around the fitted curves because of the uncertainties associated with this method. This method

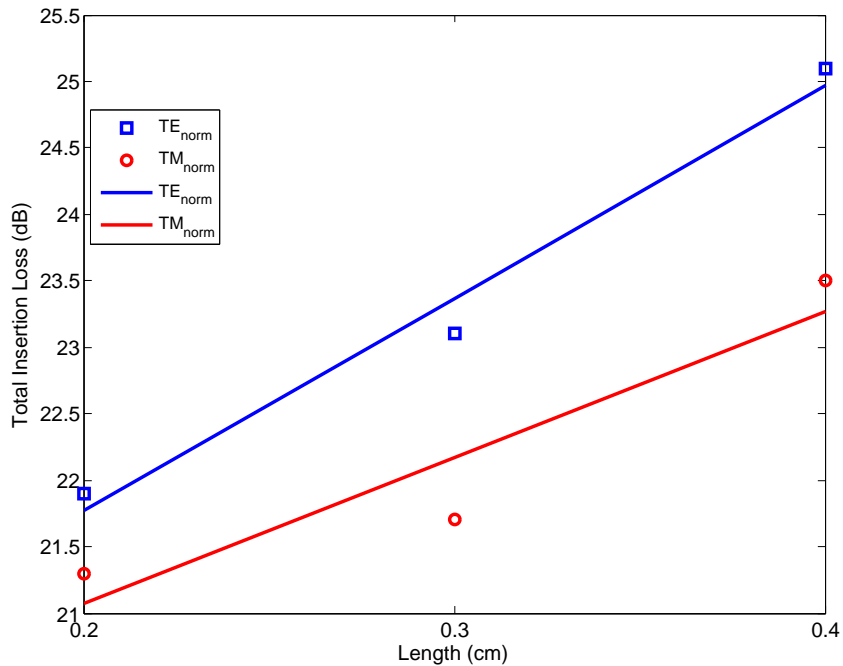


Figure 2.4: Measurements of total insertion loss using cutback method. Discrete points are measured data, curves are fitting for the corresponding data points using the relationship of total insertion loss (dB) is equal to coupling loss (dB) plus propagation loss (dB/cm) times waveguide length (cm).

is not accurate because the coupling losses and propagation losses fluctuate with different trials of coupling light into different waveguides. We can not really use the cutback method to deduce the linear losses. However, it gives the information of total insertion loss. If we use the measurement of propagation loss from the Fabry-Perot resonances, then we can estimate the coupling loss from the measurement of total insertion loss for the waveguides with normal tapering. The results are given in Table 2.2.

2.2.3 Scattered Light Measurement

The propagation loss of a waveguide can also be known by measuring the scattered light from the surface of the waveguide [2]. The assumption of this method is that the amount of light scattered from the surface is proportional to the light propagating

Length	Total Insertion Loss (dB)		Coupling Loss (dB)		Propagation Loss (dB/cm)	
	TE	TM	TE	TM	TE	TM
2 mm	21.9	21.3	21.2	20.6	3.07	3.05
3 mm	23.1	23.7	18.6	22.2	13.75	4.62
4 mm	25.1	23.5	20.9	21.1	9.66	5.56

Table 2.2: Measurements of coupling losses and propagation losses for waveguides with normal tapering using the combination of cutback method and Fabry-Perot resonances.

inside the waveguide. Then the rate that the scattered light decays should mimic the decaying rate of the propagated light inside the waveguide. Optical fibers can be used to collect the scattered light and can be scanned along the surface of the waveguide. In a previous paper, periodic gratings were used to couple light out of the waveguide and then the light was collected using a lens and detected using a silicon avalanche photodiode (APD) [50]. In our experiment, we take images of the surface of a 5 mm long waveguide using an infrared camera, and the entire surfaces of waveguides are scanned by taking a series of gray images along the waveguides. The log-scale gray-level averaged over the cross-section of a waveguide along the distance of the waveguide is plotted and then fitted using a linear equation to estimate the propagation loss of the waveguide [51]. The results are shown in Fig. 2.5. The propagation loss of the waveguide is about 8.33 dB/cm for the TE mode and 1.84 dB/cm for the TM mode. Another thing need to mention is that the 5 mm long waveguide has the width of 600 nm and height of 400 nm. It has two integrated polymer mode-field converters at each end of the waveguide as shown in Fig. 1.3(d) in Chapter 1. The polymer mode-field converters have the dimension of $2 \times 2 \mu\text{m}^2$ which significantly improve the coupling of light into the waveguide.

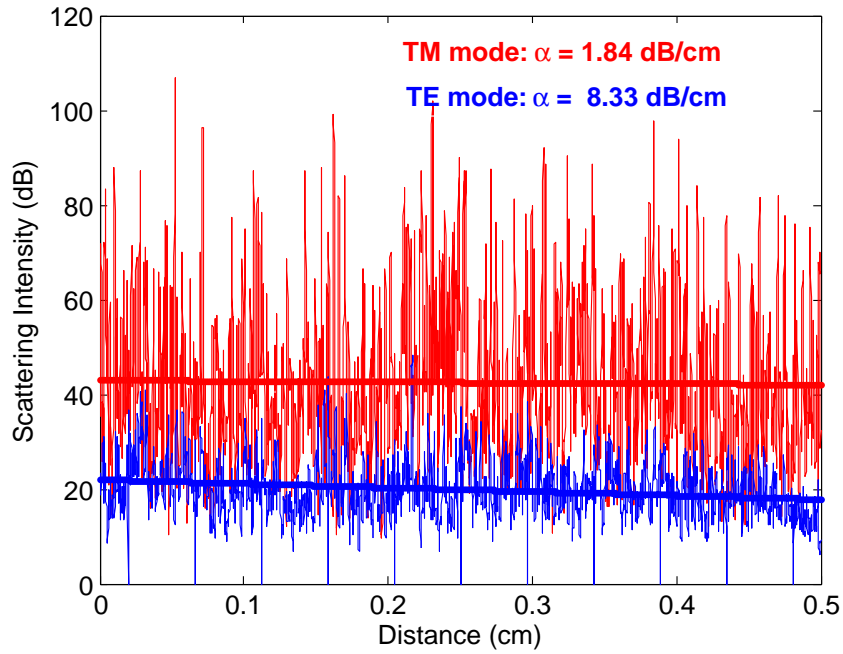


Figure 2.5: Log-scale intensity of light scattered vertically from the SOI waveguide for TM (red curves) and TE (blue curves) polarized light. Propagation losses are estimated by linear curve fitting technique.

2.3 Specialty of Inverse Tapering for SOI Waveguides

In the case of normal tapering, the facets have the dimension of $W \approx 2\mu\text{m}$, while in the case of inverse tapering, the situation is more complicated. The facet is $W \approx 100\text{ nm}$ for $L = 2\text{ mm}$, $W \approx 200\text{ nm}$ for $L = 3\text{ mm}$, and $W \approx 300\text{ nm}$ for $L = 4\text{ mm}$.

From the measurements we see that the TM mode sees less propagation loss than the TE mode. This originates from the fact that TE mode is more affected by the sidewalls. We can not really get any meaningful information from the measurements for the situation of inverse tapering since the facet widths of the three waveguides are different.

It is difficult to estimate the linear losses using the Fabry-Perot method for the cases of inverse tapering. The experimental data are shown in Fig. 2.6. We see that the resonance pattern is less obvious than that in the case of normal tapering. However, the

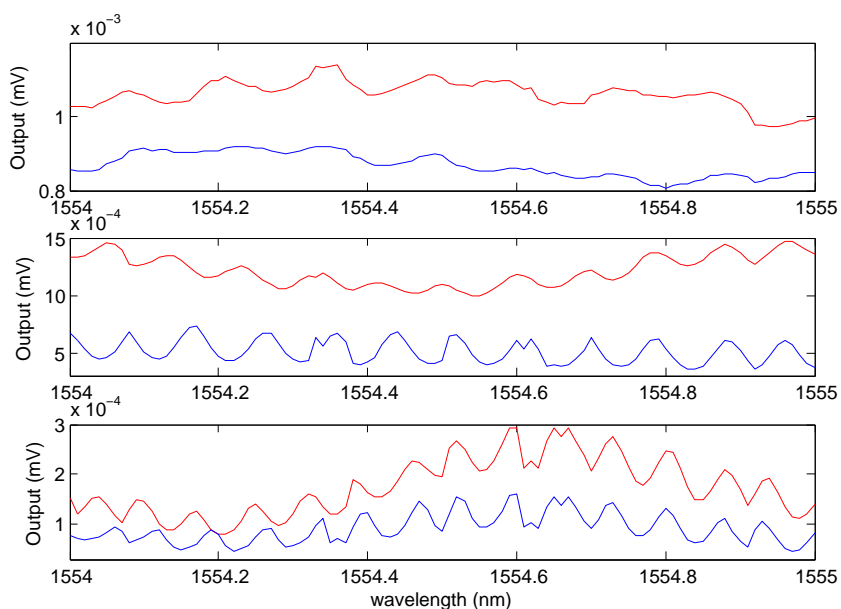


Figure 2.6: Fabry-Perot resonances for three waveguides with inverse tapering. The first waveguide is 2 mm long with a facet width of 100 nm; the second waveguide is 3 mm long with a facet width of 200 nm; the third waveguide is 4 mm long with a facet width of 300 nm.

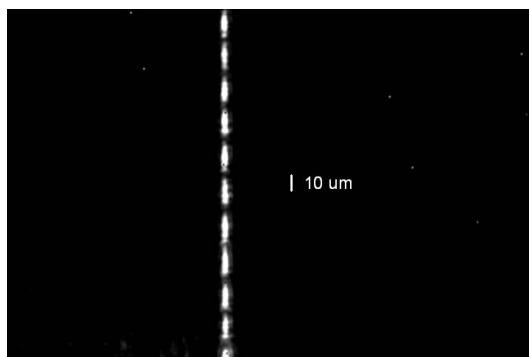


Figure 2.7: An interference pattern seen from the scattering of TE mode propagation inside an inversely tapered waveguide.

curves do show that there are more than one set of modulations. This is very obvious for the case of 4 mm long inversely tapered waveguide with the facet size of 300 nm \times 400 nm shown at the bottom of Fig. 2.6. Fig. 2.6 shows that there are two sets

of modulations, one is fast and the other is slow. We think this is because there are two resonators in the cavity. The slow modulation comes from the resonator which is actually the tapering section of the waveguide which is short, the fast modulation comes from the long resonator which is the nearly uniform central part of the waveguide. The effect of the main resonator is more and more obvious from 2 mm waveguide to 3 mm waveguide and to 4 mm waveguide because the main resonator accounts for a bigger ratio of the total length for longer waveguides. Another interesting phenomenon we see is the interference pattern of the scattered light as shown in Fig. 2.7. We see the strange periodic pattern with both the TM and TE modes inside an inversely tapered waveguide using single wavelength coupling. It may be due to the interference between different modes which implies that it is easier to excite higher-order modes in waveguides with inverse tapering.

2.4 Summary

In this chapter, we have discussed the waveguides used in our laboratory with different tapering schemes, and the measurements of coupling losses and propagation losses using the Fabry-Perot resonances, the cutback method and the scattered light measurement method. In the last section we have discussed the special behavior of SOI waveguides with inverse tapering. Since the Fabry-Perot resonance method is not suitable for measuring the propagation loss of a waveguide with inverse taperings, the scattered light measurement method is used in our experiments for those waveguides.

3 Mode and Dispersion Calculations

In this chapter I discuss the material dispersion of silicon, different methods of calculating waveguide modes and their dispersion characteristics, and then compare the accuracy and efficiency of different methods.

3.1 Material Dispersion of Silicon

Before calculating the dispersion of waveguide modes, we need to know the material dispersion first. The material dispersion relations we need in this thesis include those of silica and silicon.

The material dispersion of silica is well approximated by the Sellmeier equation [53]:

$$n^2(\lambda) = 1 + \sum_{j=1}^3 \frac{B_j \lambda^2}{\lambda^2 - \lambda_j^2}, \quad (3.1)$$

where λ_j is the j^{th} resonance wavelength and B_j is the strength of the resonance. For fused silica these parameters are $B_1 = 0.6961663$, $B_2 = 0.4079426$, $B_3 = 0.8974794$, $\lambda_1 = 0.0684043 \mu\text{m}$, $\lambda_2 = 0.1162414 \mu\text{m}$, and $\lambda_3 = 9.896161 \mu\text{m}$. It is nice that the spectrum region that we are interested in (around $1.5 \mu\text{m}$) is far from any of the resonances. So we can use this equation without much concern.

The situation for silicon is a little bit complicated. There is a modified Sellmeier expression that is widely used [54–56]:

$$n_{\text{Si}}^2(\lambda) = \varepsilon + \frac{A}{\lambda^2} + \frac{B\lambda_1^2}{\lambda^2 - \lambda_1^2}, \quad (3.2)$$

where $\lambda_1 = 1.1071 \mu\text{m}$, $\varepsilon = 11.6858$, $A = 0.939816$ and $B = 8.10461 \times 10^{-3}$. This dispersion equation produces very good fit to the experimental data taken at room temperature (299K). However, since the equation has a singularity at $\lambda_1 = 1.1071 \mu\text{m}$, it gives us trouble if we want to calculate the second and higher-order dispersion curves below $1.3 \mu\text{m}$. The exponential growth seen in the group velocity dispersion curves in some published papers [40, 57] shows this trouble. However, dispersion properties in this wavelength region are needed if we want to study the effects of ultralarge spectral broadening, such as supercontinuum generation in a silicon waveguide. In order to solve this difficulty, we use the data from Reference [55] with curve fitting and model n_{Si} accurately with the following Sellmeier-type relation:

$$n_{\text{Si}}^2(\nu) = 1 + \frac{c_1}{1 - (h\nu/E_1)^2} + \frac{c_2}{1 - (h\nu/E_2)^2}, \quad (3.3)$$

where $h\nu$ is the photon energy, $E_1 = 4.27 \text{ eV}$, $E_2 = 3.38 \text{ eV}$, $c_1 = 9.733$, and $c_2 = 0.936$ [52]. We can rewrite the equation in terms of wavelength as:

$$n_{\text{Si}}^2(\lambda) = 1 + \frac{c_1\lambda^2}{\lambda^2 - \lambda_1^2} + \frac{c_2\lambda^2}{\lambda^2 - \lambda_2^2}, \quad (3.4)$$

where $\lambda_1 = 0.2904 \mu\text{m}$, and $\lambda_2 = 0.3669 \mu\text{m}$. This equation takes into account the two direct bandgap absorptions [58] instead of the indirect bandgap absorption used in Eq. (3.2).

Other than the Sellmeier-type equation, the refractive index of silicon at room-temperature is also fitted with a Herzberger-type dispersion formula [59]:

$$n_{\text{Si}}(\lambda) = A + BL_\lambda + CL_\lambda^2 + D\lambda^2 + E\lambda^4, \quad (3.5)$$

where $L_\lambda = 1/(\lambda^2 - 0.028)$ with the wavelength λ in microns and 0.028 is the square of the mean asymptote for the short-wavelength abrupt rise in the refractive index for

14 materials (silicon included). For the silicon refractive index from $1.12 \mu\text{m}$ to $588 \mu\text{m}$ at room temperature (26°C), the coefficients are $A = 3.41906$, $B = 1.23172 \times 10^{-1}$, $C = 2.65456 \times 10^{-2}$, $D = -2.66511 \times 10^{-8}$, and $E = 5.45852 \times 10^{-14}$. As stated in Ref. [59], the quality of the fit of the reported experimental indices to the dispersion formula is good with differences in the third and fourth decimal places. Since we need smooth higher-order dispersion curves around $1.2 \mu\text{m}$, we will use Eq. (3.5) for future calculation of the refractive index of silicon material.

3.2 Methods for Calculating Waveguide Modes

It is important to know the modes and dispersion of an SOI waveguide in order to carry out the research on its optical nonlinear properties. The calculation of dispersion reduces to the calculation of mode index since n^{th} order dispersion is related to the n^{th} order derivative of the mode index. And the mode profile can also be calculated if the mode index is known [53]. There are many ways to calculate the mode index. One way is to solve the two Maxwell curl equations in the frequency domain using the method called Finite Difference in Frequency Domain (FDFD) [60]. There are free software packages available online. For example Optical Modesolver is a free FDFD simulation software package developed at the University of Maryland [61] that solves the mode indices and mode profiles directly. A second method is to solve the Maxwell equations in the frequency domain using the method called Finite Element in Frequency Domain (FEFD) [62]. The third method is the finite-difference Beam Propagation Method (BPM) that solves the scalar Helmholtz equations [62], which is also readily extendable to the vector form to include both of the TE and TM modes. Rsoft's BeamProp package [63] is such an example. The fourth one is the effective index method (EIM) [53]. The EIM treats a rectangular waveguide as two one-dimensional waveguides that are placed vertically to each other, where the index of the core region of the second waveguide takes the value of the calculated effective mode index of the first waveguide. This

method is applicable for waveguides whose one dimension is larger than the other dimension. In the case of the rib waveguides that we are interested in, it is still acceptable to use the EIM. In the case of waveguides whose two dimensions are comparable to each other, an option is to treat the waveguide as a two-dimensional rectangular waveguide [64]. These will be discussed in more detail later in this chapter.

Although many methods can be used to calculate the modes and dispersion of an SOI waveguide, in this chapter we only discuss three of them in detail: FDFD, BPM, and EIM. We treat FDFD method as the most accurate one, and compare the results using the other two methods with those obtained using FDFD to discuss their accuracy. The issue of time consumption is another factor we will discuss later in this chapter.

3.2.1 FDFD Mode Solver

The FDFD method provides a numerical solution to Maxwell's two curl equations in the frequency domain. In a finite-difference method, the domain of analysis is discretized with a rectangular grid of points. The numerical algorithm converts the derivatives of a function into differences of the function values at neighboring grid points. The finite-difference method essentially translates a second order partial differential equation into a conventional matrix eigenvalue equation. The partial differential operators have been replaced by large sparse matrices, and the eigenfunctions have been replaced by long vectors representing a sampling of the eigenfunctions at discrete grid points [62]. As described in a recent paper [60], the finite-difference method was used to solve the Maxwell's equations for H_x and H_y components of the electromagnetic field since they are continuous both tangentially and normally across the boundaries in a non-magnetic media with no current sources or free charge. The other field components H_z , E_x , E_y , and E_z can be derived from H_x and H_y according to the Maxwell's equations. The detailed theory will not be discussed here. We are interested in using this method to get the mode information and dispersion properties of our waveguides.

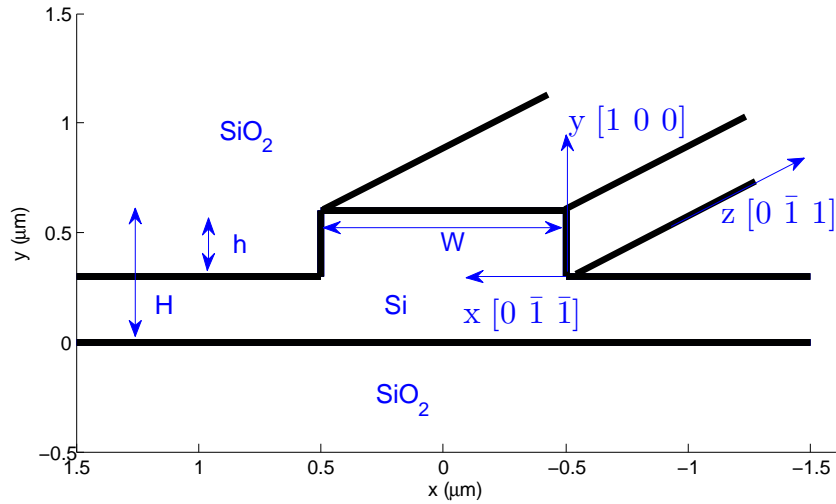


Figure 3.1: Sketch of an SOI rib waveguide fabricated on the (1 0 0) surface of the silicon crystal.

Here I give an example of a rib waveguide with dimension of width $W = 1 \mu\text{m}$, height $H = 0.6 \mu\text{m}$, and etch thickness $h = 0.3 \mu\text{m}$. The core is silicon, and the cladding is silica as shown in the Figure 3.1. We use Eq. (3.1) for the material refractive index of silica, and Eq. (3.5) for the material refractive index of silicon. The Matlab software for the FDFD method was downloaded from Professor Murphy's website [61]. The field profiles of the fundamental quasi-TE mode and quasi-TM mode at the wavelength of $1.55 \mu\text{m}$ are shown in Figure 3.2. Half of the waveguide is used for calculation because the waveguide is symmetric along the $x = 0$ axis. Although the magnetic field components H_x and H_y are used to setup the eigenvalue equations, we are only interested in the electric field components. The fundamental quasi-TE mode, shown on the left half of the plot, clearly shows a very strong E_x component together with weak but non-zero E_y and E_z components. Also the E_x component is discontinuous on the right boundary. The fundamental quasi-TM mode, shown on the right half of the plot, shows a very strong E_y component with weak but non-zero E_x and E_z components. Also the E_y component is discontinuous on the upper and lower boundaries.

The FDFD modesolver calculates the mode index n_{eff} at a specified wavelength. We

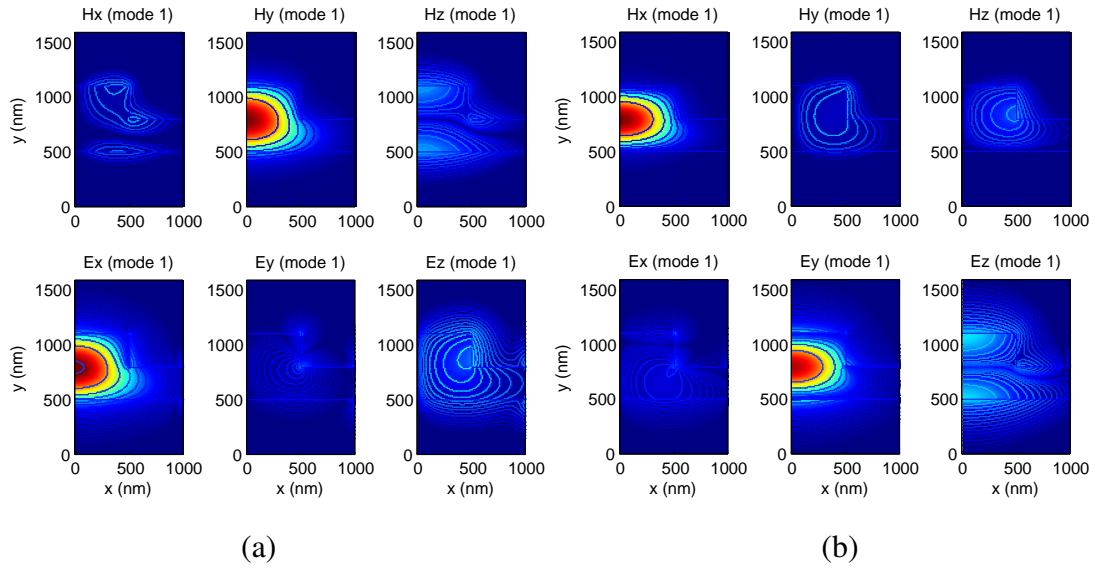


Figure 3.2: Field profiles for the fundamental (a) quasi-TE and (b) quasi-TM modes. All of the six field components of the electromagnetic field are shown.

can do the same calculation for the fundamental TE and TM modes while scanning the wavelength to study the dispersion properties of the waveguide through $\beta = n_{\text{eff}}2\pi/\lambda$. Then the n^{th} order dispersion is $\beta_n = d^n\beta/d\omega^n$, where ω is the angular frequency of the light. I used the functions `spline.m` and `fntlr.m` to calculate the Taylor polynomials in order to calculate the derivatives of β at different orders. However, the accuracy of calculation depends on the computational window and the resolution of the points in the grid. The details for this calculation are as follows: The size of the computation window is 1700 nm in the x direction and 1800 nm in the y direction, grid size is $dx = dy = 4$ nm. The results are shown in Figure 3.3. The zero dispersion wavelengths (ZDWL) are found to be $\lambda_0 = 2002.5$ nm for the TE mode and $\lambda_0 = 1482.3$ nm for the TM mode.

3.2.2 Finite-Difference Beam Propagation Method

The technique of Finite-Difference Beam Propagation Method uses finite-difference methods to solve the paraxial approximation of the Helmholtz equation [62]. By fac-

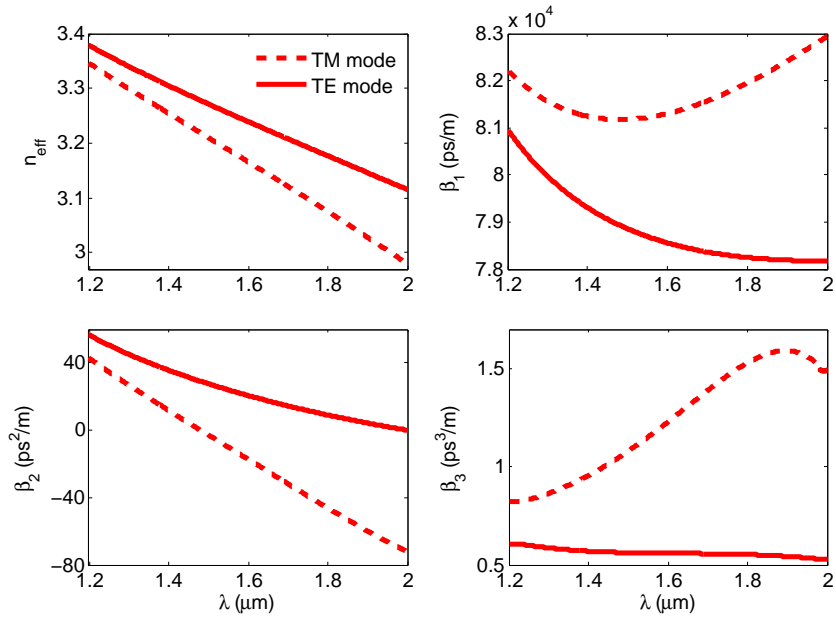


Figure 3.3: Calculation of dispersion for a waveguide with width $W = 1 \mu\text{m}$, height $H = 0.6 \mu\text{m}$, and etch thickness $h = 0.3 \mu\text{m}$.

toring rapid phase variations along the z direction, together with the paraxial approximation, which says that the second-order derivative of the field with respect to z is negligible, the second-order boundary value problem is reduced to a first-order initial value problem that can be solved by a simple integration along the propagation direction z . The fundamental limitation of this approach results from the paraxial approximation to the Helmholtz equation. It limits the study to fields that propagate primarily along the z axis (i.e. small angle propagation) and places restrictions on the index contrast [62]. However, this limit can be significantly relaxed through the use of so-called wide-angle BPM. In the case of silicon waveguides, we use vector BPM and perform parameter scans of wavelength to calculate the dispersion of the SOI multilayer waveguide. However, wide-angle BPM is not available for mode calculation. The typical calculated electrical fields at $\lambda = 1.55 \mu\text{m}$ are shown in Figure 3.4. TE mode is on the left side and TM mode is on the right side.

For a good comparison, the computational grid sizes (4nm) are chosen to be the

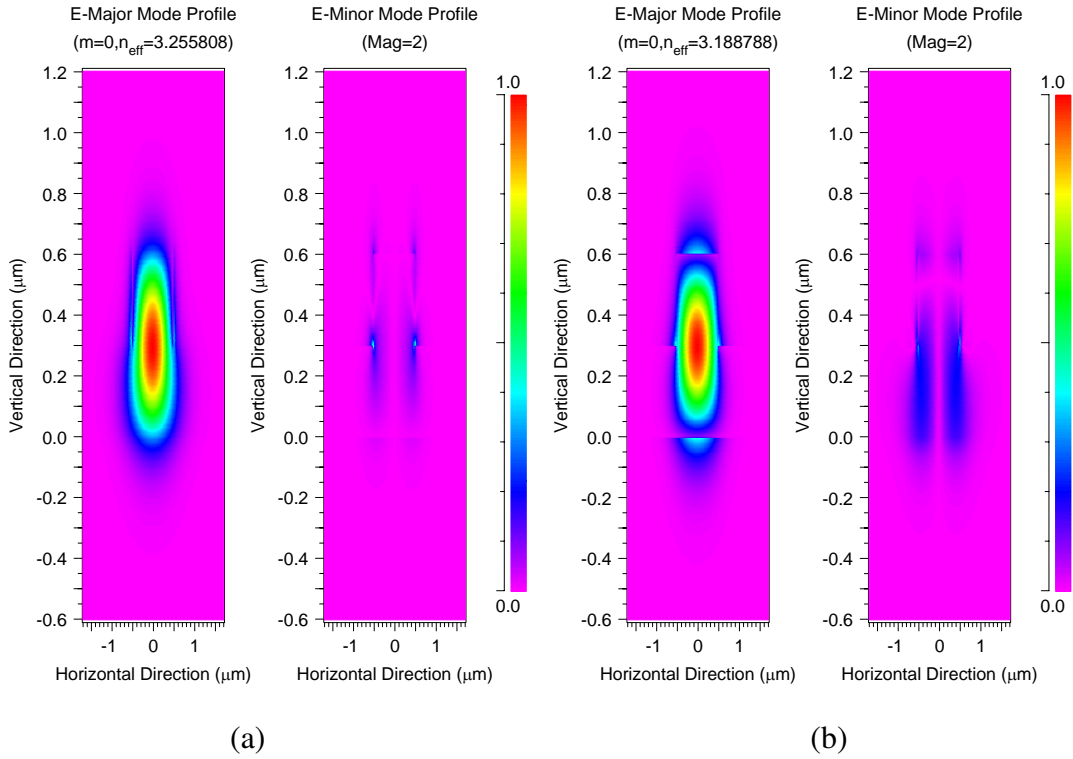


Figure 3.4: Field profiles for the fundamental (a) quasi-TE and (b) quasi-TM modes.

same as those for the FDFD calculation while the computing window on the x axis covers the whole waveguide instead of half as needed in FDFD method. The computing step size of dz is also chosen to be 4 nm. The simulation results are post-processed in Matlab to get the dispersion curves as shown in Figure 3.5. The results from the FDFD method are also shown for comparison. The accuracy of the BPM method is decent as long as $\lambda/n < H$, and it can be improved by optimizing the grid sizes. The BPM calculation takes up much less computer memory compared with the Matlab-based FDFD calculation. However, it's more time consuming at the same spatial resolution of 4 nm. Another difficulty is that this method will not give a smooth curve for high-order dispersion if the computing grid size is not small enough. Several peer researchers have noticed this issue. I had the same difficulty several years ago when I tried to use the BPM method to calculate the dispersion of SOI waveguides. I gave up on this method because of the difficulties. However, my intensive calculations show that this

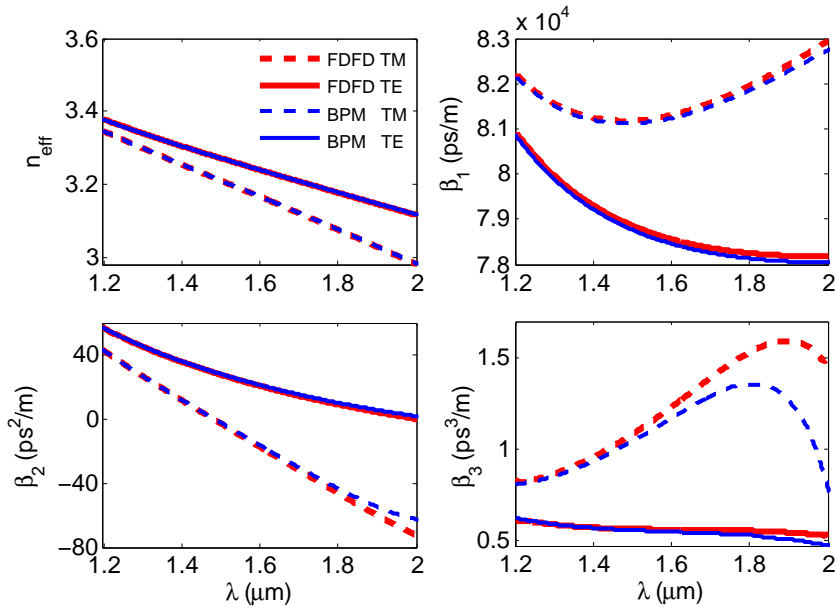


Figure 3.5: Calculation of dispersion for a waveguide with width $W = 1 \mu\text{m}$, height $H = 0.6 \mu\text{m}$, and etch thickness $h = 0.3 \mu\text{m}$.

is related to the resolution of the computing grid sizes. The solution is to reduce the grid sizes. However, it will be extremely time-consuming if the grid size is reduced to below 10 nm. An easier way is to calculate less points using BPM, and then use Matlab's spline function to interpolate the data to smooth the curves. Another point worthy of mentioning is that it is not always better to use smaller grid sizes because we may get some very strange results in some conditions. We need to take several trials with different computing grid sizes in order to get an optimized calculation. For example, calculation of the TM mode gives a sudden decrease of mode index beyond $1.7 \mu\text{m}$ when I use 4 nm as the computing steps. The final calculation for TM mode uses 8 nm as the computing steps instead, and the step size for wavelength scanning is 40 nm. The ZDWLs are found to be $\lambda_0 = 2056.4 \text{ nm}$ for the TE mode and $\lambda_0 = 1485.2 \text{ nm}$ for the TM mode. These results are quite close to those obtained with FDFD method. However, simulations with the BPM method take much longer time to provide the results.

3.2.3 Effective Index Method

In the simplified version of the EIM method, we treat the rib waveguide as an imaginary one-dimensional (1D) waveguide whose refractive index of the cladding is the calculated effective index of the etched region while the refractive index of the core is the calculated effective index of the center region. In order to calculate the effective index of the cladding, n_{clad} , we treat the etched region as an infinite 1D SOI waveguide along the y axis whose height is $H - h$ and $d_y = (H - h)/2$. And the same procedure is carried out to calculate the effective index of the core (the center region) n_{core} while the height is H and $d_y = H/2$. Finally the effective index of the whole rib waveguide is calculated assuming an infinite 1D waveguide along the x axis whose width is W and $d_x = W/2$. The refractive index of the core is n_{core} and the refractive index of the cladding is n_{clad} .

The eigenvalue equations for the 1D y-axis waveguide are [53]:

$$2p_y d_y = m\pi + 2 \tan^{-1} \left(\frac{n_1^2 q}{n_2^2 p_y} \right) \quad (\text{TM mode}), \quad (3.6)$$

$$2p_y d_y = n\pi + 2 \tan^{-1} \left(\frac{q}{p_y} \right) \quad (\text{TE mode}), \quad (3.7)$$

where m and n are the orders of mode, n_1 is the refractive index of Si, n_2 is the refractive index of SiO₂, $p_y^2 = n_1^2 k_0^2 - \beta^2$, and $q^2 = \beta^2 - n_2^2 k_0^2$. n_{eff} is then calculated from β . While the eigenvalue equations for the 1D x-axis waveguide are:

$$2p_x d_x = m\pi + 2 \tan^{-1} \left(\frac{q}{p_x} \right) \quad (\text{TM mode}), \quad (3.8)$$

$$2p_x d_x = n\pi + 2 \tan^{-1} \left(\frac{n_{\text{core}}^2 q}{n_{\text{clad}}^2 p_x} \right) \quad (\text{TE mode}), \quad (3.9)$$

where n_{core} and n_{clad} are calculated through the procedures discussed above, $p_x^2 = n_{\text{core}}^2 k_0^2 - \beta^2$, and $q^2 = \beta^2 - n_{\text{clad}}^2 k_0^2$. One thing to notice is that the TM and TE mode equations for the 1D x-axis waveguide are different from that for the 1D y-axis waveguide.

Following the method described above, the ZDWLs are found to be $\lambda_0 = 2006.1$ nm for the TE mode and $\lambda_0 = 1459.6$ nm for the TM mode. The results are shown in Figure

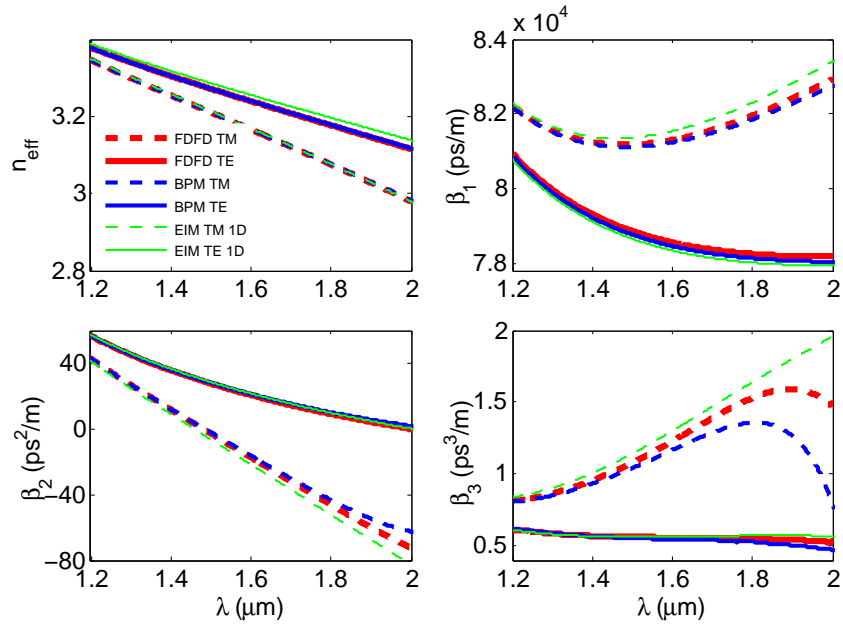


Figure 3.6: Calculation of dispersions for a waveguide with width $W = 1 \mu\text{m}$, height $H = 0.6 \mu\text{m}$, and etch thickness $h = 0.3 \mu\text{m}$ using 1D effective index method.

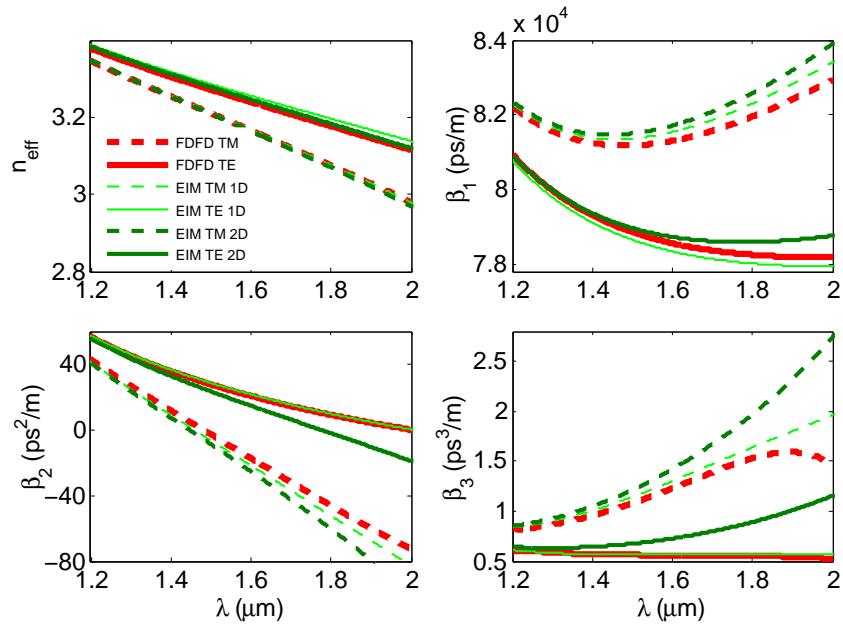


Figure 3.7: Calculation of dispersions for a waveguide with width $W = 1 \mu\text{m}$, height $H = 0.6 \mu\text{m}$, and etch thickness $h = 0.3 \mu\text{m}$ using 2D effective index method.

3.6. The calculation is not as accurate as either the FDFD or BPM method. However, it still gives decent demonstration of the dispersion properties, and it takes only a couple of seconds to do the calculation while FDFD and BPM methods take tens of minutes, or even a few hours to do the calculation of the same number of wavelengths.

Another way is to solve the eigenvalue problem as a two-dimensional rectangular waveguide [53]. The refractive index of the etched region is still calculated using a 1D approximation whose height is $H - h$. However, the center region is calculated using the eigenvalue equations for a rectangular waveguide whose cross section is $W \times H$. The index of the core is still n_{Si} ; the indices of the substrate and cover are n_{SiO_2} ; the indices on the left and right side of the rectangle are the calculated n_{clad} . Using this method, the ZDWL are found to be $\lambda_0 = 1775.7$ nm for the TE mode and $\lambda_0 = 1446.4$ nm for the TM mode. The results are shown in Figure 3.7. Surprisingly the calculation of the 2D EIM is not as accurate as the 1D EIM. This is true only for a rib waveguide because of the two etched regions. In the case of rectangular waveguides, 2D EIM gives better accuracy.

3.3 Summary

In this chapter, we have described the FDFD, BPM and EIM methods of calculating the mode index of an SOI waveguide. The FDFD method is the most accurate among the three methods, however, the requirement on a computer's memory is high. It takes 42 minutes to calculate both the TE and TM mode indices at 50 different wavelengths using my personal computer (Intel Core 2 CPU at 2 GHz with 2GB memory). The computing window and grid sizes are described earlier. The BPM method can be accurate enough as long as the wavelength is not too long ($\lambda/n < H$) and the grid sizes are chosen correctly. BPM is less tight on the memory requirement, but it takes 500 minutes to calculate 50 data points for both the TE and TM modes with the same grid sizes. Another issue is that the computational window of the BPM method is twice the

size of that used in FDFD method. The EIM method is the fastest among all three. It only takes 1.3 seconds to calculate 50 data points while the accuracy is still acceptably good as long as the wavelength is not too long ($\lambda/n < H$).

4 Dispersion Tailoring and Soliton Propagation

In this chapter, we consider dispersion in SOI waveguides and show that the ZDWL λ_0 of the waveguides used in some of the published journal papers typically exceeds $2 \mu\text{m}$. We also show that λ_0 can be shifted to below $1.5 \mu\text{m}$ with reasonable device parameters. Under such conditions, an ultrashort pulse at $1.55 \mu\text{m}$ should form a soliton as it propagates in the waveguide. This possibility may lead to new applications of SOI waveguides related to optical interconnects and high-speed optical switching. We use a modified nonlinear Schrödinger equation to study soliton evolution inside SOI waveguides in the presence of linear loss and two-photon absorption (TPA) [57].

4.1 Dispersion Tailoring

In the study of nonlinear optics, we know that anomalous dispersion is very important for efficient nonlinear interactions because the peak power of the pulse can be maintained at a relatively high level throughout the propagation, and high peak power is crucial for strong nonlinear interactions. This is because self-phase modulation always puts a positive chirp onto the pulse while anomalous dispersion puts a negative chirp onto the pulse, and these chirps can cancel each other to some degree to stop the pulse width from fast broadening and hence the peak power can be kept high. However, in

the case of normal dispersion, the dispersion also puts a positive chirp onto the pulse. The enhanced chirp makes the pulse width broadens out quickly which leads to a lower level of the peak power.

Quite a few four-wave mixing (FWM) based wavelength-conversion experiments have been carried out in SOI waveguides recently [35, 65]. The common difficulty in most cases is a very low conversion efficiency (less than -8 dB) even when a reverse-biased electric field was applied to sweep out the free carriers generated through two-photon absorption. We propose that this is related to dispersion properties of the waveguides in use. We know that it's very important to have anomalous dispersion for efficient four-wave mixing phenomena [66]. The efficiency of FWM will be low if the pump propagates in the normal dispersion region of the waveguide.

In order to test the validity of our proposal, we need to calculate the dispersion properties of the waveguides used in a FWM experiment. There are several methods available for the calculation of modes and dispersions as discussed in Chapter 3. Considering both the calculation speed and accuracy, I adopt the effective index method to obtain the dispersion relation $\beta(\omega)$ numerically for the TM_0 and TE_0 waveguide modes, where β is the modal propagation constant at the frequency ω . For our study, the three important parameters are the width W , the height H , and the etch thickness h for the waveguide geometry shown in Figure 3.1; the dispersive properties should vary considerably with these parameters. We first set $W = 1.5 \mu\text{m}$, $H = 1.55 \mu\text{m}$, and $h = 0.7 \mu\text{m}$, the values used in a recent experiment [65]. The material dispersion of Si is included using the Herzberger-type dispersion formula in Eq. (3.5). The modal refractive indices are determined from $\bar{n}(\omega) = \beta(\omega) c/\omega$ and are plotted in Figure 4.1 as a function of wavelength. The difference between the two modal indices is related to the waveguide-induced birefringence.

Dispersion to the n^{th} order can be calculated from $\beta(\omega)$ using the relation $\beta_n(\omega) = d^n \beta/d\omega^n$. The wavelength dependence of the second- and third-order dispersion parameters is shown in Figure 4.1. The ZDWL of the TM_0 mode occurs near $2.1 \mu\text{m}$,

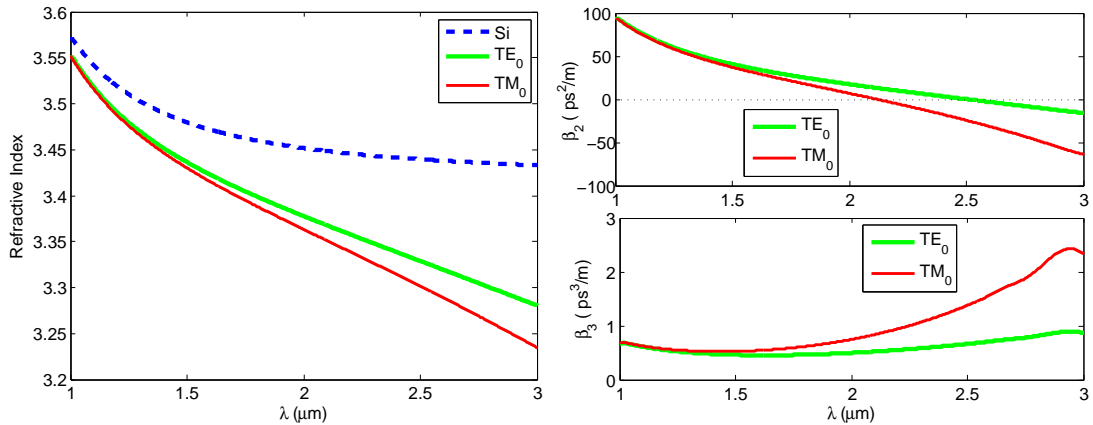


Figure 4.1: Modal refractive indices of the TE_0 (dashed line) and TM_0 (solid line) modes for $W = 1.5 \mu\text{m}$, $H = 1.55 \mu\text{m}$, and $h = 0.7 \mu\text{m}$. The material dispersion of silicon is shown by a dashed line.

and that of the TE_0 mode near $2.5 \mu\text{m}$. In the wavelength region near $1.55 \mu\text{m}$, $\beta_2 \approx 34 \text{ ps}^2/\text{m}$ is positive (normal dispersion) for both modes. The third-order dispersion is relatively small with a value $\beta_3 \approx 0.53 \text{ ps}^3/\text{m}$. We stress that our results are approximate because of the use of the effective-index approximation. However this method is good enough for the current purpose.

The important question from a practical standpoint is whether SOI waveguides can be designed to exhibit anomalous dispersion ($\beta_2 < 0$) near $1.55 \mu\text{m}$. This is possible if λ_0 is reduced to below $1.55 \mu\text{m}$ by choosing the device parameters appropriately. We have performed extensive numerical calculations to study how the ZDWL depends on W , H , and h and how it can be controlled by designing the SOI waveguide suitably. The results are shown in Figure 4.2. Figure 4.2 (a) and (b) indicate that λ_0 decreases as W and H are reduced. Figure 4.2 (c) shows that there is an optimum value of h for the TM_0 mode for minimizing λ_0 . The contours of this optimum value of h are shown in Figure 4.2 (d) in the W - H plane. Note that λ_0 is almost always lower for the TM_0 mode compared with the TE_0 mode. In fact, λ_0 cannot be reduced to below $1.5 \mu\text{m}$ for the TE_0 mode because the required width of $W < 0.3 \mu\text{m}$ becomes impractical. In the

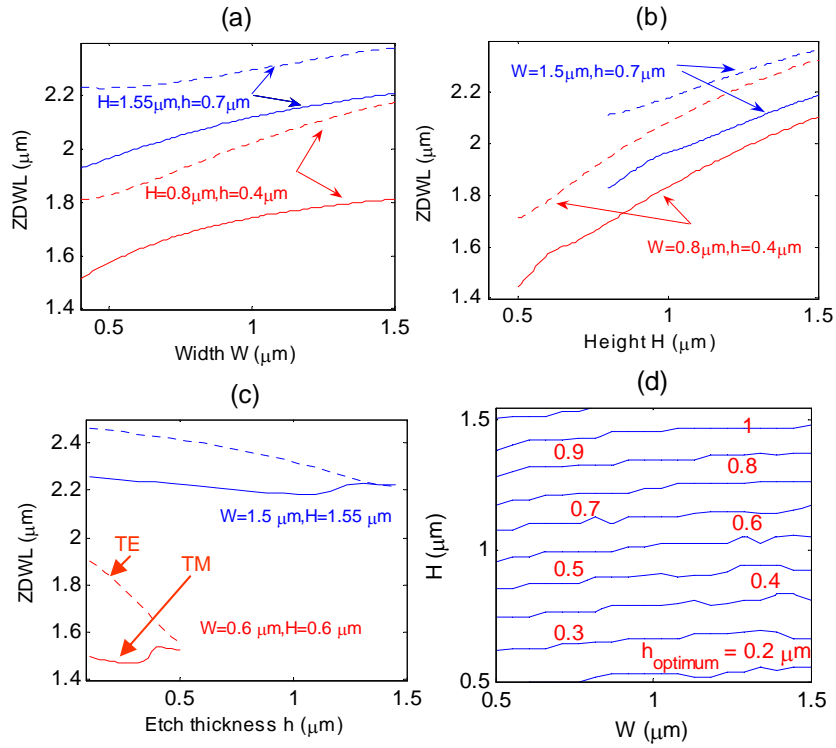


Figure 4.2: Dependence of ZDWL on (a) W , (b) H , and (c) h for the TE₀ (dotted lines) and TM₀ (solid lines) modes; (d) Contours of optimum h in the range of 0.3 to 1.1 μm in W - H plane for the TM₀ mode.

case of TM₀ mode, λ_0 can be reduced to below 1.55 μm for W in the range of 0.5 to 1.5 μm provided H and h are chosen properly.

To find the range of W and H for realizing a specific value of λ_0 , we depict in Figure 4.3 the contours of constant λ_0 in the W - H plane with h optimized in each case. It follows that the dispersion can be made anomalous at 1.55 μm for a wide range of device parameters. As an example, $\beta_2 < 0$ at 1.55 μm when $W = 1\mu\text{m}$, $H = 0.6\mu\text{m}$, and $h \approx 0.3\mu\text{m}$. These device parameters are realistic for SOI waveguides.

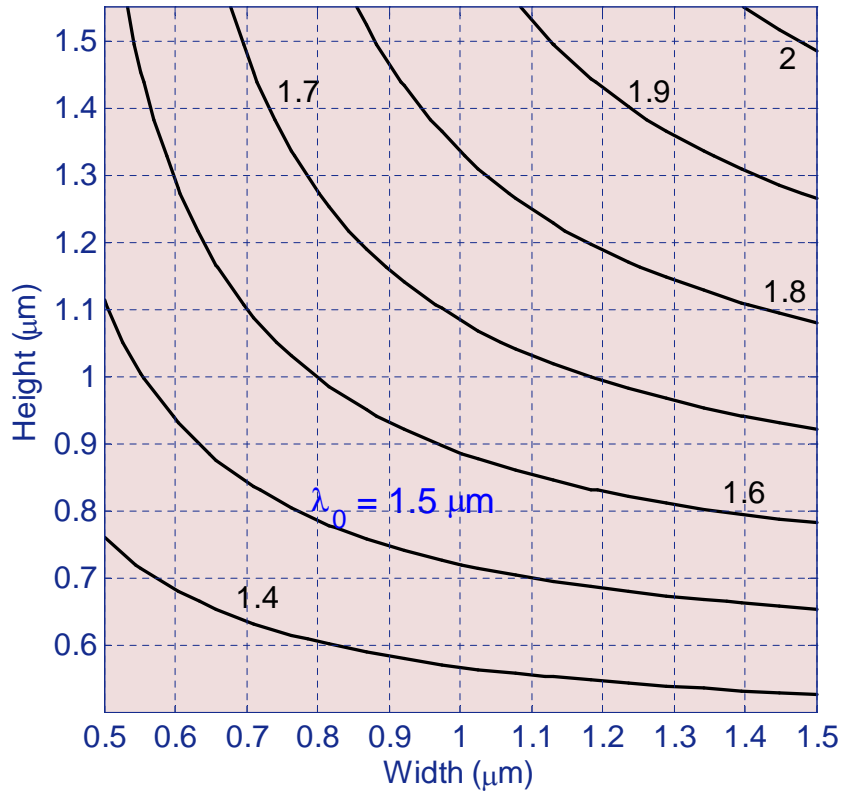


Figure 4.3: Contours of constant ZDWL as a function of W and H in the range of $\lambda_0 = 1.4$ to $2 \mu\text{m}$; etch thickness h is optimized for each set of W and H and is in the range of $h/H = 0.4$ to 0.8 .

4.2 Soliton Propagation

One should expect an optical soliton to form inside an SOI waveguide if $\beta_2 < 0$. A rough estimate of the pulse parameters can be obtained using the standard soliton theory [66]. According to this theory, a fundamental soliton can be excited if $\gamma P_0 L_D = 1$, where $\gamma = 2\pi n_2 / (\lambda A_{\text{eff}})$ is the nonlinear parameter, P_0 is the peak power, and $L_D = T_0^2 / |\beta_2|$ is the dispersion length for a pulse of width T_0 . The nonlinear refractive index of silicon is $n_2 \approx 2.5 \times 10^{-18} \text{ m}^2/\text{W}$ [67]. Using $W = 1 \mu\text{m}$, $H = 0.6 \mu\text{m}$, and $h = 0.3 \mu\text{m}$, the parameters of the TM_0 mode at $1.55 \mu\text{m}$ are found to be: $\beta_2 = -13.7 \text{ ps}^2/\text{m}$, $\beta_3 = 1.2 \text{ ps}^3/\text{m}$, $\lambda_0 = 1.46 \mu\text{m}$, $a_{\text{eff}} = 0.15 \mu\text{m}^2$, and $\gamma = 67.6 \text{ W}^{-1}/\text{m}$. If we assume $L_D = 1 \text{ cm}$,

then $T_0 = 370$ fs, corresponding to a full width at half maximum of 652 fs for the pulse shape governed by $P(t) = P_0 \text{sech}^2(t/T_0)$. The required peak power for $\gamma P_0 L_D = 1$ is about 1.5 W, a relatively low value for 650-fs pulses.

Before concluding that a soliton would form when such pulses are launched into the waveguide, we should consider the impact of linear loss, TPA, and free-carrier absorption (FCA). SRS can be ignored for 650-fs pulses because their bandwidth (≈ 0.5 THz) is much less than the Raman shift of 15.6 THz for Si. We modify the standard nonlinear Schrödinger equation to include TPA and FCA, and obtain (see Chapter 5)

$$\frac{\partial A}{\partial z} + \frac{\alpha_l}{2} A + \frac{i\beta_2}{2} \frac{\partial^2 A}{\partial t^2} - \frac{\beta_3}{6} \frac{\partial^3 A}{\partial t^3} = i\kappa |A|^2 A - \frac{\alpha_f}{2} A, \quad (4.1)$$

where $\alpha_l = 0.22$ dB/cm is the linear loss and $\kappa = \gamma + i\Gamma/2$. The imaginary part of κ is related to the TPA coefficient, $\beta_{\text{TPA}} = 5 \times 10^{-12}$ m/W [67], as $\Gamma = \beta_{\text{TPA}}/a_{\text{eff}} = 12.5$ W⁻¹/m. FCA is included by $\alpha_f = \sigma N$, where $\sigma = 1.45 \times 10^{-21}$ m² for silicon [27] and N is the density of carriers produced by TPA. It is obtained by solving [27]

$$\frac{\partial N}{\partial t} = \frac{\beta_{\text{TPA}}}{2h\nu_0} \frac{P^2(z)}{a_{\text{eff}}^2} - \frac{N}{\tau_c}, \quad (4.2)$$

where $\tau_c \approx 25$ ns is the effective carrier lifetime. For $T_0 \ll \tau_c$, and at relatively low repetition rates, the peak value of N can be approximated as $N \approx 2\beta_{\text{TPA}} P_0^2 T_0 / (3h\nu_0 a_{\text{eff}}^2)$. For the device parameters used, $N \approx 9.6 \times 10^{20}$ m⁻³. Since $\alpha_f \approx 1.4 \times 10^{-2}$ cm⁻¹ $\ll \alpha_l$ for this value of N , we can neglect FCA in Eq. (4.1).

We solve Eq. (4.1) with the split-step Fourier method [66] and study soliton propagation inside a 5-cm long SOI waveguide. The input and output pulse shapes and the corresponding spectra are plotted in Fig. 4.4 under several different conditions. The pulse does not maintain its width because of β_3 , α_l , and β_{TPA} . The green curves show the output supposing there is no linear loss or TPA. The pulse shape is distorted slightly because of third-order dispersion and shows that the impact of β_3 is relatively minor. Even without TPA, linear loss leads to pulse broadening, and TPA enhances this broadening further. However, we should stress that the pulse would broaden by a factor of

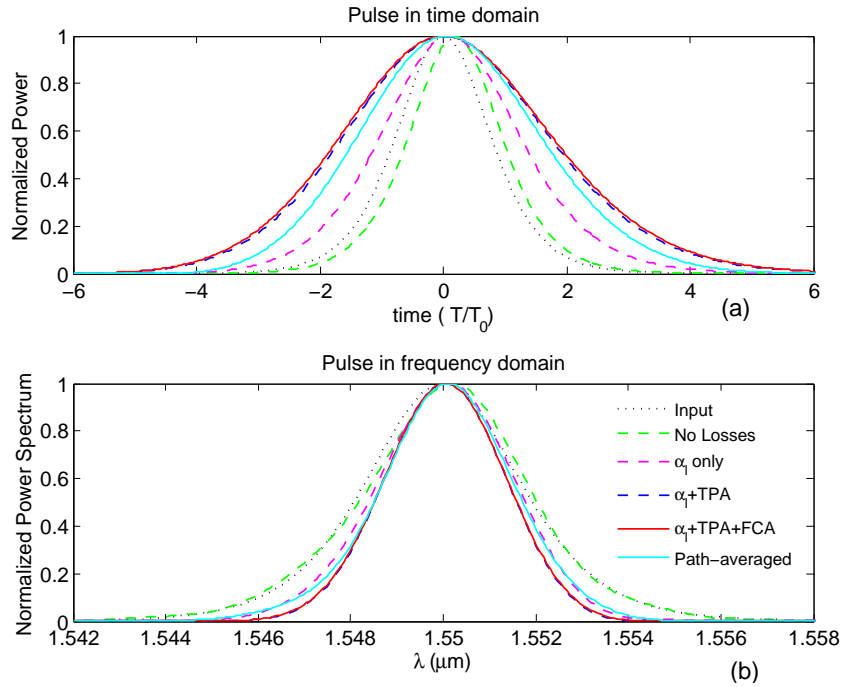


Figure 4.4: Output (a) pulse shape and (b) spectrum with different loss mechanisms included, third order dispersion is included in all cases; dotted curves show input profiles. The curve marked path-averaged shows that the loss-induced pulse broadening can be compensated to some degree by increasing the input peak power suitably.

4 in the absence of nonlinear effects. Clearly, soliton effects help because the pulse broadens by a factor of less than 2. The output pulse and spectrum with FCA are also plotted for comparison. And we see that it is justified to neglect free-carrier effects in the case of soliton propagation since the peak power is still on the low end.

We can reduce the pulse broadening even further by using the concept of a path-averaged soliton [66]. In this approach, the input peak power is increased by averaging pulse peak power over the waveguide length, $\bar{P}_0 = \frac{1}{L} \int_0^L P_0(z) dz$, and requiring $\gamma \bar{P}_0 L_D = 1$. This amounts to enhancing the input peak power by a factor of $F_e = \alpha_l L / [1 - \exp(-\alpha_l L)]$, where $\alpha_l = \alpha_l + \Gamma \bar{P}_0$ is the total effective loss. For the parameters used, F_e equals 1.6. As shown in Fig. 4.4, the broadening induced by linear loss and TPA can be reduced considerably when the input power is increased by this factor.

Indeed, an experiment has demonstrated dispersion tailoring and soliton propagation inside an SOI waveguide [68].

4.3 Summary

In summary, we studied the dispersive properties of SOI waveguides and found that the ZDWL of the TM_0 mode is approximately $2.1 \mu\text{m}$ for the device used in Ref. [35]. We used numerical calculations to reveal the dependence of the ZDWL on the three design parameters of the device. The results show that λ_0 can be reduced to below $1.55 \mu\text{m}$ with reasonable waveguide dimensions. A guideline for choosing the device parameters in order to get the desired ZDWL is given in a contour plot. For a device with width $1 \mu\text{m}$, height 600 nm , and etch thickness 300 nm , the second-order dispersion at $1.55 \mu\text{m}$ is found to be negative. Propagation of a 650-fs pulse at $1.55 \mu\text{m}$ reveals that such a pulse can nearly maintain its shape and spectrum over a 5-cm -long waveguide because of the soliton-like effects in the anomalous-dispersion regime.

5 Theoretical Framework for Nonlinear Interactions in Silicon Waveguides

In this chapter, we discuss a theoretical framework for the nonlinear pulse propagation in silicon waveguides, which includes dispersion, linear loss, self-phase modulation, two-photon absorption, Raman scattering, free-carrier absorption, and free-carrier dispersion. In the complete model, the nonlinear wave interactions are expressed in the form of a convolution between material response function (including both electronic response and Raman response) and the electric field of light. The Raman response function is discussed in detail to reveal its polarization selection properties and its relative contribution to the total nonlinear response. Finally, we briefly discuss the variance of experimental measurements of the nonlinear refractive index, n_2 , and the TPA coefficient, β_{TPA} , over a large range.

5.1 General Formalism

The nonlinear interactions of optical waves inside silica fibers are well understood owing to extensive investigations over the past few decades [66]. The so-called generalized nonlinear Schrödinger equation (NLSE) provides a fairly accurate description,

even for ultrashort pulses creating an octave-spanning supercontinuum [69]. As the origin of third-order nonlinearity in silicon waveguides is quite similar to that of silica fibers, a similar theoretical formalism can be used for silicon waveguides, with suitable modifications to account for the features unique to silicon. Since silicon is a semiconductor crystal, the unique features include two-photon absorption (TPA), free-carrier absorption (FCA), free-carrier dispersion (FCD), and the anisotropic and dispersive third-order nonlinearity [9, 27, 67, 70, 71].

In my paper on supercontinuum generation [52], I have given a generalized nonlinear Schrödinger equation (NLSE) to describe the pulse evolution in an SOI waveguide. In a 2007 review paper [9], a more complete model was used, and the time-domain evolution of the amplitude $A_j(z, t)$ ($j = x, y, z$) of the pulse was given as:

$$\frac{\partial A_j}{\partial z} = \sum_{m=0}^{\infty} \frac{i^{m+1} \beta_{jm}}{m!} \frac{\partial^m A_j}{\partial t^m} + i \beta_j^f(\omega, N_e, N_h) A_j + i \left(1 + i \xi \frac{\partial}{\partial t} \right) P_j^{\text{NL}}, \quad (5.1)$$

where the first term on the right side of the equation represents the linear loss (imaginary part of β_{jm}) and linear dispersion of the waveguide mode (real part of β_{jm}), the second term represents the free-carrier induced loss and dispersion, and the third term represents the third-order nonlinear effects. β_{jm} is the m^{th} order dispersion parameter at ω_0 . These parameters also include the linear loss when $\beta(\omega)$ is a complex quantity.

If we assume that free carriers are generated only optically so that $N_e = N_h = N_c$ for the free carrier densities, then

$$\beta_i^f(\omega, N_e, N_h) = \beta_i^f(\omega, N_c) \approx \frac{n_0(\omega)}{n_i(\omega)} \left[\frac{\omega}{c} n_f(\omega, N_c) + \frac{i}{2} \alpha_f(\omega, N_c) \right], \quad (5.2)$$

where the real part represents free-carrier dispersion and the imaginary part represents free-carrier absorption. Here n_0 is the material refractive index of silicon, and $n_i = c\beta_i(\omega)/\omega$ is the modal refractive index. The free-carrier index $n_f = \sigma_n(\omega)N_c = \zeta(\omega_r/\omega)^2 N_c$, where $\zeta \approx -1.35 \times 10^{-27} \text{ m}^3$ when the reference frequency ω_r corresponds to the wavelength of 1550 nm [42]. The free-carrier absorption $\alpha_f = \sigma_a(\omega)N_c =$

$1.45 \times 10^{-21} (\omega_r/\omega)^2 N_c$ (in units of m^2). The dynamics of the averaged free-carrier density is governed by a simple equation of the form [9, 52]

$$\frac{\partial N_c(z, t)}{\partial t} = \frac{\beta_{\text{TPA}}}{2h\nu_0} \frac{|A(z, t)|^4}{a_{\text{eff}}^2} - \frac{N_c(z, t)}{\tau_c}, \quad (5.3)$$

where $\beta_{\text{TPA}} = 5 \times 10^{-12} \text{ m/W}$ is the two-photon absorption coefficient, a_{eff} is the averaged effective area, and τ_c is the effective carrier lifetime that includes all the effects of recombination, diffusion, and drift [72].

In Eq. (5.1), ξ is related to the frequency dependence of the nonlinear parameter, and is given by [9]

$$\xi \equiv \frac{1}{\omega_0} + \frac{1}{\chi_e(\omega_0)} \frac{d\chi_e}{d\omega} \Big|_{\omega_0} - \frac{1}{a_{\text{eff}}(\omega_0)} \frac{da_{\text{eff}}}{d\omega} \Big|_{\omega_0}, \quad (5.4)$$

where $\chi_e(\omega_0) \equiv \chi_{1111}^e(-\omega_0; \omega_0, -\omega_0, \omega_0)$. In practice, the ξ term becomes important only when the spectrum of input pulses broadens by a large factor during their propagation inside a silicon waveguide, for example, in the case of supercontinuum generation [52]. In many cases of practical interest, $\xi \ll 1$, and its contribution can be neglected. The nonlinear polarization $P_j^{\text{NL}}(z, t)$ has the following compact form in the time domain:

$$P_j^{\text{NL}}(z, t) = A_k(z, t) \int_{-\infty}^{\infty} R_{jklm}^{(3)}(t - \tau) A_l^*(z, \tau) A_m(z, \tau) d\tau, \quad (5.5)$$

where the third-order nonlinear response function is given by [9]

$$\begin{aligned} R_{jklm}^{(3)}(t) = & \gamma_e(\omega_0) \delta(\tau) \left[\frac{\rho}{3} (\delta_{jk} \delta_{lm} + \delta_{jl} \delta_{km} + \delta_{jm} \delta_{kl}) + (1 - \rho) \delta_{jklm} \right] \\ & + \gamma_R h_R(t) (\delta_{jl} \delta_{km} + \delta_{jm} \delta_{kl} - 2\delta_{jklm}), \end{aligned} \quad (5.6)$$

where the electronic nonlinear parameter $\gamma_e(\omega_0)$ is defined as

$$\gamma_e(\omega_0) \equiv \chi_{1111}^e(-\omega_0; \omega_0, -\omega_0, \omega_0) \equiv \gamma_0(\omega_0) + i\beta_{\text{TPA}}(\omega_0)/(2a_{\text{eff}}), \quad (5.7)$$

and $\gamma_0 = \omega_0 n_2 / (c a_{\text{eff}})$ is the nonlinear Kerr parameter. The nonlinear anisotropy of silicon is characterized by $\rho \approx 1.27$. The percentage contribution of Raman scattering

to the total third-order nonlinear responses is γ_R . $h_R(t)$ is the Raman response function. The Raman response is discussed in more detail in the next section. As we will see later, γ_R is only a few percent of γ_e and is negligible unless the pulse spectrum falls within the Raman gain bandwidth.

Equation (5.1) is written in a coordinate basis aligned along the crystallographic axes. For commonly used silicon wafers where the substrate is on the (1 0 0) surface, this amounts to assuming that the waveguide is fabricated along the [0 1 0] or [0 0 1] direction. If that is not the case, the nonlinear response in other Cartesian coordinate systems can be found by a suitable rotation of the basis. Usually, an SOI waveguide is fabricated along the [0 $\bar{1}$ 1] direction because of cleaving convenience. In this case, the new coordinate system is obtained by a 45 ° rotation along the [1 0 0] direction, and the components of the $_{ijklm}$ become

$$R'_{yyyy}(t) = \gamma_e \delta(t), \quad R'_{xxxx}(t) = \gamma_e \delta(t)(1 + \rho)/2 + \gamma_R h_R(t), \quad (5.8)$$

$$R'_{xyxy}(t) = R'_{yxyx}(t), \quad R'_{yxyx}(t) = \gamma_e \rho \delta(t)/3 + \gamma_R h_R(t). \quad (5.9)$$

Equations (5.8) and (5.9) above show that the electronic contribution is enhanced for the quasi-TE mode ($R'_{xxxx}(t)$) by a factor of $[(1 + \rho)/2 - 1]$ (about 14%) having its origin in the nonlinear anisotropy [9].

Equation (5.1) provides a general theoretical basis for studying the nonlinear effects in silicon waveguides in the time domain. We can use it to study a variety of nonlinear phenomena inside silicon waveguides. Following the simplification procedures described earlier in this section, in most applications if stimulated Raman scattering is negligible (which is true according to the next section), it can be simplified further as [73]

$$\frac{\partial A_x}{\partial z} = \sum_{m=0}^{\infty} \frac{i^{m+1} \beta_{xm}}{m!} \frac{\partial^m A_x}{\partial t^m} - \frac{\alpha_l}{2} A_x - \frac{\sigma}{2} (1 + i\mu) N_c A_x + \frac{ik_0 n_2}{a_{\text{eff}}} (1 + ir) \left(\frac{1 + \rho}{2} |A_x|^2 + \frac{\rho}{3} 2 |A_y|^2 \right) A_x, \quad (5.10)$$

$$\frac{\partial A_y}{\partial z} = \sum_{m=0}^{\infty} \frac{i^{m+1} \beta_{ym}}{m!} \frac{\partial^m A_y}{\partial t^m} - \frac{\alpha_l}{2} A_y - \frac{\sigma}{2} (1 + i\mu) N_c A_y + \frac{ik_0 n_2}{a_{\text{eff}}} (1 + ir) \frac{\rho}{3} (|A_y|^2 + 2 |A_x|^2) A_y, \quad (5.11)$$

where $j = x$ in Eq. (5.11) represents TE component, and $j = y$ represents TM component. For the term representing third-order nonlinear response, the first term in the parenthesis represents SPM, while the second term with a factor of two represents cross-phase modulation (XPM) and cross-two-photon absorption (XTPA), where XTPA means that two photons from different origins are absorbed simultaneously to generate an electron in the conduction band and a hole in the valence band of silicon. $\mu = 2k_0\zeta/\sigma$, and $r = \beta_{\text{TPA}}/(2k_0n_2)$.

5.2 Stimulated Raman Scattering

An important thing to notice about Raman scattering in SOI waveguides is its polarization dependence. From Eqs. (5.8) and (5.9) we see that $R_{yyyy}^{(3)}(t)$ is the only component that does not have any contribution from the Raman response term. Two important conclusions about Raman scattering can be drawn from Eqs. (5.8) and (5.9) for SOI waveguides fabricated along the $[0 \bar{1} 1]$ direction. First, the Raman contribution is absent for the quasi-TM modes polarized along the $[1 0 0]$ direction as shown in Fig. 3.1. Second, the Raman coupling between the pump and signal waves, polarized orthogonally and launch as the TE and TM modes, occurs with the same magnitude γ_R [9], but the Kerr nonlinearity is reduced roughly by one third in such a polarization configuration compared with the co-polarized TE – TE situation.

If we consider the scenario of a single pulse propagating in the TE mode, it is useful to write the third-order response function in Eq. (5.8) as $R_{xxxx}^{(3)}(t) = (\gamma_R/f_R)R(t)$, where $R(t) = (1 - f_R)\delta(t) + f_R h_R(t)$. Here the first term governs the nearly instantaneous electronic response and $h_R(t)$ is the Raman response function originating from optical phonons [52, 66]. The parameter f_R represents fractional contribution of the nuclei to the total nonlinear polarization. The functional form of the Raman response function $h_R(t)$ is deduced from the Raman gain spectrum, $g_R(\Omega)$, known to exhibit a narrow Lorentzian peak of $\Gamma_R/\pi = 105$ GHz bandwidth, located $\Omega_R/(2\pi) = 15.6$ THz away

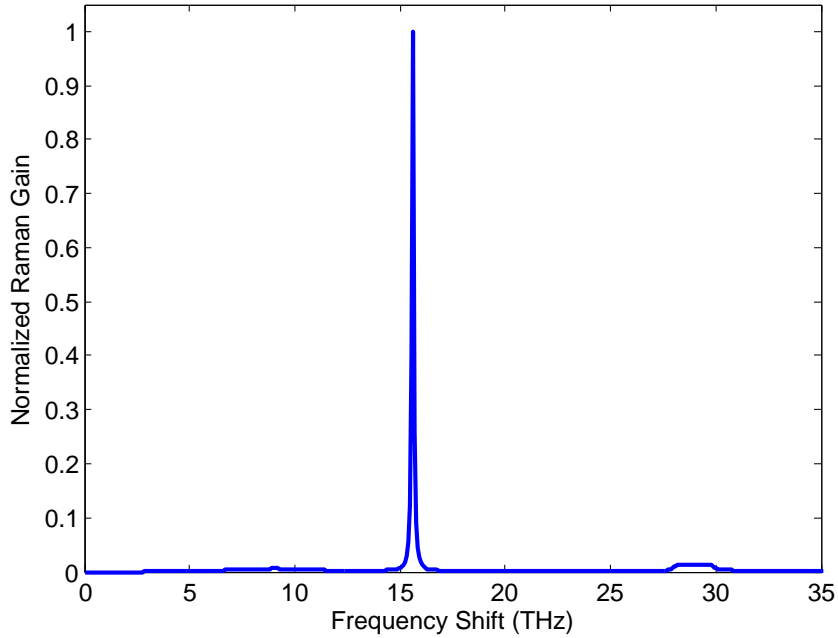


Figure 5.1: Raman spectrum of crystalline silicon. The experimental data also shows high-order Raman scattering. (From Ref. [74].)

from the pump frequency as shown in Fig. 5.1 [74]. The figure shows the normalized $g_R(\Omega)$ for crystalline silicon as a function of the frequency shift at a pump wavelength $\lambda_p = 488$ nm [74]. For other non-resonant pump wavelengths, $g_R(\Omega)$ keeps the same shape while the peak value depends inversely on λ_p . The imaginary part of the Fourier transform $H_R(\Omega)$ of $h_R(t)$ is related to $g_R(\Omega)$ as $\text{Im}[H_R(\Omega)] = g_R(\Omega)/(2n_2k_0f_R)$, where $k_0 = 2\pi/\lambda_0$. We use the value $g_R^{\text{max}} = 2 \times 10^{-10}$ m/W at the Raman gain peak [21] and $n_2 = 2.5 \times 10^{-18}$ m²/W [67]. The real part of $H_R(\Omega)$ is then found from the Kramers–Kronig relation. The real part and imaginary part of $H_R(\Omega)$ is shown in Fig. 5.2. Once $H_R(\Omega)$ is known, $h_R(t)$ is obtained by taking its inverse Fourier transform. The parameter f_R is found to be 0.1032 from the normalization condition of $\int_0^\infty h_R(t)dt = 1$; this value is relatively small compared with $f_R = 0.18$ for silica fibers [66]. Then we have $\gamma_e/\gamma_R = 2(1 - f_R)/[f_R(1 + \rho)]$ for the co-polarized TE – TE situation.

In the case of Raman scattering through TE-TM mode coupling, Eq. (5.9) indicates that $\gamma_e/\gamma_R = 3(1 - f'_R)/(f'_R\rho)$, hence $f'_R = 3f_R(1 + \rho)/(2\rho + 3f_R + \rho f_R) \approx 2.28f_R$.

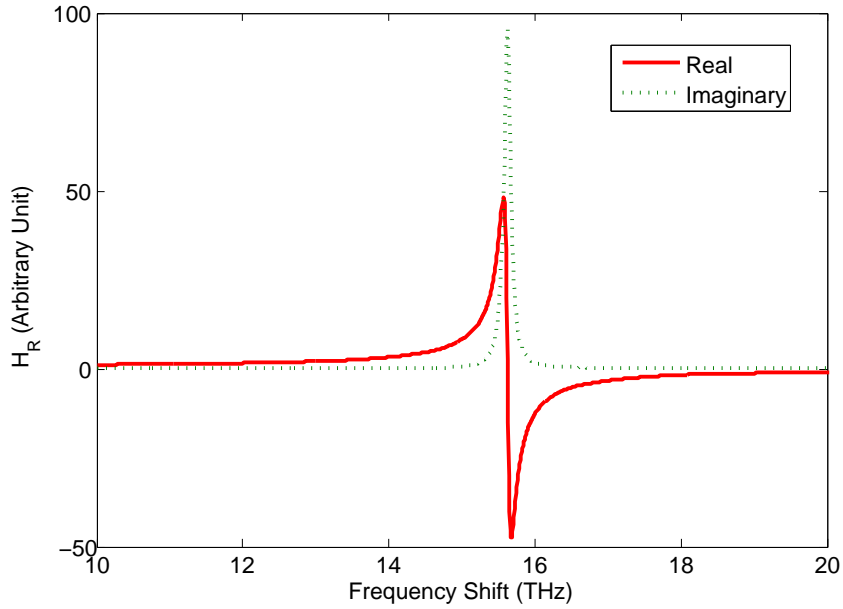


Figure 5.2: Real part and Imaginary part of $H_R(\frac{\Omega}{2\pi})$

This means that Raman response contributes more to the total nonlinear response in this scenario.

The above analysis is based on the experimental data of the Raman spectrum which shows other multi-phonon Raman processes as well. Another way to describe the Raman response is to use the equation for a damped oscillator [66]

$$h_R(t) = \frac{\tau_1^2 + \tau_2^2}{\tau_1 \tau_2} \exp(-t/\tau_2) \sin(t/\tau_1), \quad (5.12)$$

where $\tau_1 = 1/(\Omega_R^2 - \Gamma_R^2)^{1/2} \approx 10$ fs, $\tau_2 = 1/\Gamma_R \approx 3.03$ ps. The Fourier transform of $h_R(t)$ leads to the Raman-gain spectrum with a Lorentzian shape as [9]:

$$H_R(\Omega) = \frac{\Omega_R^2}{\Omega_R^2 - \Omega^2 - 2i\Gamma_R\Omega}. \quad (5.13)$$

f_R can be written as $f_R = g_R\Gamma_R/(n_2k_0\Omega_R)$. Then $f_R = 0.0664$ when $n_2 = 2.5 \times 10^{-18}$ m²/W. The number is lower using the theoretical calculation because it does not include any multi-phonon Raman scattering which are included in the experimental data as shown in Fig. 5.1.

So much has been discussed about Raman response of silicon. However, in most cases, spontaneous Raman scattering can be neglected in Equation (5.1) due to the profile of Raman-gain spectrum of silicon material.

5.3 Nonlinear Refractive Index of Silicon

n_2 is a very important parameter in the third-order nonlinear optics in silicon waveguides. Many research groups have carried out measurement of n_2 and β_{TPA} [75]. The published data of n_2 differ by great amount, varying from 2.5×10^{-18} m²/W to 14.5×10^{-18} m²/W; while measurement of β_{TPA} is more stable, its value changes from 4.4×10^{-12} m/W to 9×10^{-12} m/W. This adds confusion to researchers. We need to pick up a number in our study, and we also should be able to justify our choice.

In fact, it is not very instructive to compare different absolute values of n_2 and β_{TPA} that are measured using different materials and different methods. However, it is useful to use the nonlinear figure of merit F_n defined as the ratio of n_2 and β_{TPA} . This ratio eliminates some of the uncertainties because the measurements of n_2 and β_{TPA} involve the same material and the same method. There are two ways to define F_n depending on whether n_2 is in the numerator or in the denominator. Since we are more interested in SPM, we prefer to define the nonlinear figure of merit as $F_n = n_2/(\lambda\beta_{\text{TPA}})$.

Table 5.1 gives some of the measured values of n_2 and β_{TPA} by different groups. In the table, the maximum value of F_n is 1.56, however their data is from the estimation of the nonlinear phase shift which is not accurate especially for silicon waveguides because of the severe TPA and free-carrier effects. From the table, we see that F_n converges to a value of 0.34. So the measurements of References [67, 71, 79] are more acceptable. We choose to use the numbers from Ref. [67] partially because it is the work of our research group. From these measurements [67], we can estimate that at $1.55 \mu\text{m}$, $n_2 \approx 2.5 \times 10^{-18}$ m²/W and $\beta_{\text{TPA}} \approx 5 \times 10^{-12}$ m/W. We use this set of values for our further studies.

n_2 ($\times 10^{-18}$ m ² /W)	β_{TPA} ($\times 10^{-12}$ m/W)	λ (μm)	F_n	Reference
6	4.5	1.536	0.87	[76]
7	9	1.53	0.51	[77]
14.5	6	1.55	1.56	[78]
2.41	4.77	1.5	0.34	[67]
4.5	7.9	1.54	0.37	[71]
4.125	7.9	1.55	0.34	[79]

Table 5.1: Measurements of n_2 , β_{TPA} and the corresponding nonlinear figure of merit of silicon by different research groups.

5.4 Summary

In summary, we have discussed a complete theoretical framework for the nonlinear pulse propagation in silicon waveguides that includes dispersion, linear loss, self-phase modulation, two-photon absorption, Raman scattering, free-carrier absorption, and free-carrier dispersion. Next, the Raman response function was discussed in detail to reveal its polarization selection properties and its percentage contribution to the total nonlinear response. We also show that spontaneous Raman scattering in SOI waveguides is negligible in most cases. Finally, we briefly discuss the experimental measurement of nonlinear parameters n_2 and β_{TPA} , and we justified our choice of the value $n_2 \approx 2.5 \times 10^{-18}$ m²/W and $\beta_{\text{TPA}} \approx 5 \times 10^{-12}$ m/W.

6 Self-phase Modulation in the Presence of Two-Photon Absorption

In this chapter, we give a simplified model to describe the self-phase modulation process for pulses propagating through an SOI waveguide in a single TE or TM mode. We use this model to study the effects of two-photon absorption (TPA) on the self-phase modulation process in silicon waveguides while including both free-carrier absorption (FCA) and free-carrier dispersion (FCD). An analytical solution is provided in the case in which the density of the generated carriers is relatively low; it is useful for estimating the spectral bandwidth of output pulses at low repetition rates. The free-carrier effects are studied numerically with emphasis on their role on the nonlinear phase shift and spectral broadening. We also consider how the repetition rate of a pulse train affects the SPM process. Experiments on SPM-induced spectral broadening are carried out. The experimental results show significant SPM induced spectrum broadening and blue shifted spectra in silicon waveguides. And the spectra show polarization dependent features.

6.1 Self-phase Modulation: Theoretical

The phenomenon of SPM in SOI waveguides plays an important role as it leads to chirping and spectral broadening of ultrashort pulses [25, 77, 80]. In practice, TPA limits the extent of SPM through nonlinear absorption and generation of free carriers that not only absorb light (FCA) but also modify the refractive index (FCD).

6.1.1 Theoretical Model

In order to study the impact of the TPA, FCA, and FCD on SPM analytically or numerically, we need a theoretical model to describe the process. The nonlinear Schrödinger equation (NLSE) (5.1) is a complete model for the study of nonlinear phenomena in silicon waveguides. However we can simplify it greatly to study the SPM process. First we assume that light propagates only in TE or TM mode so that we can neglect the coupling terms. Second, we assume that the bandwidth of the pulse spectrum is less than 15.6 THz ($\Delta\lambda < 125$ nm at $\lambda_0 = 1.55$ μm), which is almost always true, so that we can neglect the Raman term. Third, we assume that the pulse bandwidth is not too large so that we can neglect the ξ term that relates to the frequency dependence of the nonlinear parameter as written in Eq. (5.4), which is also almost always true. Then we can simplify Eq. (5.1) greatly and rewrite the NLSE for the intensity of the pulse as [73]:

$$\frac{\partial E}{\partial z} + \frac{i\beta_2}{2} \frac{\partial^2 E}{\partial t^2} = ik_0 n_2 (1 + ir) |E|^2 E - \frac{\sigma}{2} (1 + i\mu) N_c E - \alpha_l E / 2, \quad (6.1)$$

where E is the intensity of the electric-field envelope of the pulse, $k_0 = 2\pi/\lambda$, β_2 is the dispersion parameter at the input wavelength λ , n_2 is the Kerr coefficient, σ is the FCA coefficient, and α_l accounts for linear losses. The dimensionless parameter r governs the relative importance of TPA and is defined as $r = \beta_{\text{TPA}} / (2k_0 n_2) = 1 / (4\pi F_n)$, where F_n is the nonlinear figure of merit. The second dimensionless parameter μ governs the impact of FCD and is analogous to the linewidth enhancement factor well known in the

context of semiconductor lasers. The TPA-induced free-carrier density N_c is governed by the rate equation Eq. (5.3).

The parameters appearing in Eqs. (6.1) and (5.3) depend on the carrier wavelength of the input pulses, chosen to be $1.55 \mu\text{m}$ as this spectral region is most relevant for silicon photonics. At this wavelength, $n_2 = 2.5 \times 10^{-18} \text{ m}^2/\text{W}$, $\beta_{\text{TPA}} = 5 \times 10^{-12} \text{ m/W}$, and $\sigma = 1.45 \times 10^{-21} \text{ m}^2$ [21], resulting in $r = 0.25$. The parameter μ is estimated using $\mu = 2\zeta k_0/\sigma$ with $\zeta = 1.35 \times 10^{-27} \text{ m}^3$ [42] and is found to be close to 7.55. A relatively large value of μ indicates that the FCD effects are important for silicon waveguides and must be included. Note that the effective values of these parameters may change for small-size waveguides [80, 81]. Eq. (6.1) is similar to Eq. (5.10) except that Eq. (6.1) describes the intensity of the pulse, while Eq. (5.10) describes the amplitude of the pulse.

6.1.2 Single-Pulse Approximation

In general, Eqs. (6.1) and (5.3) need to be solved numerically. However, under certain conditions, an approximate analytic solution is possible. First, dispersive effects can be neglected for picosecond pulses because the waveguide length is typically much shorter than the dispersion length, $L_D = T_0^2/|\beta_2|$, where T_0 is the pulse width. Second, if we assume that the repetition rate R_p of the pulses is low ($R_p \tau_c \ll 1$) and their peak intensity is not too high, N_c remains low enough that we can neglect both FCA and FCD. We estimate that N_c is negligible when the input peak intensity I_0 satisfies the condition $I_0 \ll 3h\nu_0/(\sigma T_0)$. For example, $I_0 \ll 2.7 \text{ GW/cm}^2$ for $T_0 = 10 \text{ ps}$. If we set $N_c = 0$ and $\beta_2 = 0$ in Eq. (6.1), we get

$$\frac{\partial E}{\partial z} = ik_0 n_2 (1 + ir) |E|^2 E - \frac{\alpha_l}{2} E. \quad (6.2)$$

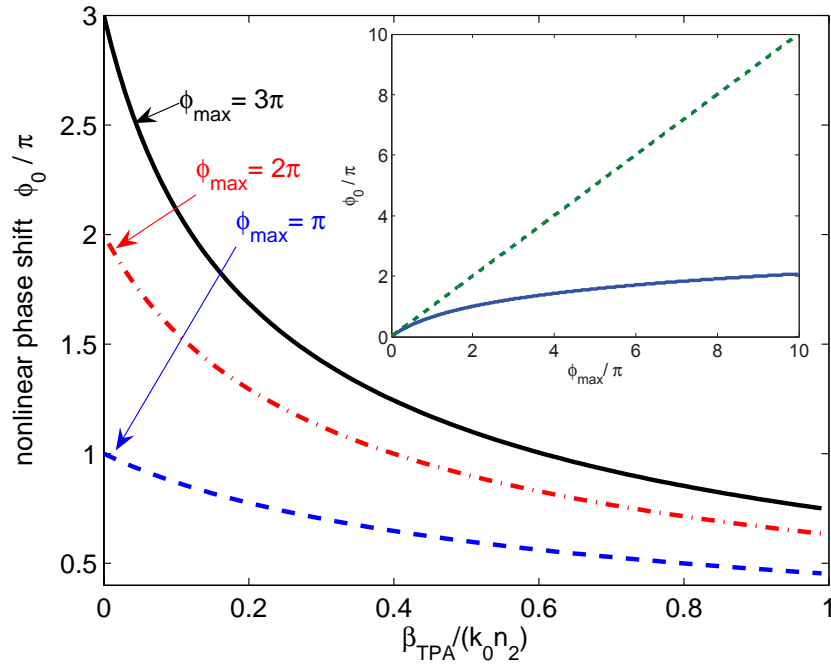


Figure 6.1: Reduction in nonlinear phase shift at the pulse center because of TPA inside a silicon waveguide for $\phi_{\text{max}} = \pi$, 2π , and 3π . The inset shows ϕ_0 as a function of ϕ_{max} using $r = 0.25$; dashed curve shows the $r = 0$ case.

Substituting $E = \sqrt{I} \exp(i\phi - \alpha_l z/2)$ and solving the resulting equations for intensity I and phase ϕ , we get

$$I(L, t) = \frac{I(0, t) \exp(-\alpha_l L)}{1 + 2k_0 n_2 r I(0, t) L_{\text{eff}}}, \quad (6.3a)$$

$$\phi(L, t) = (2r)^{-1} \ln[1 + 2k_0 n_2 r I(0, t) L_{\text{eff}}], \quad (6.3b)$$

where $L_{\text{eff}} = (1 - e^{-\alpha_l L})/\alpha_l$ is the effective length for a waveguide of length L .

The preceding solution shows how the intensity and SPM are affected by the TPA parameter r . In the limit $r \rightarrow 0$ (no TPA), we recover the standard result used for fibers [66], and the maximum nonlinear phase shift at the pulse center is $\phi_{\text{max}} = k_0 n_2 I_0 L_{\text{eff}}$. In the presence of TPA, the phase shift at the pulse center becomes $\phi_0 \equiv \phi(L, 0) = \ln(1 + 2r\phi_{\text{max}})/(2r)$. This phase shift is plotted in Fig. 6.1 as a function of $2r$ for three values of ϕ_{max} . As one may expect, TPA reduces the SPM-induced phase shift, and the

reduction becomes more severe at higher input intensity levels because of a logarithmic growth of ϕ_0 with intensity. This logarithmic growth is seen more clearly in the inset, where we plot ϕ_0 as a function of ϕ_{\max} using $r = 0.25$ (the value estimated for Si at $1.55 \mu\text{m}$) and compare it with the linear growth (dashed line). Clearly, the nonlinear phase shift is severely limited by TPA at high intensity levels.

Next, we focus on the case that the input intensity is high enough that TPA-generated carriers and the associated FCA and FCD cannot be neglected. In this case, we solve Eqs. (6.1) and (5.3) numerically and focus on a specific SOI waveguide of 2-cm length with $\alpha_l = 1 \text{ dB/cm}$, $\beta_2 = \pm 1 \text{ ps}^2/\text{m}$, and a carrier lifetime of $\tau_c = 1 \text{ ns}$. The $1.55\text{-}\mu\text{m}$ input pulses have a Gaussian shape with the intensity profile $I(0, t) = I_0 \exp(-t^2/T_0^2)$. We choose $T_0 = 10 \text{ ps}$.

The top row of Fig. 6.2 shows the output pulse spectra at two different input intensities when all effects are included (solid curves). The first plot corresponds to $\phi_{\max} = 1.5\pi$, but $\phi_{\max} = 7.5\pi$ for the second one. The dashed curves based on the analytic solution include TPA ($r = 0.25$) but neglect free-carrier effects. Based on the limiting value of input intensity for which our analytic model holds, FCA and FCD effects are relatively small in the first case but become quite large in the second case. The dotted curves show the $r = 0$ case (no TPA). Clearly, the TPA effect becomes strong enough for $I_0 = 6 \text{ GW/cm}^2$ that the spectral width is reduced from 5 to $< 2 \text{ nm}$. Note that our analytical model provides a reasonable estimate of the spectral bandwidth even when input intensity levels are so high that N_c is not negligible. This is so because free carriers affect mostly the spectral shape. We can use this feature to predict the spectral bandwidth analytically from Eq. (6.3b) [66]. The spectra in Fig. 6.2 also agree qualitatively with recent experiments [80].

An important feature to note in Fig. 6.2 is that, while TPA leaves the pulse spectrum symmetric, the free carriers produced by TPA make it considerably asymmetric. In particular, free carriers affect mostly the “red” part of the spectrum; the “blue” part remains almost unchanged at low intensity levels. The question is whether this asym-

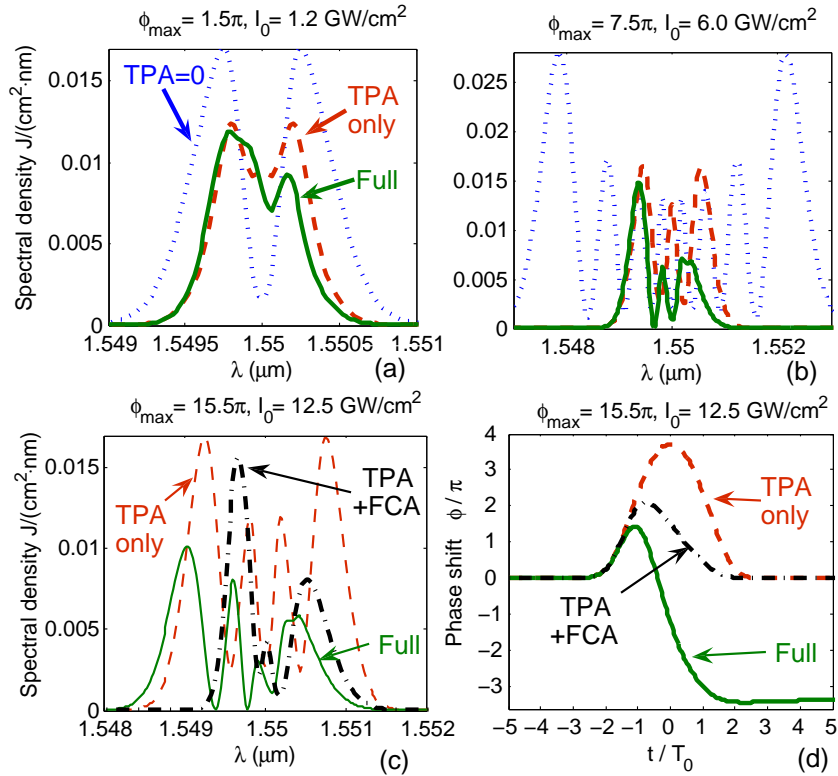


Figure 6.2: SPM-broadened pulse spectra (solid curves) at the end of a 2-cm-long SOI waveguide at three input intensities such that $\phi_{\max} = 1.5\pi$, 7.5π , and 15.5π . Dashed curves include TPA but neglect FCA and FCD effects; dotted curves neglect TPA as well. The nonlinear phase profiles in the three situations are shown in the last plot for $\phi_{\max} = 15.5\pi$.

metry is introduced by FCA, FCD, or both of them. To answer this question, we show in Fig. 6.2(c) pulse spectra at an intensity level of 12.5 GW/cm^2 under the influence of TPA only (dashed curve), TPA and FCA (dot-dashed curve), and all three effects (solid curve). The spectrum becomes narrower and asymmetric when FCA is included without FCD ($\mu = 0$). The effect of FCD ($\mu = 7.55$) is to broaden the spectrum and shift it toward the “blue” side. To understand these features, we show in Fig. 6.2(d), the nonlinear phase shift across the pulse in the three cases. The phase profile is symmetric in the case of TPA only, becomes asymmetric when FCA is included, and develops

negative values in the pulse tails when FCD is included.

Physically, changes in the nonlinear phase shift result from the time-dependent nature of the carrier-density buildup at any point in the waveguide. Near the leading edge of the pulse, $N_c \approx 0$. As the pulse passes through that location, N_c builds up and continues to increase even after the pulse peak has passed. We can estimate the profile of $N_c(t)$ by solving Eq. (5.3) approximately near the front end of the waveguide where $|E(z,t)|^2$ is close to its input. Noting that pulse width $T_0 \ll \tau_c$, the τ_c term can be ignored as carriers do not have enough time to recombine over the pulse duration. The carrier density is then given by

$$N_c(t) \approx \frac{\beta_{\text{TPA}} I_0^2 T_0}{2h\nu_0} \sqrt{\frac{\pi}{8}} \left[1 + \operatorname{erf} \left(\frac{\sqrt{2}t}{T_0} \right) \right] \quad (6.4)$$

After the pulse has passed through the input end, $N_c \approx 3 \times 10^{18} \text{ cm}^{-3}$ for the parameter values used in our study. Absorption by these carriers reduces the phase shift in an asymmetric fashion, as seen by the dot-dashed curve in Fig. 6.2(d).

To understand the role of FCD, we first note that the FCD-induced phase shift has a sign opposite to that of the Kerr effect as seen in Eq. (6.1). This can be understood by noting that free carriers reduce the refractive index while the Kerr effect increases it. Physically speaking, the total nonlinear phase shift ϕ has contributions from these two effects [82]. Because of the opposite signs associated with them, the total nonlinear phase shift is reduced all across the pulse (compared with the TPA only situation). In particular, ϕ becomes 0 at a certain time and negative after that, as shown clearly in Fig. 6.2(d). The blue shift seen in Fig. 6.2(c) originates from such negative values of ϕ . The pulse spectrum broadens because of FCD (compared with the dot-dashed curve) because ϕ changes rapidly over a short time interval.

6.1.3 Pulse Trains with Different Repetition Rates

We next consider the impact of repetition rate R_p associated with a pulse train on SPM-induced spectral broadening. The important dimensionless parameter is $R_p \tau_c$. As long

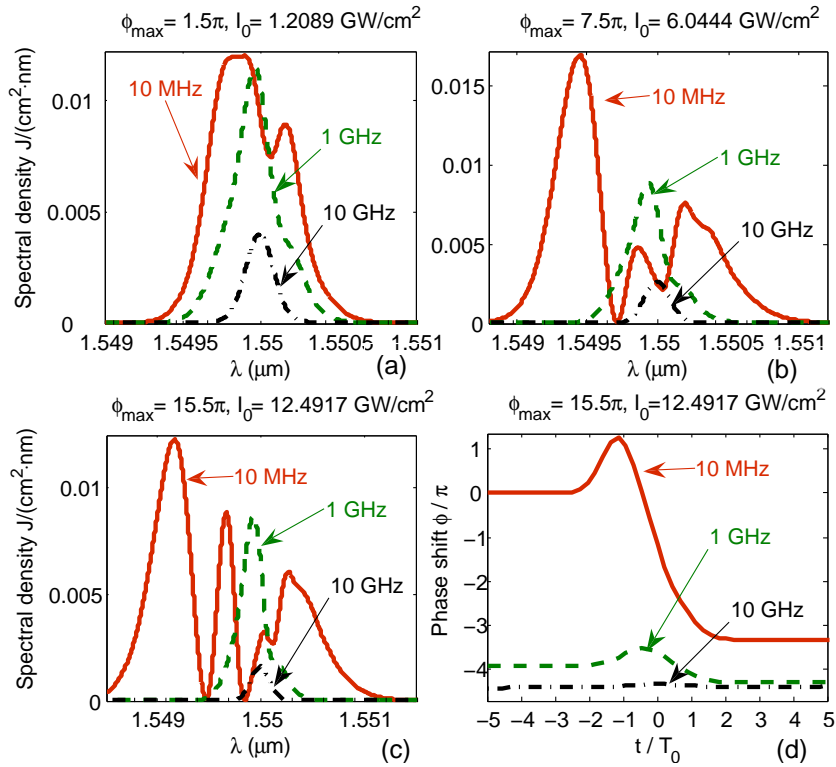


Figure 6.3: Pulse spectra at the same three intensity levels as in Fig. 6.2 except that all effects are included and three repetition rates are considered. The nonlinear phase shift at three different repetition rates is shown in part (d) at $I_0 = 12.5 \text{ GW/cm}^2$.

as $R_p \tau_c \ll 1$, the preceding results shown in Fig. 6.2 remains reasonably accurate. However, if $R_p \tau_c$ is close to or exceeds 1, the situation changes dramatically because carriers produced by a pulse do not have enough time to recombine before the next pulse arrives. As a result, the density of carriers from pulse to pulse increases until a steady-state is reached. In numerical simulations, we obtain this steady-state value by propagating a large number of pulses. The characteristic time needed to reach the steady state is 4 to 5 τ_c . Since $N_c(z, t)$ then follows a periodic pattern, we can focus on one pulse.

Fig. 6.3 shows the pulse spectra at three intensity levels under conditions identical to those in Fig. 6.2 except that all effects are included and the pulse repetition rate is changed from a relatively low value of 10 MHz to a relatively high value of 10 GHz. The 10-MHz curves (solid lines) are identical to those shown in Fig. 6.2 as $R_p \tau_c =$

0.01 for them. The 1-GHz curves (dashed lines) represent the intermediate case of $R_p \tau_c = 1$. The 10-GHz case (dot-dashed lines) corresponds to $R_p \tau_c = 10$ and represents the worst-case scenario in which the background value of the carrier density becomes excessively large. The main conclusion is that the parameter $R_p \tau_c$ should be ≤ 0.2 if SPM-induced spectral broadening is desirable. In practical terms, the carrier lifetime should be reduced to below 20 ps if the SOI waveguide is to operate at a bit rate of 10 Gb/s that is used commonly for telecommunication applications. One way to reduce the carrier lifetime is to use a reverse-biased p-i-n diode structure to remove the carriers [65].

In summary, we have presented a comprehensive study of the SPM phenomenon in SOI waveguides in the presence of the TPA, FCA and FCD effects. The FCA and FCD effects are studied numerically for a better understanding of their role on SPM-induced chirping and spectral broadening. We also studied how the repetition rate of a pulse train affects the SPM process.

6.2 Self-phase Modulation: Experimental

In order to better understand the physics of SPM together with all the other nonlinear interactions, we did the experiment of SPM in a 3-mm long SOI waveguide. The cross section of the waveguide is $600 \text{ nm} \times 400 \text{ nm}$. There are two normal tapering sections on both sides of the 3-mm long main waveguide to improve the coupling efficiency. Numerical calculations with the FDFD method show that the ZDWL of the TM mode is $1.27 \mu\text{m}$, while ZDWL of the TE mode is $1.38 \mu\text{m}$. We use two single-mode tapered fiber lenses (Nanonics Imaging Ltd.) to couple light into and out of the waveguides as shown in Fig. 2.2. The laser source is a mode-locked fiber laser (PolarOnyx Mercury 1000) with average power as high as 120 mW after the EDFA. The pulse width is measured to be around 200–300 fs, and the period of pulses is 22 ns. So the peak power can be as high as 10 kW. The central wavelength is 1564 nm with a dispersive-wave

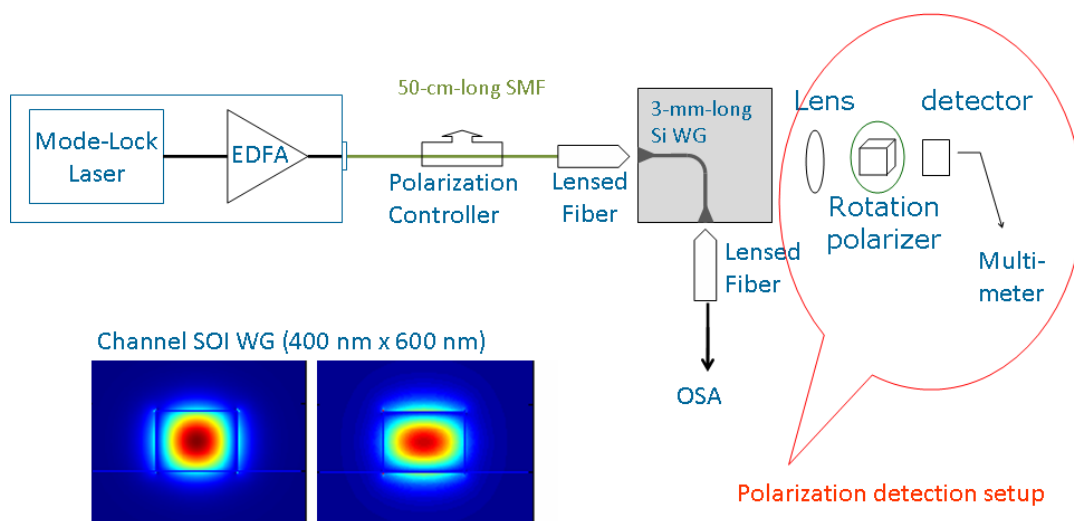


Figure 6.4: Experimental setup for SPM. A 50-cm long tapered fiber lens is used for coupling light into the waveguide. A polarization controller placed on the input side of the tapered fiber is used to control the input as a TE mode or a TM mode of the SOI waveguide. Another setup on the other side of the waveguide is for the purpose of testing if the input is a TE mode or a TM mode.

peak located at 1574 nm. The experimental setup is shown in Fig. 6.4.

In our first attempt, we used a piece of fiber lens that is 35-cm long to couple light from the laser source to the waveguide. The polarization of light before coupling into the waveguide was in the TE direction. We obtained pulse spectra over a wide range of input peak powers by varying the driving current of the EDFA from 100 to 500 mA. We then plot the entire set of spectra as a spectrograph in which the driving current is along the x axis, wavelength along the y axis, and the spectral intensities are represented by color. The results are shown in Figure 6.5. The left figure shows the spectrograph after the 35-cm long single mode tapered fiber lens and before light enters the SOI waveguide. The right figure shows the spectrograph after the SOI waveguide. The average power out of the EDFA at different driving current is shown in Table 6.1. If we assume that about 1% of the total power is coupled into the waveguide (20 dB coupling loss), then the average input power and the peak input power at the beginning of the

Driving Current (mA)	100	200	300	400	500
Average Power (mW)	9	23	40	71	126
Input Average Power (mW)	0.09	0.23	0.4	0.71	1.26
Input Peak Power (W)	7.38	16.02	25.81	44.92	74.83

Table 6.1: The relationship between the driving current of the EDFA and the estimated input power at the input end of the SOI waveguide.

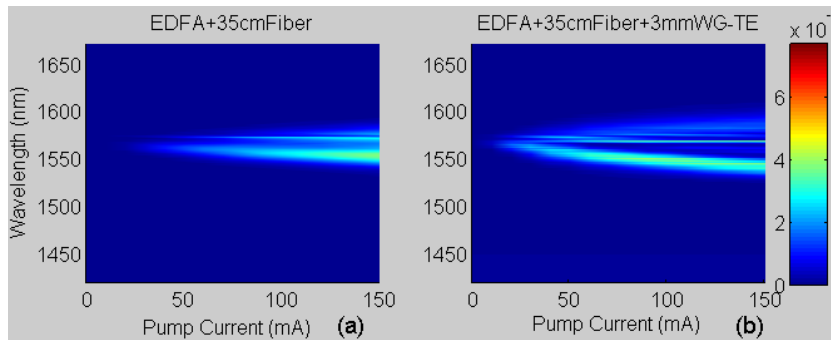


Figure 6.5: SPM spectra at low input power levels. SPM experiment using a 35-cm long tapered fiber lens for coupling: (a) Spectrum after the EDFA and the 35-cm long fiber; (b) Spectrum after the SOI wave-guide.

waveguide can be estimated by the relation $P_0 = P_{ave}T_p/(2T_0) \approx P_{ave} \times 10^5$ if we assume that the pulse period is $T_p = 22$ ns and the pulse width parameter $T_0 = T_{FWHM}/1.76$ for a hyperbolic secant pulse shape. T_{FWHM} are given in Table 9.1 in Chapter 9.

In the first experiment, the fiber for coupling light into the waveguide was too short to incorporate a polarization controller. So we extended the fiber to be 50 cm long and used a polarization controller to choose the mode that light will propagate inside the waveguide. The results are shown in Figure 6.6. The upper left figure shows the spectra immediately after the EDFA of the laser source; the upper right figure shows the spectra after the EDFA and the 50-cm long single mode fiber; the lower left figure shows the output spectra of the TE mode after the 3-mm long SOI waveguide; the lower right figure shows the output spectra of the TM mode after the SOI waveguide.

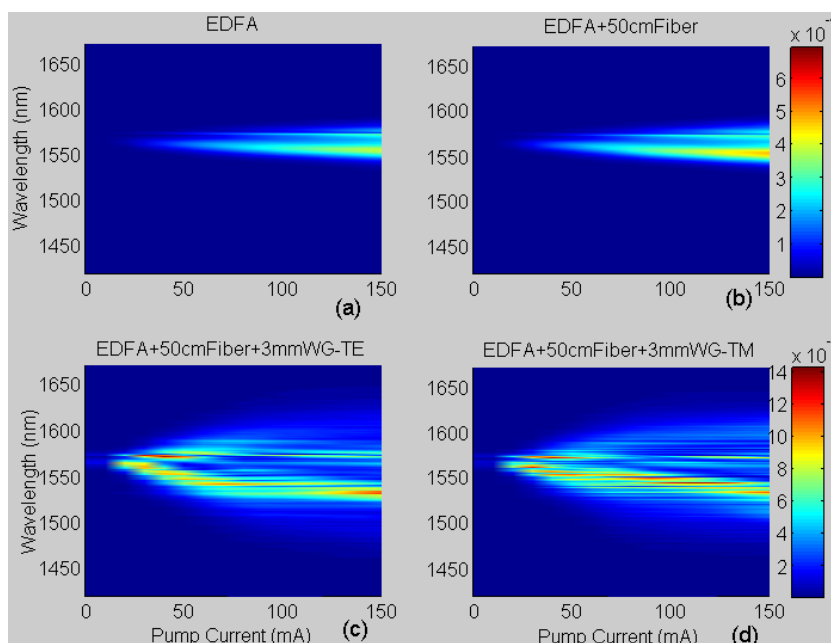


Figure 6.6: SPM spectra at low input power levels. SPM experiment using a 50-cm long fiber lens for coupling: (a) Spectrum after the EDFA of the laser source; (b) Spectrum after the EDFA and the 50-cm long single mode fiber; (c) Spectrum of TE mode after the SOI waveguide; (d) Spectrum of TM mode after the SOI waveguide.

In all the figures, there is a bright line at around 1574 nm. This is the wavelength of the dispersive wave associated with our mode-locked fiber laser. It does not participate in the nonlinear processes. From the experimental data, we see that the spectrum of the mode-locked pulses is broadened by the EDFA as the gain increases. The 35-cm and 50-cm long lensed fibers broaden the spectrum further. Additional broadening on the red side occurs in the case of 50-cm long fiber because of intrapulse Raman scattering. In the case of a 35-cm long fiber, the spectrum at the input of the waveguide is less wide, and the spectra in Fig. 6.5(b) show that the whole spectrum mainly splits into two parts because of SPM. This figure for the TE mode also shows a continuous blue shift because of the FCD effect. However this blue shift saturates at higher input power, which means that the optical power propagating inside the waveguide is limited by the TPA process instead of the FCA process. This saturation is seen again in Fig. 6.6(c) for TE mode

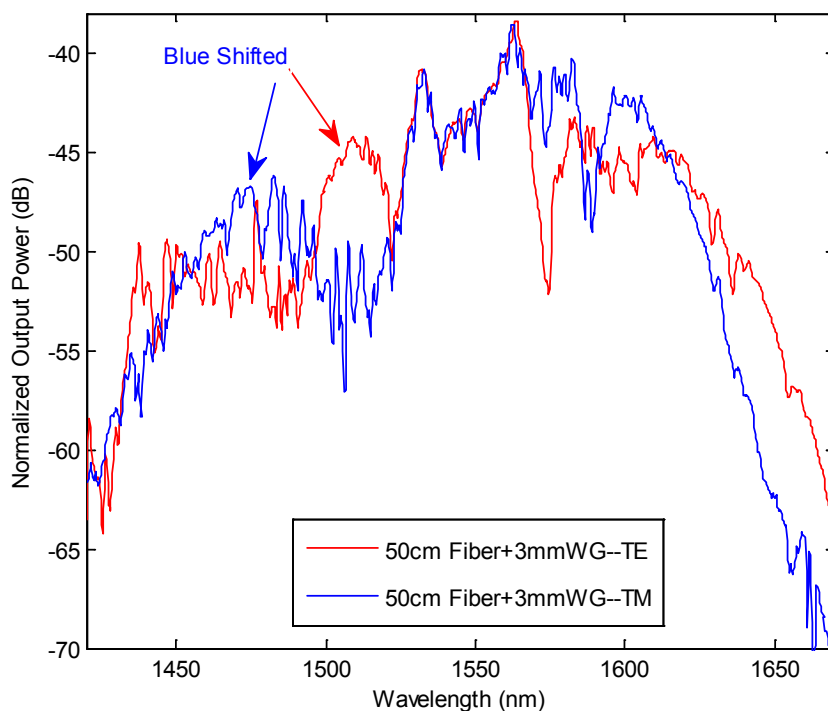


Figure 6.7: SPM spectra when the driving current is 500 mA. solid red line: spectrum after the 3-mm SOI waveguide in TE mode using the 50-cm long fiber; solid blue line: spectrum after the 3-mm SOI waveguide in TM mode using the 50-cm long fiber.

propagation with a 50-cm long fiber. Fig. 6.6(c) for the TE mode and Fig. 6.6(d) for the TM mode show similar patterns with increasing input powers. However, Fig. 6.6(d) for the TM mode does not show the saturation of the blue shift. Comparing the spectrum in Fig. 6.6(c) and (d) with that in (a) and (b), we see much more significant spectrum broadening happening inside an SOI waveguide that is only 3 mm long as comparing with a silica fiber that is 50 cm long, which is about 170 times longer than the silicon waveguide.

The spectrographs in Fig. 6.5 and 6.6 do not reveal fine structure in the pulse spectra very clearly. In order to see the spectrum in more detail, we plot the spectrum of the output pulse at a driving current of 500 mA in different situations. In Fig. 6.7, we plot the output spectra of the 3-mm-long waveguide in both the TE and TM modes using the 50-cm long fiber. The y-axis is plotted on a log scale. The output spectra of

TE and TM modes share similar patterns. The TE spectrum shows more red shift at lower power levels and a saturated blue shift, while the TM spectrum shows less red shift at lower power levels but an unsaturated blue shift. More numerical simulations are needed to understand the physics better. The blue shift is associated with the free-carrier dispersion [73]. It seems that the free-carrier dynamics is different for the two polarization situations.

6.3 Summary

In summary, we have presented a comprehensive study of the SPM phenomenon in SOI waveguides in the presence of the TPA, FCA and FCD effects. The FCA and FCD effects are studied numerically for a better understanding of their role on SPM-induced chirping and spectral broadening. The impact of these effects on SPM is analyzed both analytically and numerically with an emphasis on the physics behind them. We also considered pulse trains to explore how the repetition rate of a pulse train affects the SPM process. Experiments on SPM-induced spectral broadening are carried out. From the data, we see significant SPM induced spectrum broadening and blue shifted spectra in silicon waveguides. And the spectra show polarization dependent features.

7 Supercontinuum Generation

In this chapter, we show through numerical simulations that silicon waveguides can be used to create a supercontinuum extending over 350 nm or more by launching femtosecond pulses and propagating them as higher-order solitons. The physical process behind supercontinuum generation (SCG) is related to self-phase modulation, soliton fission, and generation of Cherenkov radiation. In contrast with optical fibers, stimulated Raman scattering plays little role. We show that two-photon absorption (TPA) and free-carrier absorption (FCA) are not detrimental to the supercontinuum process, even though TPA reduces the spectral broadening to some extent. This scheme should prove useful for practical applications as a relatively short waveguide (length < 1 cm) with low-energy (< 1 pJ) pulses can be used [52]. Preliminary experiments are carried out, and the results show spectrum broadened as wide as 160 nm.

7.1 Physics of Supercontinuum Process

When optical pulses propagate through an optical waveguide, their temporal and spectral evolution is affected not only by a number of nonlinear effects such as SPM, XPM, FWM, and SRS, but also by the dispersive properties of the fiber. All of these nonlinear processes are capable of generating new frequencies within the pulse spectrum. It turns out that, for sufficiently intense pulses, the pulse spectrum becomes so broad that it may

extend over a frequency range exceeding 100 THz. Such extreme spectral broadening is referred to as supercontinuum generation [66, 83].

In the context of optical fibers, the nonlinear mechanisms that are responsible for broadening the spectrum of an ultrafast pulse includes SPM, SRS, FWM, soliton fission, and Cherenkov radiation [66, 84].

SPM can produce considerable spectral broadening at the fiber output. The spectral broadening factor is approximately given by the maximum SPM-induced phase shift, $\phi_{\max} = \gamma P_0 L_{\text{eff}}$, where P_0 is the peak power of the pulse and L_{eff} is the effective fiber length. For typical values of the experimental parameters used, this spectral broadening factor is ~ 10 [66].

Another nonlinear mechanism that can generate new wavelengths is SRS. If the input peak power P_0 is large enough, SRS creates a Stokes band on the long-wavelength side, shifted by about 13 THz from the center of the pulse spectrum. Even if the peak power is not large enough to reach the Raman threshold, SRS can amplify the pulse spectrum on the long-wavelength side as soon as SPM broadens it by 5 nm or more. Clearly, SRS would affect any supercontinuum by enhancing it selectively on the long wavelength side, thus making it asymmetric. However, SRS cannot generate any frequency components on the short-wavelength side.

FWM is the nonlinear process that can create sidebands on both sides of the pulse spectrum, provided a phase-matching condition is satisfied, and it is invariably behind any supercontinuum generated using optical fibers. FWM is also the reason why dispersive properties of the fiber play a critical role in the formation of a supercontinuum. Indeed, because of a large spectral bandwidth associated with any supercontinuum, the group-velocity dispersion (GVD) parameter β_2 cannot be treated as a constant over the entire bandwidth, and its wavelength dependence should be included through higher-order dispersion parameters in any theoretical modeling.

In the case of femtosecond pulses, a different physical mechanism called soliton fission plays a critical role in the formation of a supercontinuum in highly nonlinear

fibers. At high peak power levels and anomalous GVD, input pulses correspond to a higher-order soliton whose order is governed by $N = (\gamma P_0 L_D)^{1/2}$, where $L_D = T_0^2/|\beta_2|$ is the dispersion length. Such solitons are perturbed considerably by higher-order effects, such as third-order dispersion and intrapulse Raman scattering, that lead to their fission into much narrower fundamental solitons. The fission of a higher-order soliton produces multiple fundamental solitons. Almost all of these solitons are shorter than the original input pulse, the shortest one being narrower by a factor of $2N - 1$. For femtosecond input pulses, the individual solitons have a relatively wide spectrum (~ 10 THz) and are thus affected by intrapulse Raman scattering that shifts the soliton spectrum toward longer and longer wavelengths with further propagation inside the fiber. As a result, many new spectral components are added on the long-wavelength side of the original pulse spectrum. This process is different from cascaded SRS that creates multiple Stokes bands for picosecond pulses.

The important remaining question is what process creates spectral components on the short-wavelength side of the pulse spectrum. This is where the dispersive properties of the fiber play a critical role. Ultrashort solitons, created through the fission process and perturbed by third- and higher-order dispersion, emit nonsolitonic radiation (NSR) in the form of dispersive waves whose wavelength falls on the short wavelength side in the normal dispersion region of the fiber [66]. This radiation is also known as the Cherenkov radiation [84] that emits at a frequency determined by the underlying phase-matching condition requiring that the dispersive waves propagate at the same phase velocity as the soliton. When solitons are mainly perturbed by the third-order dispersion β_3 , the frequency of Cherenkov radiation is given by [84]

$$\Omega_d \approx -\frac{3\beta_2}{\beta_3} + \frac{\gamma P_s \beta_3}{3\beta_2^2}, \quad (7.1)$$

where P_s is the peak power of the fundamental soliton perturbed by β_3 . In the absence of losses, $P_s = (5/3)^2 P_0$, where P_0 is the input peak power [66].

Although SCG is usually realized by using highly nonlinear fibers, we propose that SOI waveguides are also promising for this application. Similar nonlinear mecha-

nisms should be responsible for the SCG in SOI waveguides. This possibility offers the prospect of an on-chip ultrabroadband source useful for many applications.

7.2 Dispersion Properties

Some key issues need to be considered before we study SCG in SOI waveguides. First of all, dispersion properties are very important for supercontinuum generation. The pulses have to propagate in the anomalous dispersion region but not too far from the zero-dispersion wavelength (ZDWL) [66]. Second, the mode of polarization of the input pulse is also important as it relates to Raman scattering in SOI waveguides. From Chapter 5, we know that for an SOI waveguide fabricated along the $[0 \bar{1} 1]$ direction on the $(1 0 0)$ surface, SRS cannot occur when an input pulse excites the TM mode. To include the impact of SRS, we focus on the TE mode in the study.

We have shown in Chapter 4 that the ZDWL of waveguides can be tailored to fall in the anomalous regime with a suitable design [57]. We have also found that the ZDWL of both the TE and TM modes can be below $1.55 \mu\text{m}$ for a ridge waveguide geometry shown as the inset in Fig. 7.1 when both the width and height of the waveguide are close to $0.8 \mu\text{m}$ [37]. We focus on such a waveguide and assume that $W = 0.8 \mu\text{m}$ and $H = 0.7 \mu\text{m}$. We use the Herzberger-type dispersion formula Equation (3.5) [59] as discussed in Chapter 3. The effective mode index n_{eff} and its wavelength dependence are calculated using the full-vector finite difference mode solver [61]. The ZDWL of the fundamental TE mode is found to be 1496 nm . The effective mode area is $a_{\text{eff}} = 0.32 \mu\text{m}^2$ at $\lambda_0 = 1550 \text{ nm}$. The wavelength dependence of n_{Si} , n_{eff} , and second-order dispersion β_2 are shown in Fig. 7.1. Although such a waveguide supports multiple modes, our analysis shows that the phase velocities and mode profiles differ substantially for the fundamental mode and high-order modes. As a result, intermodal coupling is not likely to participate in the soliton fission process. Although we focus on a specific waveguide geometry, our results should apply to any waveguide designed to

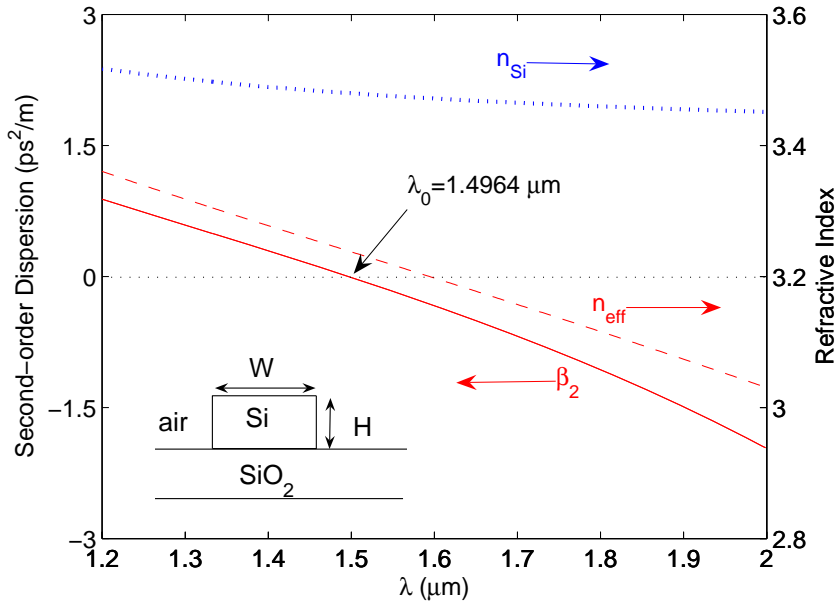


Figure 7.1: Wavelength dependence of n_{Si} (dotted), n_{eff} (dashed), and β_2 (solid) for the fundamental TE mode using the waveguide shown in the inset with $W = 0.8 \mu\text{m}$, and $H = 0.7 \mu\text{m}$.

produce dispersion parameters close to those used here.

7.3 Numerical Simulations

To study supercontinuum generation, we launch a femtosecond pulse polarized such that it excites the fundamental TE mode and propagates in the form of a high-order soliton. Its evolution is governed by the same generalized nonlinear Schrödinger equation Equation (5.1), but simplified similar as Equation (6.1):

$$\begin{aligned} \frac{\partial A}{\partial z} = & \sum_{m=2}^{\infty} \frac{i^{m+1} \beta_m}{m!} \frac{\partial^m A}{\partial t^m} - \frac{\sigma}{2} (1 + i\mu) N_c A - \frac{1}{2} \alpha_l A \\ & + i\gamma(1 + ir) \left(1 + \frac{i}{\omega_0} \frac{\partial}{\partial t} \right) A(z, t) \times \int_{-\infty}^t R(t - \tau) |A(z, \tau)|^2 d\tau, \end{aligned} \quad (7.2)$$

where the nonlinear parameter γ is defined as $\gamma = n_2 k_0 / a_{\text{eff}}$. The other parameters are the same as Equation (6.1). The difference is that $A(z, t)$ describes the amplitude while

$E(z, t) = |A(z, t)|^2/a_{\text{eff}}$ describes the intensity of light. The density N_c produced by TPA is governed by Eq. 5.3. The effective carrier lifetime is estimated to be about 3 ns [72] for the SOI waveguide we use. For femtosecond pulses used here and at relatively low repetition rates, $N_c \leq 2\beta_{\text{TPA}}P_0^2T_0/(3h\nu_0a_{\text{eff}}^2)$, where P_0 is the peak power of a ‘‘sech’’ pulse of width $T_p \approx 1.76T_0$. The wavelength dependence of γ and σ is neglected in this study; it can be included following a standard approach [72].

A soliton of order N is excited if $A(0, t) = \sqrt{P_0} \text{sech}(t/T_0)$ initially, and the input parameters satisfy the condition $N^2 = \text{Re}(\gamma)P_0T_0^2/|\beta_2|$. We solve Eq. (7.2) with the split-step Fourier method [66] for a third-order soliton ($N = 3$) using $T_p = 50$ fs. The peak power P_0 equals 25 W using $n_2 = 2.5 \times 10^{-18}$ m²/W and $\beta_2 = -0.1701$ ps²/m (estimated from Fig. 7.1 at $\lambda_0 = 1.55$ μm). We estimate a maximum carrier density of $N_c \approx 8 \times 10^{21}$ m⁻³, resulting in $\alpha_f = \sigma N_c \approx 11.6$ m⁻¹ after all carriers have been generated. So free-carrier effects do not play a big role in the current situation. This is true especially because the pulse width is so short. Numerically, we solve the coupled set of Eqs. (7.2) and (5.3) to include all time-dependent features of TPA, FCA, and FCD.

For the nonlinear response function $R(t)$ appearing in Eq. (7.2), we use the form $R(t) = (1 - f_R)\delta(t) + f_R h_R(t)$, where the first term governs the nearly instantaneous electronic response and $h_R(t)$ is the Raman response function. The parameter $f_R = 10.32\%$ represents the fractional contribution of the nuclei to the total nonlinear polarization. The functional form of the Raman response function $h_R(t)$ is deduced from the Raman gain spectrum, $g_R(\Omega)$, known to exhibit a narrow Lorentzian peak of ≈ 105 -GHz bandwidth, located 15.6 THz away from the pump frequency [74].

As seen in Eq. (7.2), soliton evolution is affected by dispersion to all orders ($m > 1$). Often, the sum is truncated to include the dispersion terms up to $m = 6$ or 7 [66]. A better approach is to notice that the infinite series can be written in the frequency

domain as

$$\mathcal{F} \left[\sum_{m=2}^{\infty} i \frac{\beta_m}{m!} \frac{\partial^m A}{\partial t^m} \right] = \left[\beta(\omega) - \beta(\omega_0) - \beta_1(\omega_0)(\omega - \omega_0) \right] \tilde{A}(\omega), \quad (7.3)$$

where $\beta(\omega) = n_{\text{eff}}(\omega)\omega/c$, $\beta_1(\omega) = \partial\beta/\partial\omega$, and \mathcal{F} is the Fourier transform operator. We include dispersion to all orders by using Eq. (7.3) with $n_{\text{eff}}(\omega)$ from Fig. 7.1.

In our numerical simulations, we propagate the 50-fs-wide third-order soliton inside a 1.2-cm-long SOI waveguide. Figure 7.2 shows the temporal and spectral profiles at the waveguide output. The features seen here can be understood in terms of soliton fission and Cherenkov radiation. The single third-order soliton evolves into three individual fundamental solitons in the time domain, as seen in Fig. 7.2(a). In Fig. 7.2(b), we see a spectral peak located at $1.31 \mu\text{m}$. We have verified that this spectral feature corresponds to a dispersive wave that produces the long tail in Fig. 7.2(a). This is the so-called Cherenkov radiation, emitted at a frequency determined by Eq. (7.1). In the absence of losses, $P_s = (5/3)^2 P_0$; linear losses and TPA reduce this value all along the waveguide length. As a rough estimate, we use $P_s \approx P_0$ with $\beta_2 = -0.1701 \text{ ps}^2/\text{m}$ and $\beta_3 = 4.12 \times 10^{-3} \text{ ps}^3/\text{m}$ in Eq. (7.1) and find that the wavelength of Cherenkov radiation is around $1.32 \mu\text{m}$. This value agrees with numerical simulations shown in Fig. 7.2. The dominant spectral peak in this figure is red shifted by about 75 nm from the input wavelength. We have verified by setting $f_R = 0$ that this shift is mostly due to self-phase modulation, and not due to SRS. In contrast with silica fibers, SRS plays a minor role in silicon because of its much narrower Raman-gain spectrum, and also the power clamping effect of TPA.

Although the spectrum of the output pulse in Fig. 7.2 extends over 300 nm or so, it is not uniform enough to be useful for practical applications. We have studied the evolution of femtosecond pulses along the waveguide length under a variety of launch conditions. Our results indicate that soliton fission for $N = 3$ occurs within 3 mm after the pulse is launched, and a supercontinuum is formed soon after. In fact, the supercontinuum is much more uniform when it is first formed because it is not much

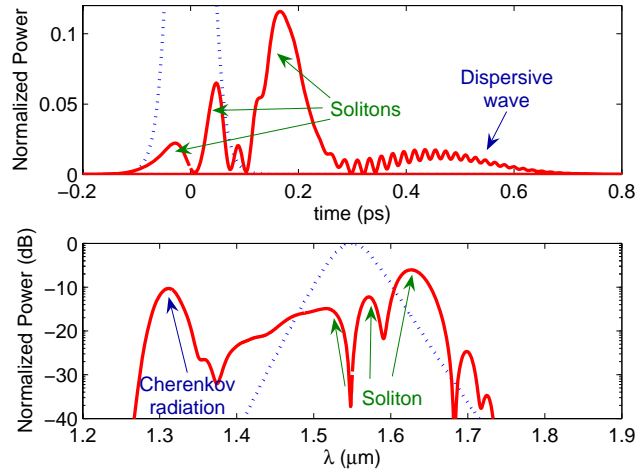


Figure 7.2: Temporal and spectral profiles at the output of 1.2-cm-long SOI waveguide when a 50-fs pulse propagates as a third order soliton. Dotted curves shows, for comparison, the corresponding input profiles.

affected by the TPA. As an example, Fig. 7.3 shows the output spectrum on a semilog scale at a distance of 3 mm under the conditions of Fig. 7.2. The 20-dB bandwidth is close to 420 nm in this case, which covers the entire telecommunication range from 1.3 μm to 1.7 μm . The main point to note is that a 3-mm-long SOI waveguide can produce a relatively broad supercontinuum of acceptable quality, which obviates any bends in the waveguide.

To see what role TPA and FCA play over the 3-mm length, we have repeated the simulation with $\beta_{\text{TPA}} = 0$ so that both of them are absent. The result is also shown in Fig. 7.3. Clearly, TPA reduces the bandwidth of supercontinuum but does not affect much of its flatness. The free carriers generated during this process have a negligible impact on the pulse because, by the time enough free carriers accumulate at a certain location, the 50-fs pulse moves away from that spot. We thus conclude that neither SRS nor FCA plays a significant role during supercontinuum formation in Si waveguides.

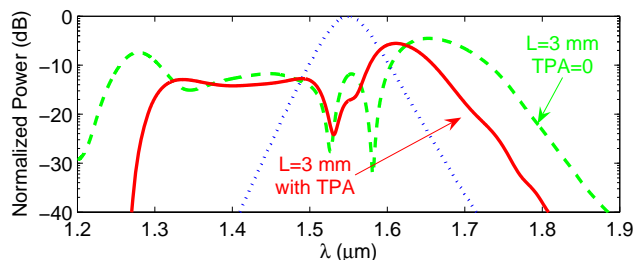


Figure 7.3: Supercontinuum created in a 3-mm long SOI waveguide under the conditions of Fig. 7.2. The dashed curve shows the spectrum when the effects of TPA and FCA are ignored. The dotted curve shows the input pulse spectrum.

7.4 Experiment

Although we predict the ultra-wide spectrum broadening in silicon waveguide, it is difficult to realize it experimentally. The lack of precise dispersion engineering and the lack of ultra-short optical pulses (< 50 fs) are the major issues for supercontinuum generation experiment in SOI waveguide. However, we did some preliminary experiment by coupling in 300-fs pulses with very high peak power into the waveguide. The peak power inside the waveguide is as high as 70 W. The results are shown in Figure 7.4. We see very broad spectra (10 dB bandwidth is around 160 nm) at high input power levels. This is not really supercontinuum generation. But it gives us some knowledge of the ultra-wide spectrum broadening in silicon waveguide.

7.5 Summary

In summary, silicon waveguides can be used to create a supercontinuum extending over 400 nm or more by launching femtosecond pulses and propagating them as higher-order solitons. The physical process behind supercontinuum formation is related to soliton fission, self-phase modulation and generation of Cherenkov radiation. As low-energy (≈ 1 pJ) pulses and relatively short waveguides (length < 1 cm) are sufficient

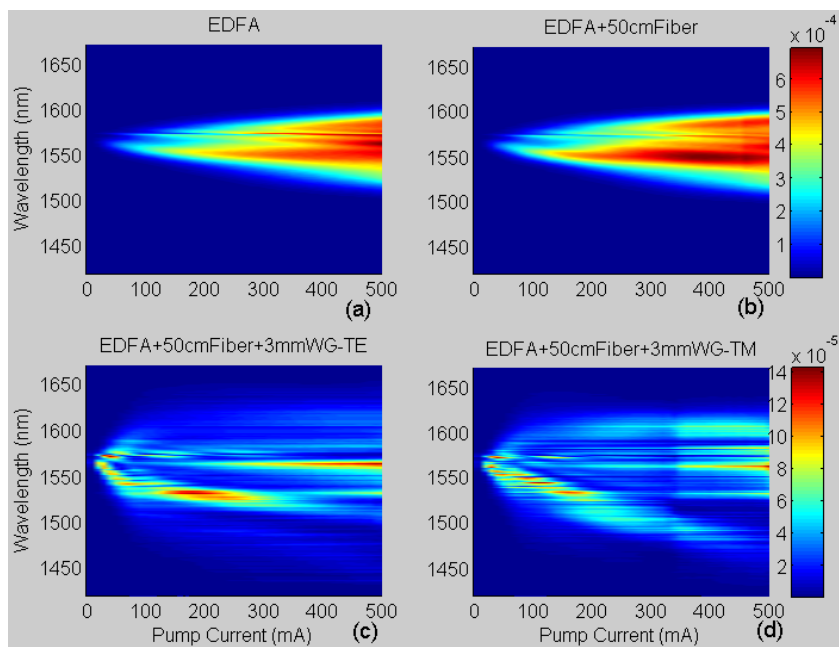


Figure 7.4: SCG spectra at high input power levels. SCG experiment using a 50-cm long fiber lens for coupling: (a) Spectrum after the EDFA of the laser source; (b) Spectrum after the EDFA and the 50-cm long single mode fiber; (c) Spectrum of TE mode after the SOI waveguide; (d) Spectrum of TM mode after the SOI waveguide. Very broad spectra are obtained at high input power levels.

for supercontinuum generation, the proposed scheme should prove useful in practical applications. Some preliminary experiment results are also given.

8 Cross-phase Modulation and Nonlinear Polarization Rotation

In this chapter, we study the nonlinear polarization rotation induced by a pump pulse on a probe beam through cross-phase modulation inside a silicon waveguide and show that this phenomenon can be used to realize a fast Kerr shutter in spite of the free-carrier and walk-off effects. We show that free carriers generated by the pump pulse through two-photon absorption affect the switching process considerably especially with the interaction of walk-off effects. However, numerical simulations reveal that their impact is not detrimental for short pump pulses. In this case, an approximate analytical solution predicts the shape and duration of the switching window with reasonable accuracy [85]. Next we have successfully realized a Kerr shutter experimentally using an SOI waveguide. In the case of polarizer at perpendicular state we see modulated pulses, while in the case of polarizer at parallel state we see dips modulated by cross-TPA at the presence of the pump pulses. Optical autocorrelation traces of the switching window are recorded. Ultra short switching window (< 1 ps) is realized. Numerical simulations agree well with experimental results at lower input pump power.

8.1 Implementation of a Kerr Shutter

All-optical switches based on SOI waveguides are an important component for any integrated optical circuit. Although several switching schemes have been explored in the past [25,43,86,87], a Kerr shutter [66] has not yet been realized. In this chapter we propose and analyze an optical switching scheme in an SOI waveguide through nonlinear polarization rotation (NPR) induced by cross-phase modulation (XPM). Detailed numerical simulations show that the free-carrier effects can be negligible for femtosecond pump pulses. In addition, this scheme does not require a Mach-Zehnder interferometer configuration, therefore this all-optical switch is compact for silicon-based photonic integrated circuits (PIC).

The basic idea behind a Kerr switch is to change the state of polarization of a probe beam inside an SOI waveguide by utilizing nonlinear changes in the refractive index that are produced by an intense pump pulse (NPR through XPM). A polarizer is placed after the waveguide as a polarization analyzer that transmits the probe only when a pump pulse is present to induce a NPR on the probe, thus converting the waveguide into an optical switch. The duration of the switching window may exceed the width of the pump pulse because of the walk-off effects, but its magnitude can be controlled by carefully tailoring the waveguide dispersion, selecting the wavelengths of the pump and probe appropriately, and optimizing the pump power. The birefringence-induced linear polarization rotation can be compensated by a polarization controller at the output end of the waveguide.

We adopt the configuration shown in Fig. 8.1 for our Kerr switch. Pump pulses are polarized along the x axis and propagate as a quasi-TE mode of the SOI waveguide. The weak CW probe, polarized at 45° with respect to the pump, excites both TE and TM modes equally. The phases of the two probe components change through XPM by different amounts, resulting in a net relative nonlinear phase shift that manifests as NPR. The polarizer can be adjusted to block the probe (we call it polarizer at ϕ_\perp) or

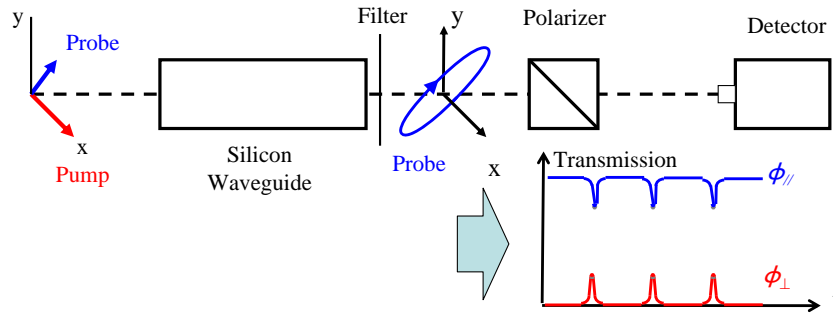


Figure 8.1: Schematic setup of the proposed optical Kerr shutter. The probe undergoes nonlinear polarization rotation inside the silicon waveguide when a pump pulse is present. An optical filter is used to block the pump light. A polarizer works as a polarization analyzer to set the transmission of the system in two output states.

transmit the probe (we call it polarizer at ϕ_{\parallel}). The transmission under the two conditions is also plotted for better understanding.

8.2 Theoretical Analysis

We calculate the XPM-induced phase shift by solving three coupled equations [73, 85]:

$$\frac{\partial E_x}{\partial z} + d_x \frac{\partial E_x}{\partial T} = 2ik_0 n_2 a (1 + ir) I_p E_x - \frac{\sigma}{2} (1 + i\mu) N_c E_x - \frac{\alpha_l}{2} E_x + i(\beta_x - \bar{\beta}) E_x, \quad (8.1)$$

$$\frac{\partial E_y}{\partial z} + d_y \frac{\partial E_y}{\partial T} = 2ik_0 n_2 b (1 + ir) I_p E_y - \frac{\sigma}{2} (1 + i\mu) N_c E_y - \frac{\alpha_l}{2} E_y + i(\beta_y - \bar{\beta}) E_y, \quad (8.2)$$

$$\frac{\partial I_p}{\partial z} = -\beta_{\text{TPA}} I_p^2 - \sigma N_c I_p - \alpha_l I_p, \quad (8.3)$$

where E_x and E_y are the probe amplitudes and $I_p = |E_p|^2$ is the pump intensity. Only the intensity equation is needed for the pump because its phase does not affect the XPM process. The CW probe is assumed to be so weak that it does not induce any nonlinear effects. The pump-induced XPM effect is included through the Kerr parameter n_2 . The coefficients a and b indicate that the strength of XPM depends on the relative polarizations of the pump and probe. In the case of silicon, $a = (1 + \rho)/2$ and $b = \rho/3$, where the anisotropic factor $\rho \approx 1.27$ as discussed in Chapter 5 [9]. The TPA of the

pump is governed by $r = \beta_{\text{TPA}}/(2k_0n_2)$. The free carriers absorb both the pump and probe light, and σ governs the magnitude of this absorption. Equally important is the index change induced by free carriers whose magnitude is controlled by μ . The linear losses are taken to be the same for the pump and probe although they may differ in some situations. The last term in the probe equations accounts for the birefringence resulting from different mode indices n_x and n_y for the TE and TM modes. Here, $\bar{\beta} = (\beta_x + \beta_y)/2$ is the average value of $\beta_x = n_x k_0$ and $\beta_y = n_y k_0$ with $k_0 = 2\pi/\lambda_s$, λ_s being the probe wavelength. The walk-off effects result from different group velocities of the pump and probe components. Since only relative speeds matter, we work in a frame moving at the pump speed and introduce a reduced time $T = t - z/v_{gp}$. Using the notation, $\beta_{1j} = d\beta_j/d\omega = 1/v_{gj}$ with $j = x, y, p$, the two walk-off parameters of the probe are defined as $d_x = \beta_{1x} - \beta_{1p}$ and $d_y = \beta_{1y} - \beta_{1p}$.

Finally, we use the following rate equation for the carrier density $N_c(z, T)$:

$$\frac{\partial N_c}{\partial T} = \frac{\beta_{\text{TPA}}}{2h\nu_p} I_p^2(z, T) - \frac{N_c}{\tau_c}, \quad (8.4)$$

where $h\nu_p$ is the energy of a pump photon and τ_c is the carrier lifetime. To be consistent, we have neglected the terms containing probe intensity, assuming a relatively weak probe.

A numerical solution of Eqs. (8.1)–(8.4) provides a reasonable description of the pump-induced NPR effects. Before discussing the numerical results, we show that an approximate analytic solution is also possible and it can provide considerable physical insight. The simplifying approximation we make is that the carrier density N_c is small enough that its impact is negligible. This approximation is too drastic to be valid in general. However, we show later that it is reasonable for relatively short, not too intense, pump pulses that are widely separated. In this case, the free carriers do not affect much of the switching process. Since the pump equation (8.3) does not depend on the probe, it can be solved easily when $N_c = 0$:

$$I_p(z, T) = \frac{\alpha_l I_0(T) e^{-\alpha_l z}}{\alpha_l + \beta_{\text{TPA}} I_0(T) (1 - e^{-\alpha_l z})}, \quad (8.5)$$

where $I_0(T)$ is the intensity profile of the input pulse launched at $z = 0$. The two probe equations can also be solved analytically because of their linear nature. Introducing $T'_x = T - d_x z$ and the transformation $E_x = A_x e^{-\alpha_l z/2} e^{i(\beta_x - \bar{\beta})z} e^{i\phi_x}$, Eq. (8.1) leads to:

$$\frac{\partial A_x}{\partial z} = -2k_0 n_2 a r I_p A_x, \quad \frac{\partial \phi_x}{\partial z} = 2k_0 n_2 a I_p. \quad (8.6)$$

Both of them can be solved to obtain

$$A_x(z, T'_x) = A_x(0, T'_x) \times \exp \left[-a \int_0^z \frac{\alpha_l e^{-\alpha_l z'} \beta_{\text{TPA}} I_p(0, T'_x + d_x z')}{\alpha_l + \beta_{\text{TPA}} I_p(0, T'_x + d_x z')(1 - e^{-\alpha_l z'})} dz' \right], \quad (8.7)$$

$$\phi_x(z, T'_x) = \frac{a}{r} \int_0^z \frac{\alpha_l e^{-\alpha_l z'} \beta_{\text{TPA}} I_p(0, T'_x + d_x z')}{\alpha_l + \beta_{\text{TPA}} I_p(0, T'_x + d_x z')(1 - e^{-\alpha_l z'})} dz'. \quad (8.8)$$

The solution for A_y is obtained by replacing a with b and the subscript x with y in Eqs. (8.7) and (8.8).

The NPR of the probe beam by the pump beam is governed by the relative phase shift $\Delta\phi = \phi_x - \phi_y$. Notice that the linear birefringence of the waveguide also leads to a phase difference between the two polarization components. This birefringence-induced polarization rotation can be compensated by using a polarization compensator after the waveguide. Another polarizer is needed after the polarization compensator to block the probe in the absence of a pump pulse. Each pump pulse changes probe polarization through NPR such that some probe light is transmitted through the polarizer only over the pump duration. The probe transmission depends on the relative nonlinear phase shift $\Delta\phi$.

8.3 Numerical Simulations

To test the range of validity of the analytic solution, we have solved Eqs. (8.1)–(8.4) numerically for a 5-mm-long SOI waveguide with a cross-section area of $600 \times 450 \text{ nm}^2$. The pump and probe wavelengths are $\lambda_p = 1.56 \text{ }\mu\text{m}$ and $\lambda_s = 1.54 \text{ }\mu\text{m}$. The walk-off parameters are calculated using the dispersion curves for the fundamental TE and

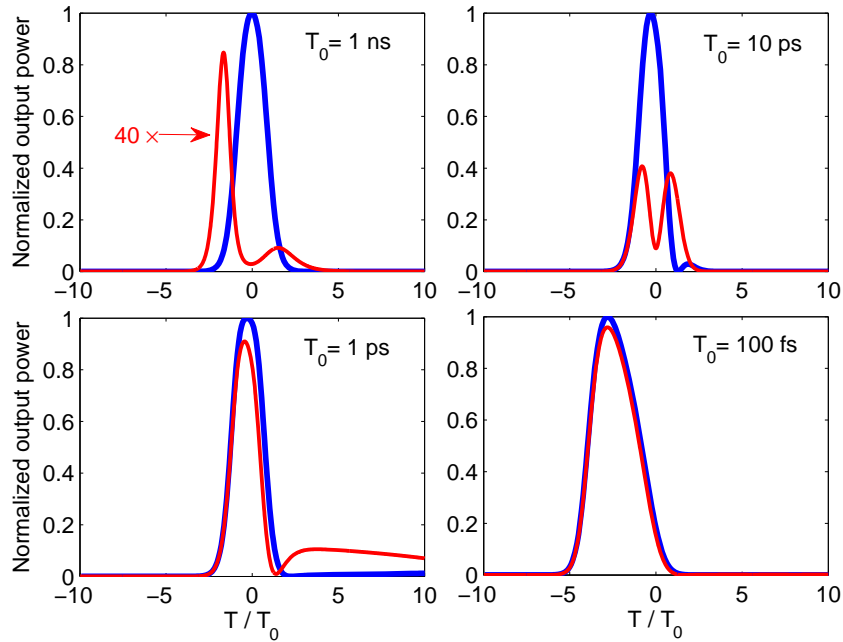


Figure 8.2: Switching windows for 4 different pump-pulse widths. The thinner red curves mark the numerical results while the thicker blue curves show the analytical prediction neglecting the free-carrier effects.

TM modes and are $d_x = -0.78$ ps/cm and $d_y = 30.2$ ps/cm. For the nonlinear parameters, we use the values from our recent measurements [67]: $n_2 = 2.5 \times 10^{-18}$ m²/W, $\beta_{\text{TPA}} = 5 \times 10^{-12}$ m/W. We note that n_2 values in the literature differ by up to a factor of 2 but our results are not too sensitive to the exact value if the device length is adjusted to obtain the same nonlinear phase shift. The other parameters are chosen to be: $\sigma = 1.45 \times 10^{-21}$ m², $\mu = 7.597$ [73], $\tau_c = 1.5$ ns, $\alpha_l = 5$ dB/cm, and $a_{\text{eff}} = 0.1$ μm^2 . The peak power is 4 W for the ‘sech’ pump pulses with $P_p(T) = P_0 \text{sech}(T/T_0)^2$. The width T_0 is varied over a wide range to study the shape and duration of the NPR-induced switching window. The CW power of the input probe is 1 mW to ensure negligible self-phase modulation.

Figure 8.2 compares the switching windows for values of T_0 ranging from 1 ns to as short as 0.1 ps obtained numerically (thin lines) with those predicted analytically (thick lines) by neglecting the free-carrier effects. These results show that free carriers play a

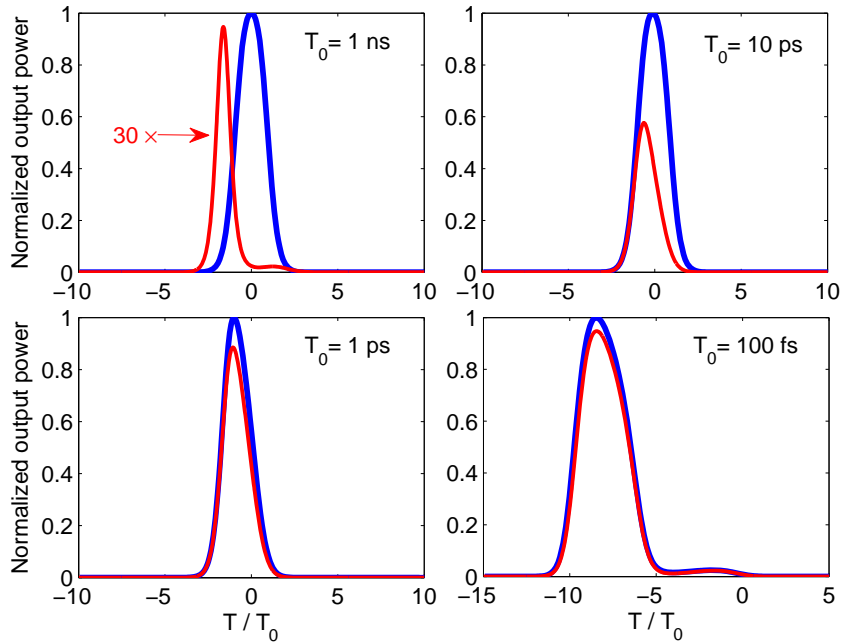


Figure 8.3: Switching windows for the same 4 pump-pulse widths and the same operating conditions used in Fig. 8.2. The only difference is that a square-shape silicon waveguide is employed to minimize walk-off effects.

significant role for pulses much wider than 1 ps but can be neglected for shorter pump pulses. In particular, the switching window is not affected much by free carriers for 100-fs pulses. In the case of 1-ps pump pulses, the switching windows almost coincide except for a low-amplitude tail that results from the interaction between the free-carrier effects and walk-off effect. Free-carrier effects break the temporal symmetry of the probe field. In the presence of group-velocity mismatch, the free-carrier-induced phase shift is not the same for A_x and A_y , resulting in polarization changes that produce some leakage of the probe power. With this in mind, we can understand the appearance of a second peak for 10-ps or wider pulses. Since the index and phase changes produced by the XPM and free carriers occur with opposite signs, they cancel each other occasionally. The case of very long pulses ($T_0 > 100$ ps) is interesting because the switching window can be considerably shorter than the pump pulse but only at the expense of a much reduced power (note the magnification by a factor of 40 in Fig. 8.2 used for this

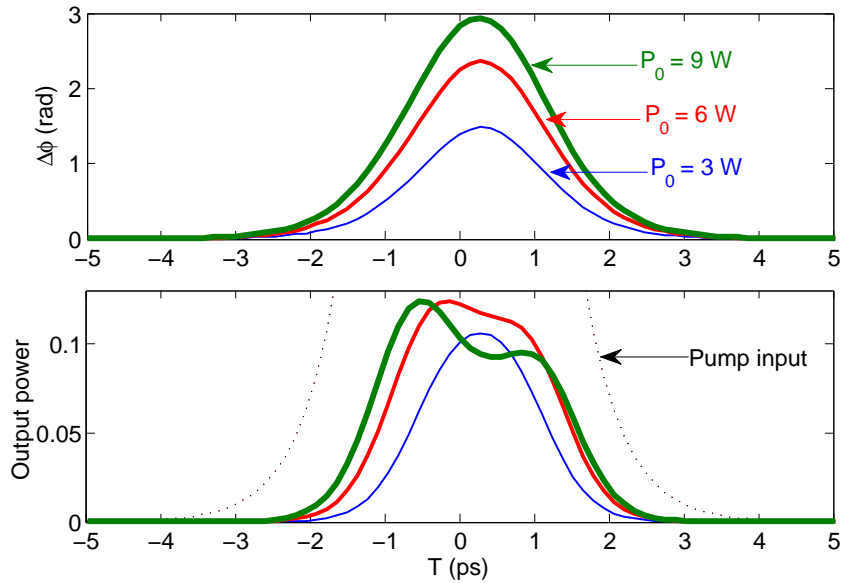


Figure 8.4: Nonlinear phase shift and switching windows at three different input peak powers of 3 W, 6 W, and 9 W in the case of using a square-shape waveguide ($400 \times 400 \text{ nm}^2$). The width of the pump pulses is 1 ps.

case).

We note from Fig. 8.2 that the performance of a silicon-based Kerr shutter suffers considerably (compared with the case of silica fibers) from a combination of the free-carrier and walk-off effects. The use of a square-shape waveguide may help because it will reduce the birefringence effects. Figure 8.3 shows the results under conditions identical to those of Fig. 8.2 except that a square-shape waveguide ($400 \times 400 \text{ nm}^2$) is employed with the modified values $d_x = -1.98 \text{ ps/cm}$, $d_y = -1.16 \text{ ps/cm}$, and $a_{\text{eff}} = 0.09 \text{ } \mu\text{m}^2$. As expected, the switch performance is improved considerably because of reduced walk-off effects. In particular the long tail seen in Fig. 8.2 for 1-ps pump pulses has disappeared completely.

We should point out that the performance of a Kerr switch also depends on the peak power of pump pulses. In the case of a Kerr shutter based on silica, one may want to choose the power level such that $\Delta\phi \approx \pi$. However in the case of silicon waveguides, nonlinear absorptions set the limit on peak pump power. Serious distortion on switching

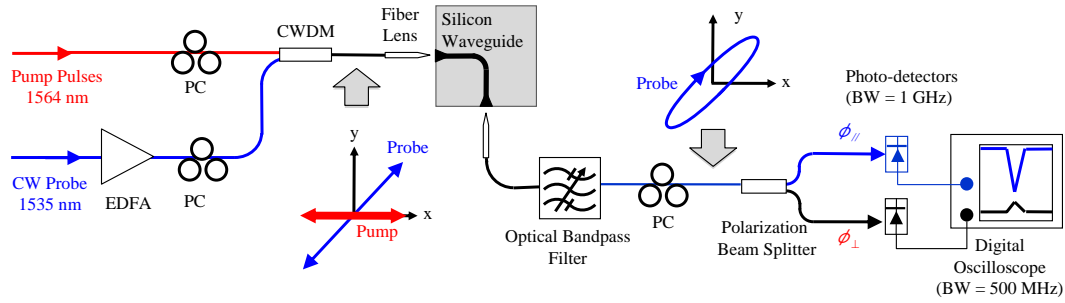


Figure 8.5: Experimental setup used for realizing Kerr switching in silicon waveguides. EDFA: Er-doped fiber amplifier; PC: polarization controller; CWDM: coarse wavelength-division multiplexer.

window starts even before $\Delta\phi$ approaches π . This is illustrated by Fig. 8.4, where the switching window together with the nonlinear phase shift at three different input peak powers ($T_0 = 1$ ps) are drawn in the case of using a square waveguide.

8.4 Experimental Realization of a Silicon Kerr Shutter

We have done several experiments to verify the feasibility of realizing an optical Kerr shutter using an SOI waveguide. The experiments are successful in the sense that they show stable modulation of the CW signal by using pump pulses with only a few watts of peak power. The width of the switching window, resolved by using an optical auto-correlator, is within sub-picosecond regime.

The experimental setup is shown in Fig. 8.5. The optical source for CW signal is a tunable semiconductor laser (HP 8168F). Its output power of 1 mW is then amplified to 300 mW by an EDFA. A polarization controller is placed after the EDFA to make sure that the CW signal is polarized at 45° to the x axis. The pump is a commercial mode-locked fiber laser (PolarOnyx Mercury 1000) that is also amplified by an EDFA to an average power level of 5.9 mW (driving current of EDFA is 80 mA.) that corresponds to a peak power of around 607 W according to Table. 6.1. A polarization controller

is placed after this EDFA as well. Theoretically, this polarization controller should be tuned so that the pump is coupled into the waveguide as the TE mode. However, in our experiment we tuned this polarization controller to optimize the signal-noise ratio of the modulated CW signal at the output.

The CW signal and the pulsed pump are combined using a coarse-WDM (CWDM) coupler. The coupling efficiency for each channel is around 81% which corresponds to an insertion loss of 0.9 dB. The light is then coupled into a 4-mm-long SOI waveguide using a tapered fiber lens with a coupling efficiency of 1%. So the input average power of the CW signal is 2.4 mW and the peak power of the pump pulses is 4.92 W. The light at the output end of the waveguide is then collected using another tapered fiber lens. A tunable optical bandpass filter (3 dB bandwidth is 1.2 nm.) is used to block the pump light. A quarter waveplate is then tuned carefully to compensate for linear phase shift induced by the birefringence of the SOI waveguide. A polarizer is placed after the waveplate. At one orientation of the polarizer (we call it polarizer at ϕ_{\perp}), the tuning of the quarter waveplate and the polarizer is such that the output power of the CW signal (as the current signal in the digital phosphor oscilloscope) alone is at its minimum; then we rotate the polarizer by 90° (we call it polarizer at ϕ_{\parallel}), the output power of the CW signal alone is at its maximum. Then we turn off the CW signal and turn on the pump. We make sure that the pump pulses are completely blocked by the optical bandpass filter since we do not see any residual pulses on the oscilloscope when the pump alone is turned on. While the pump is on, we turn on the CW signal, and we see modulations on the CW signal with either one of the two orientations of the polarizer. If the polarizer is set at ϕ_{\perp} , we see pulses from a lower-level background on the oscilloscope. The modulation depth decreases if the quarter waveplate is tuned away from its optimized orientation and the polarizer is tuned accordingly. This is the demonstration of successful all-optical modulation because of XPM-induced NPR. If the polarizer is set at ϕ_{\parallel} , we then see individual dips from a higher-level background on the oscilloscope with a modulation depth deeper than that in the first scenario. This

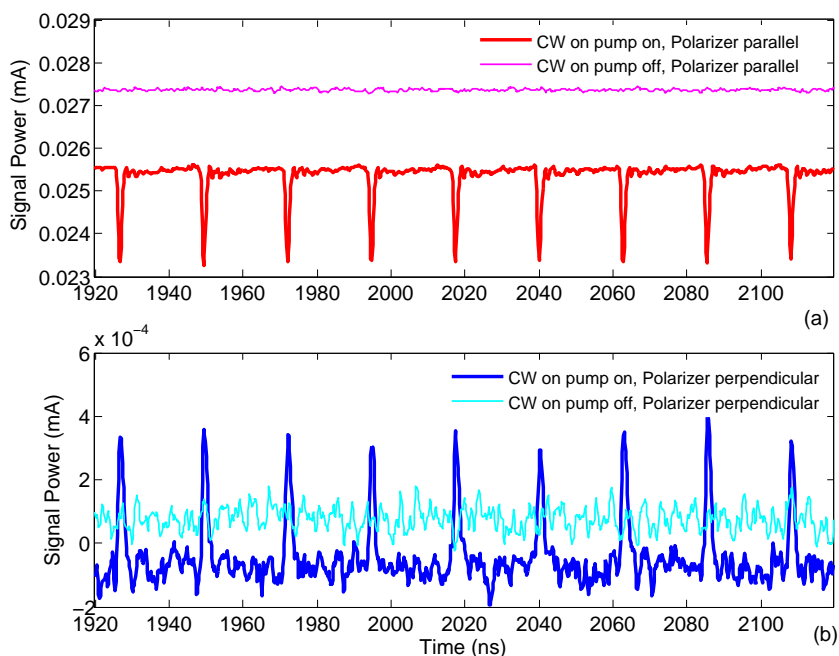


Figure 8.6: Result of the experiment of a silicon Kerr shutter. The data show the readings of the output power of the CW signal in the oscilloscope in four different situations.

is the demonstration of cross-TPA-induced modulation on the CW signal which means one photon from the signal and one photon from the pump are absorbed simultaneously. Also the peak power of the pump pulses is important to achieve good modulation depth. We start to see some modulation when the input peak power reaches 3.8 W (driving current of EDFA is 60 mA). The modulation depth increases as the power increases, becomes maximum when the peak power is 4.9 W (driving current of EDFA is 80 mA), then decreases afterwards, and completely disappears when the input peak power is 12 W (driving current of EDFA is 200 mA). The phenomenon agrees qualitatively with the theoretical prediction as shown in Fig. 8.4. The experimental results with input peak power of 4.9 W are shown in Fig. 8.6.

From these results, we see that each time the pump power is turned on, the average power of the CW signal drops. This comes from the free-carrier dispersion induced phase change on the CW signal because of the free carriers generated through the TPA

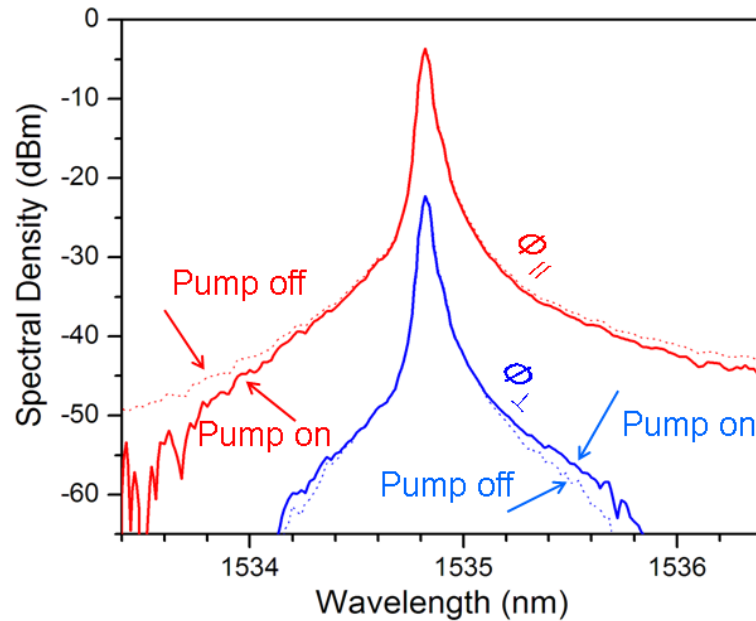


Figure 8.7: Result of the experiment of a silicon Kerr shutter. The data show the readings in the OSA in four different situations.

processes by the pump pulses. The polarizer is adjusted to minimize the background power level of the ϕ_{\perp} state when both pump and probe are on. Because the output is extremely sensitive to the phase change of the CW signal, the background outputs when pump is on are different from that when the pump is off because the phases are different in the two cases. The instantaneous free-carrier effects do not affect much the CW signal as the pump pulses are extremely short (~ 500 fs at the input of the waveguide) compared with the carrier lifetime (~ 2 ns). In the case of polarizer at ϕ_{\parallel} , we see dips on the CW signal whenever there is a pump pulse. This dip is mainly caused by cross-TPA, but at the end of the dips we see a tiny prolonged tail that is because of FCA. This effect is more obvious when a much higher pump power is used. We can use this tail to estimate the free-carrier's lifetime of the SOI waveguide. However, the resolution is limited by the speed of the oscilloscope.

We also measured the spectrum at the output of the polarizer. The results are shown in Fig. 8.7. We do not see an obvious spectral broadening effect because of the relatively

low repetition rate of the pump pulses.

8.5 Experiments with Optimized SOI waveguides

The previous experiments are all carried out on SOI waveguides that have normal taperings on both sides of the waveguides. The cross section of the taperings is $2 \times 0.4 \mu\text{m}^2$. The biggest difficulty of these waveguides is the very low coupling efficiency (around 20 dB coupling loss). In order to improve the quality of the Kerr switch, we optimized the fabrication of the waveguides by using polymer mode-field converters on both sides of the waveguides as discussed in the section of Scattered Light Measurement in Chapter 2. The cross section of the mode-field converters is $2 \times 2 \mu\text{m}^2$. This improves the coupling efficiency significantly. The total coupling loss is around 8 dB in this case. The propagation loss is around 10 dB/cm, and the length of the waveguides are 5 mm long. This improves the signal-to-noise ratio (SNR) of the output signal significantly. And we switch to use the Tapered Lensed Fiber from OZ Optics which provides 12 μm working distance, instead of only around 5 μm with the tapered fiber lenses from Nanonics Imaging Ltd. [48].

The polarizer is adjusted to minimize the background power level of the ϕ_{\perp} state when both pump and probe are on.

In order to see the switching behavior in more detail, we use a 20-GHz optical sampling oscilloscope (OSO) (HP/Agilent 83480A) to measure switched signal outputs at two polarization states. The results are shown in Fig. 8.8. The long tail in the state of ϕ_{\parallel} is caused by FCA, and the free-carrier life time can be estimated to be 2.4 ns from the experimental trace.

We are interested in the switching behavior at different pump peak power levels. Fig. 8.9 (a) shows the switched amplitude as a function of pump peak power in the silicon waveguide. The switched amplitude is normalized to the transmitted background power of the probe at ϕ_{\parallel} . The blue squares indicate the measured switching amplitude

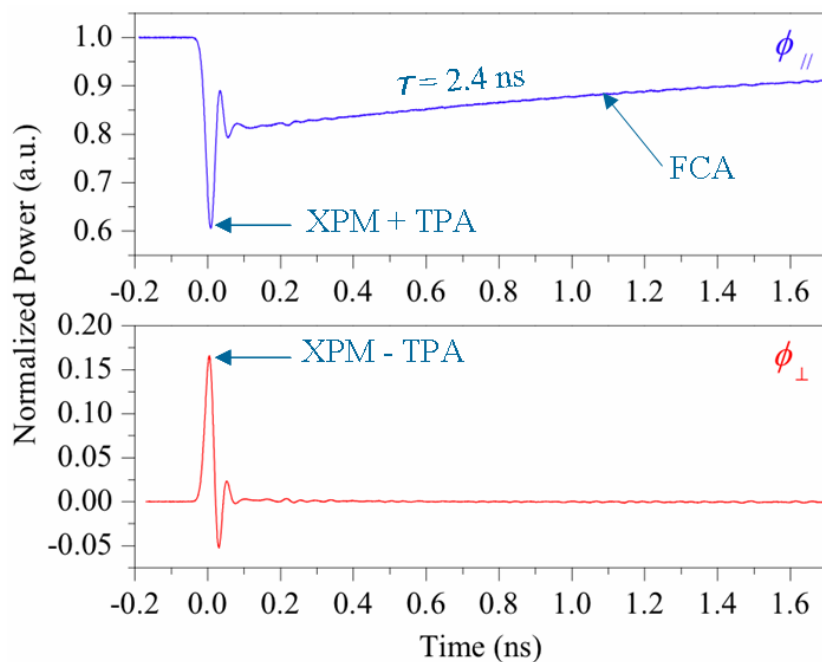


Figure 8.8: Result of the experiment of a silicon Kerr shutter. Measured oscilloscope traces of the probe output at ϕ_{\parallel} and ϕ_{\perp} using a 20-GHz optical sampling oscilloscope.

of the dip for ϕ_{\parallel} . As the pump peak power increases, the probe is switched with larger amplitude. This is consistent with the proportion of TPA to the pump power. In the case of ϕ_{\perp} (red dots), the switching amplitude is maximum at pump peak power of about 13 W. In general, there is an optimized pump peak power for highest switching amplitude. We also recorded the residual pump pulse when the CW probe is turned off. The residual pump pulse is negligibly small compared with the switched probe power. Numerical simulations confirm the switching behavior at lower input powers as shown in Fig. 8.9 (b). A gaussian shaped low-pass filter is used to mimic the limited bandwidth of the OSO for the numerical simulation. However we do have some difficulty in matching the numerical simulations with the experiment results at high input peak powers. Further study of nonlinear effects at high input peak powers inside SOI waveguides is needed for better understanding.

We use an optical autocorrelator (model FR-103MN by Femtochrome Research)

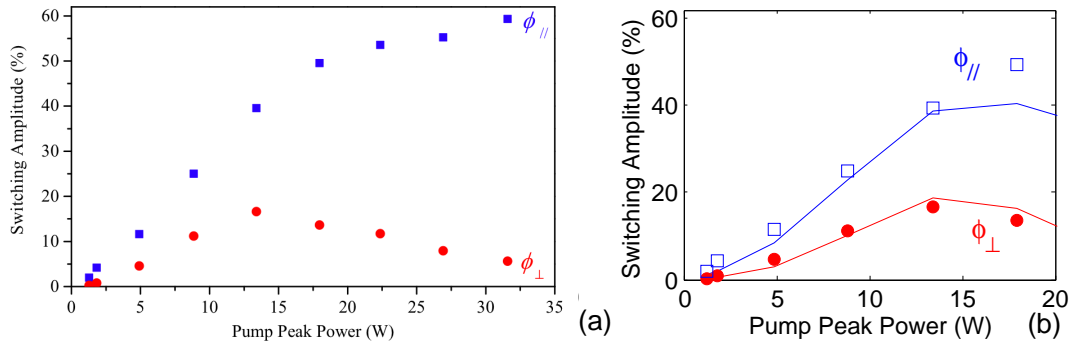


Figure 8.9: Switching amplitude as a function of input pump peak power at ϕ_{\parallel} and ϕ_{\perp} using a 20-GHz optical sampling oscilloscope: (a) Experiment results; (b) Numerical simulations at low input pump peak power.

to resolve the width of the switching window. As the power of the probe output is too weak to generate a second harmonic signal for second order autocorrelation, we amplify the output of the signal using an EDFA (up to 16 dBm average power). Fig. 8.10 (a) shows the autocorrelation traces at different input pump peak power. The trace at the pump peak power of 3.3 W shows a FWHM of 1.1 ps. This corresponds to a pulse width of about 800 fs for a gaussian pulse. Note that the signal pulse is broadened inside the EDFA also. At the pump peak power of 4.9 W, we start to see two wings on each side of the center switching window. This is due to walk-off effects. And the walk-off induced wings dominate at even higher pump peak power levels. The behavior of walk-off induced wings is confirmed by the numerical simulation as shown in Fig. 8.10 (b). The FWHM of the autocorrelation trace at the pump peak power of 13 W is found to be 7.6 ps. This number is used to decide the walk-off parameter d_y for the numerical simulations. This number is found to be about 30% of that from FDFD calculations. This shows that the actual dimensions of the waveguide deviate from the designed values by a small amount.

Another thing to notice is that FCD parameter $\zeta \approx -5.3 \times 10^{-27} \text{ m}^3$ instead of $\zeta \approx -1.35 \times 10^{-27} \text{ m}^3$ is used for better agreement of numerical simulation with experimental results. This confirms that the hole contribution to FCD is 5 times that of

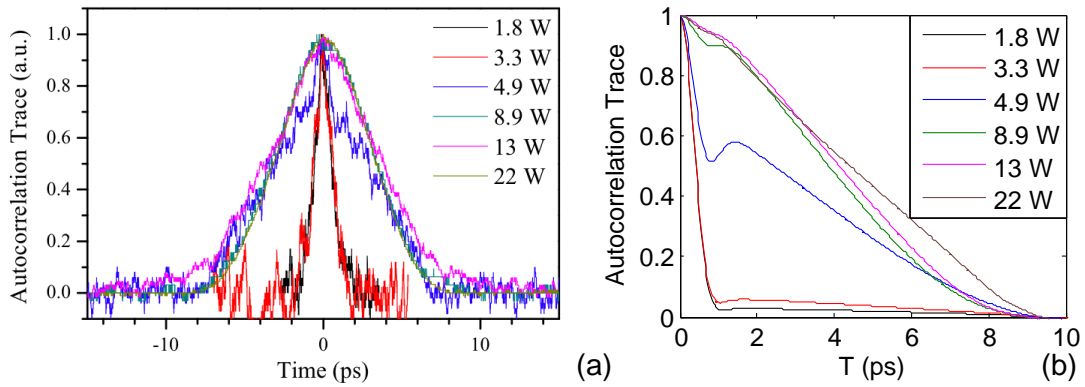


Figure 8.10: Autocorrelation traces of the probe output at ϕ_{\perp} : (a) Experiment results; (b) Numerical simulations.

electrons [9].

8.6 Summary

In summary, first we have shown theoretically that the NPR, induced by a pump pulse on a CW probe inside a silicon waveguide, can be used to realize a fast Kerr shutter. We show that free carriers generated by the pump pulse through two-photon absorption affect the switching process because of a combination of the free-carrier and walk-off effects. However, their impact is not detrimental for pump pulses shorter than 5 ps or so, especially when birefringence effects are minimized by employing a square-shape waveguide. For such short pulses, an approximate analytical solution predicts the shape and duration of the switching window with reasonable accuracy. Even though a switching window of < 5 ps duration can be realized using SOI waveguides, we stress that the repetition rate of such a switch is invariably limited by the carrier lifetime. It is unlikely to exceed 1 GHz unless the effective carrier lifetime is reduced substantially using a suitable technique such as carrier sweeping by an external electric field [29] or enhanced recombination through ion implantation [88]. Also the performance can be improved by optimizing the waveguide geometry to minimize the walk-off effect.

Second, we have realized a Kerr shutter experimentally using an SOI waveguide. We see that the CW signal can be switched at the same rate as the pump pulses. In the case of polarizer at perpendicular state we see modulated pulses, while in the case of polarizer at parallel state we see dips modulated by cross-TPA at the presence of the pump pulses. Optical autocorrelation traces of the switching window are recorded. Ultra short switching window (< 1 ps) is realized experimentally.

9 Mode-locked Fiber Laser and Pulse Width Measuring

In this chapter, we discuss two mode-locked fiber lasers that we used to do the experiments on SOI waveguides. We explain the working scheme of our home-made mode-locked fiber laser first, and then we characterize the parameters of the home-made mode-locked fiber laser and the commercial mode-locked fiber laser. We use optical auto-correlators to measure the pulse width. One of the auto-correlators is based on two-photon absorption inside a silicon APD, and the other one is based on second-harmonic generation inside a nonlinear crystal (LiIO_3). The commercial laser is amplified by an EDFA. The measurements show that pulse width increases as the EDFA's driving current increases.

9.1 Home-Built Mode-locked Fiber Laser

We built a passively mode-locked all-fiber erbium laser for experiments on SOI waveguides. The setup is schematically shown in Fig. 9.1. The mode-locking scheme is nonlinear polarization rotation. The idea is that the pulse acquires intensity-dependent nonlinear phase shift as it propagates inside the ring cavity. The polarization of the pulse rotates as a consequence of this nonlinear phase shift. However, the center of the pulse acquires a different polarization than its wings. In the setup, the isolator has

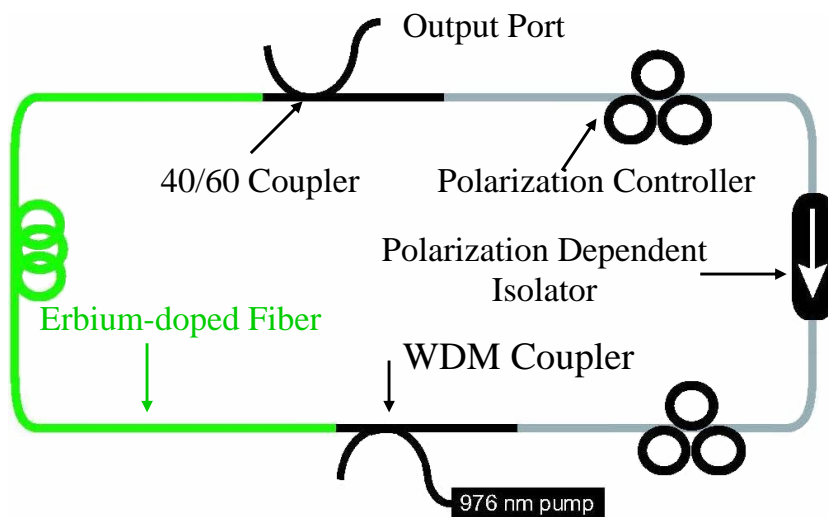


Figure 9.1: Setup of a mode-locked all-fiber erbium laser. The mode-locking scheme is nonlinear polarization rotation.

a large polarization-dependent loss. The two polarization controllers allow us to optimize the state of polarization such that the peak of the pulse travels through the isolator. Therefore, the isolator shortens the pulse by acting, in conjunction with the nonlinear polarization rotation mechanism, as an artificial fast saturable absorber [89]. It is possible to use a single polarization controller. However, two polarization controllers give more freedom to do adjustment. We found it easier to use both of them.

The total length of the ring cavity is around 12 m, while the length of the erbium-doped fiber is around 4 m. We are able to mode lock the laser at two different wavelengths as shown in Fig. 9.2, one wavelength is at 1532 nm, which is near the peak of erbium gain spectrum, the other is at 1561 nm, a wavelength near which losses of our fiber ring cavity are minimum. The 3-dB spectral bandwidths of the mode-locked pulses at these two wavelengths are 5.6 nm and 5.2 nm, respectively. The pulse-train observed using an oscilloscope is shown in Fig. 9.3. The period of pulses is around 119 ns. A 40/60 output coupler is used to maximize the output power of the laser. In our setup, the 980-nm pump power can be as high as 120 mW. The maximum average power of the mode-locked fiber laser is around 5 mW. The 3-dB pulse width is mea-

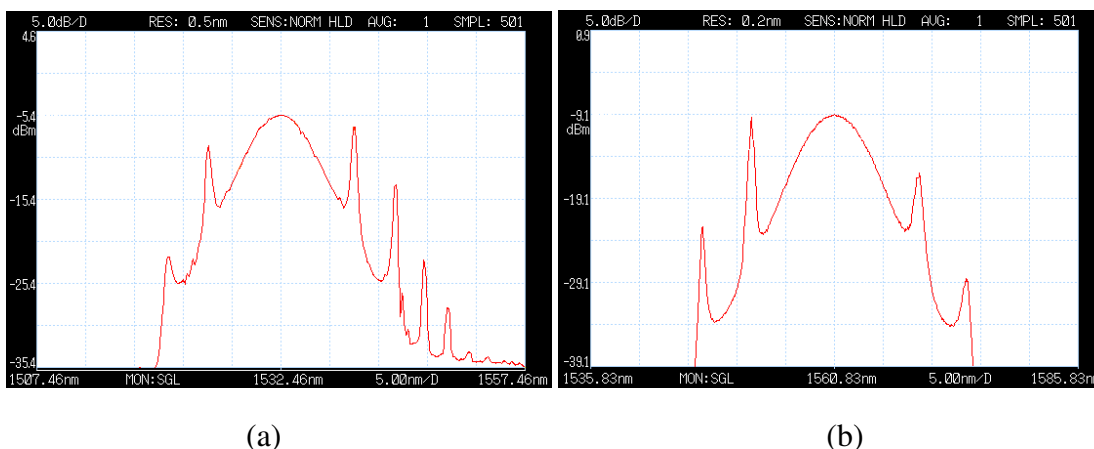


Figure 9.2: Spectra of the home-made mode-locked all-fiber erbium laser: (a) mode-locked at 1532 nm; (b) mode-locked at 1561 nm.

sured to be around 900 fs by using an optical auto-correlator which will be discussed later.

An interesting thing we found about the polarization of such a mode-locked fiber laser is that the polarization is wavelength-dependent. Fig. 9.4 is a demonstration of such phenomenon. We let the output of the mode-locked fiber laser first pass through a polarization controller, then pass through a polarizer which passes horizontally polarized light, then feed into an optical spectrum analyzer (OSA). The polarization controller is adjusted such that the center of the spectrum becomes a minimum after passing through the polarizer. So the polarization controller converts the polarization state of the original peak of the spectrum into linear polarization along the vertical axis. From Fig. 9.4 we know that the polarization states at different wavelengths are different. This is easily understood because the mode-locking scheme of this laser is through nonlinear polarization rotation which implies that the state of polarization is power dependent in the frequency-domain. Since the output coupler is placed at a location that is away from the isolator, the polarization state of the laser output of a single pulse will also be varying in the time-domain.

Besides the home-made mode-locked fiber laser, we also use a commercial laser Po-

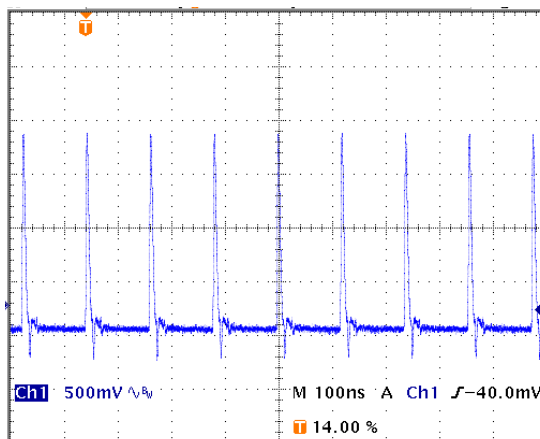


Figure 9.3: Figure of pulse-train from oscilloscope. The period of pulses is 119 ns.

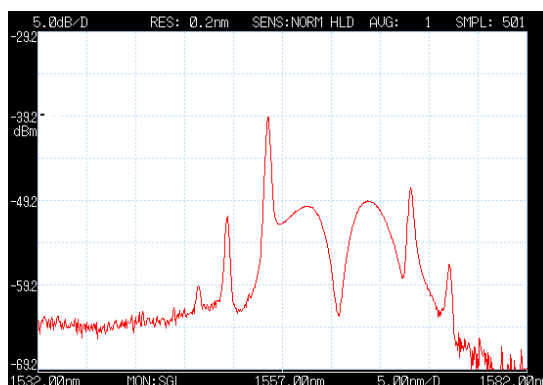


Figure 9.4: Wavelength-dependence of the polarization state of the mode-locked all-fiber laser.

larOnyx Mercury 1000 (<http://www.polaronyx.com/>). The output power of the mode-locked fiber laser itself is not very strong. However there is a very powerful EDFA after the laser that can boost the average output power up to 120 mW. The 3-dB pulse width is around 200 fs, pulse period is 23 ns. The center wavelength is 1562 nm and the 3-dB bandwidth of spectrum is 12.6 nm. There is a dispersive wave located at 1574 nm as shown in Fig. 9.5.

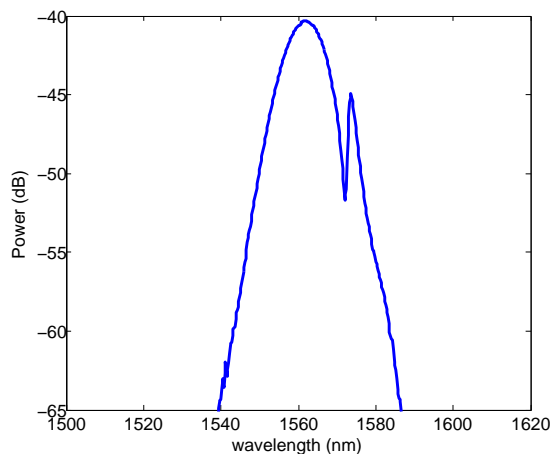


Figure 9.5: Spectrum of the commercial mode-locked fiber laser (Mercury 1000 by PolarOnyx).

9.2 Pulse-Width Measured using Auto-Correlation

Different techniques are needed to measure pulse shapes at different time scales. Very fast oscilloscopes combined with fast detectors are able to measure pulses as short as 14 ps. For example, the Digital Serial Analyzer Sampling Oscilloscope DSA8200 by Tektronix provides the bandwidth up to 70+ GHz (<http://www.tek.com/>), and the Terabit Optical Oscilloscope C8660 by Hamamatsu also provides bandwidth measurement of more than 70 GHz (<http://www.hamamatsu.com/>). Streak cameras are another convenient tool to measure short pulses typically with a temporal resolution of 2 picoseconds. Measurements of pulses shorter than this duration require other techniques such as optical autocorrelation and frequency-resolved optical gating (FROG) [90].

We use optical autocorrelation to gain information about the pulse shape. We tried two different ways to use intensity optical autocorrelation to measure the pulse width of mode-locked fiber lasers.

9.2.1 Interferometric Auto-Correlation using TPA inside Si APD

Since the temporal phase can be a problem in using the amplitude auto-correlation, it is more accurate to use the intensity auto-correlation where the phase term does not appear in the intensity. A very simple way to carry out intensity auto-correlation is to focus the output of the Michelson interferometer into a silicon APD. Since silicon does not absorb light at 1.55 μm linearly, but absorbs the light nonlinearly through two-photon absorption, we can use this effect to setup an intensity auto-correlation. The difficulty of this technique is that some residue pump light at 980 nm will be absorbed linearly by the silicon APD. By using backward pumping in the laser cavity, we can eliminate the residual 980-nm light substantially. Then we use a 1550/980 WDM coupler to further cut down the residual 980-nm light.

Assuming that the pulses are Gaussian:

$$E_1(t) = I_1 \exp(-t^2/T_0^2 - i\omega t), \quad E_2(t) = I_2 \exp[-(t + \tau)^2/T_0^2 - i\omega(t + \tau)]. \quad (9.1)$$

We separate the linear and nonlinear response of the detector as [92]:

$$r_L \propto \int_{-\infty}^{\infty} |E_1(t) + E_2(t)|^2 dt, \quad (9.2)$$

$$r_{NL} \propto \int_{-\infty}^{\infty} |E_1(t) + E_2(t)|^4 dt, \quad (9.3)$$

where we have neglected the spatial distribution of the laser spot. Plugging Eq. (9.1) into the linear and nonlinear response functions, and assuming $I_1 = I_2$, we get

$$r_L \propto \int_{-\infty}^{\infty} \left[\exp(-\frac{t^2}{T_0^2}) + \exp(-\frac{(t + \tau)^2}{T_0^2}) + 2 \exp[-\frac{(t + \tau/2)^2 + \tau^2/4}{T_0^2}] \cos(\omega\tau) \right] dt, \quad (9.4)$$

$$r_{NL} \propto \int_{-\infty}^{\infty} \left[\exp(-\frac{t^2}{T_0^2}) + \exp(-\frac{(t + \tau)^2}{T_0^2}) + 2 \exp[-\frac{(t + \tau/2)^2 + \tau^2/4}{T_0^2}] \cos(\omega\tau) \right]^2 dt. \quad (9.5)$$

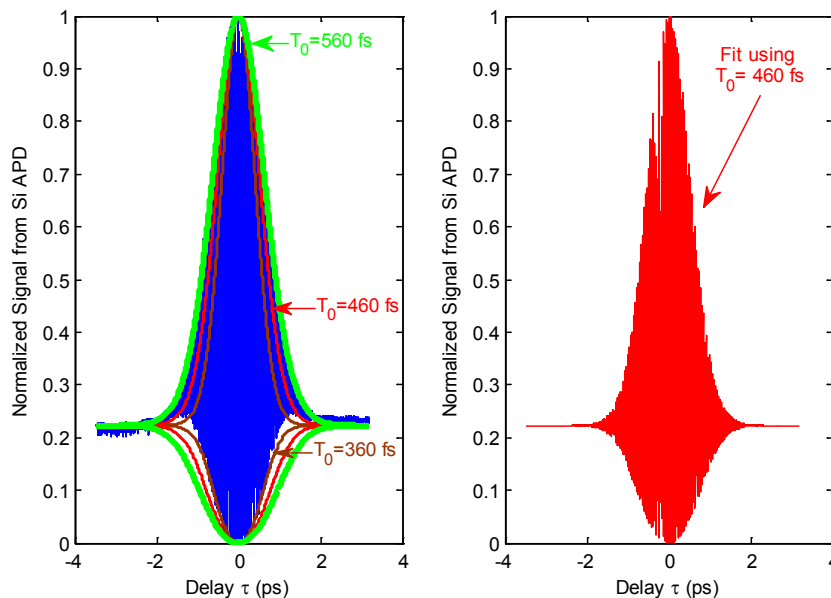


Figure 9.6: TPA-based auto-correlation trace and its fit using Gaussian pulse shape: (a) Experiment data with a fitting envelope using Gaussian pulse shape with $T_0 = 560$ fs, 460 fs, and 360 fs; (b) Numerically simulated data with $T_0 = 460$ fs

The linear and nonlinear responses are thus given by

$$r_L \propto 2\sqrt{\pi}T_0 \left[1 + \exp\left(-\frac{\tau^2}{4T_0^2}\right) \cos(\omega\tau) \right], \quad (9.6)$$

$$r_{NL} \propto \sqrt{2\pi}T_0 \left[1 + \exp\left(-\frac{\tau^2}{2T_0^2}\right) + 4\exp\left(-\frac{3\tau^2}{8T_0^2}\right) \cos(\omega\tau) + 2\exp\left(-\frac{\tau^2}{2T_0^2}\right) \cos^2(\omega\tau) \right]. \quad (9.7)$$

In the experiment, we use New Focus Optically Encoded Translation Stages 9067-com-E (step resolution is 80 nm) to control the movable mirror with the step size of 240 nm. The auto-correlation trace obtained with the home-made mode-locked fiber laser is shown in Fig. 9.6(a). We then fit the experimental data using Eqs. (9.6) and (9.7). The value $T_0 = 560$ fs is good for the top envelope, while the value $T_0 = 360$ fs is good for the bottom envelope, hence we use $T_0 = 460$ fs as a compromise. Hence the FWHM of the pulse is again 770 fs which agrees with the result of the previous section. Note that the ratio 8:1 (peak to the wings), characteristic of interferometric autocorrelation traces,

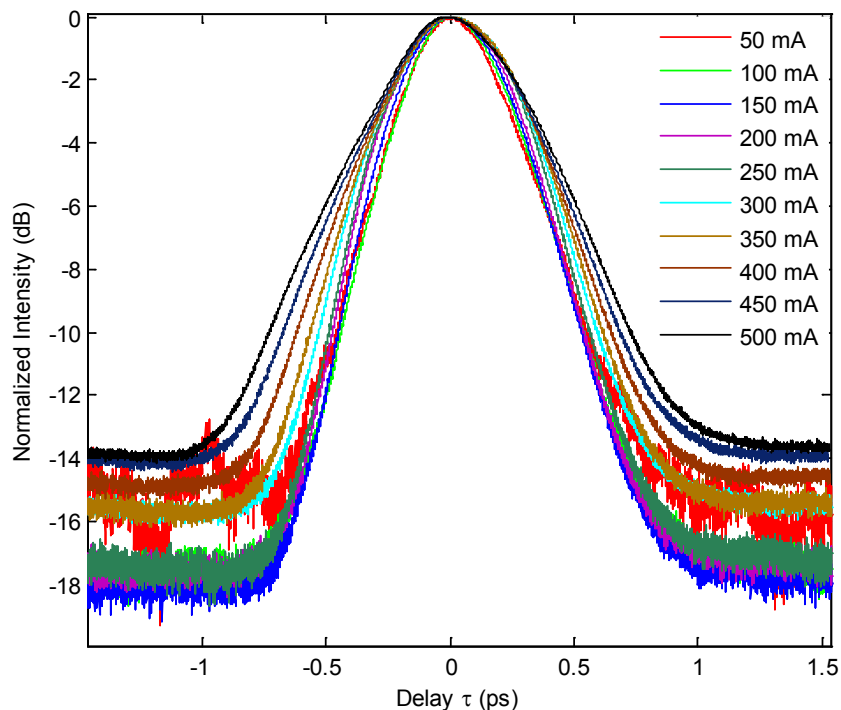


Figure 9.7: SHG-based auto-correlation trace. The curves represent pulses after the EDFA with pumping current changing from 50 mA to 500 mA.

does not show up in the figure. This is because the linear response also takes part in the detector's whole response function. In the case of second harmonic generation (SHG), if a filter is used to completely block the fundamental wavelength component, then the linear term disappears and we should be able to see the ratio of 8:1. Another issue we need to emphasize is that the amplitude of the output pulse of a mode-locked fiber laser is better fitted with a hyperbolic secant function [91]. It is also possible to do the calculations using hyperbolic secant function [92]. However we only used a Gaussian function for calculational simplicity.

9.2.2 Intensity Auto-Correlation using SHG

The third way we measure the pulse width is using a commercial optical auto-correlator FR-103MN by Femtochrome Research, Inc. The basic idea is to use the second har-

Pumping Current (mA)	50	100	150	200	250	300	350	400	450	500
$\text{FWHM}_{\text{trace}}(\text{fs})$	458	464	504	544	570	588	594	601	615	639
$\text{FWHM}_{\text{pulse}}(\text{fs})$	234	236	257	278	291	300	303	306	314	326

Table 9.1: The correspondence between the driving current of the EDFA and the estimated FWHM of the pulses.

monic generation (SHG) in a nonlinear crystal to realize intensity auto-correlation. In our experiment, we use LiIO_3 as the nonlinear crystal. The working wavelength range of the crystal is 700 – 1800 nm. The SHG pulses are then fed into a PMT detector while the original two beams of light are blocked. The electric signal is then displaced using an oscilloscope for recording. Since this is a commercial auto-correlator, the detailed information can be found on their website (<http://www.femtochrome.com/>).

The equations that describe the response of the PMT are the same as those in the case of the Si APD. Since an oscilloscope is a slow electronic device, the fast oscillation feature is absent for the signals we get using this auto-correlator. The nice part of this device is that the speed is much faster than the previous one because scanning of the delay is done by spinning the mirrors instead of moving the movable mirror step by step. We use this device to study the pulse width changes of the PolarOnyx Mercury 1000 laser after being amplified by the powerful EDFA. The results are shown in Fig. 9.7. As a good estimate from the previous section, the FWHM of the pulse is about 0.51 times the FWHM of the auto-correlation trace. Hence the FWHM of the pulses can be calculated. The results in Table 9.1 show that the pulse width increases with increasing pumping current of the EDFA. The noise level of the auto-correlation trace also increases. This implies that the pulses are more and more chirped by SPM.

9.3 Summary

In summary, we have built a mode-locked all-fiber laser that is based on nonlinear polarization rotation of the pulses traveling inside the ring cavity. We used two different techniques to measure the width of the mode-locked pulses. Our study shows that the pulses becomes broader after propagation through an EDFA, and the EDFA puts on chirps onto the pulses.

10 Summary

In this thesis on the third and higher-order nonlinear optics in silicon waveguides, we have investigated both the linear and nonlinear optical properties of silicon-on-insulator (SOI) waveguides with an emphasis on third-order nonlinearities and free-carrier effects in such waveguides. The objective is to understand the possible nonlinear applications of SOI waveguides and to analyze the intrinsic difficulties this structure faces for some of the real applications.

Chapter 1 gives a short introduction of the current state of research in silicon photonics. Chapter 2 discusses the SOI waveguides we used in our laboratory, and the measurements of propagation loss, total insertion loss, and coupling loss using Fabry-Perot resonances, cutback method, and scattered light measurement method. Chapter 3 discusses three mathematical tools for calculating the modes and dispersion properties of SOI waveguides, and compares the three methods from the aspects of accuracy and efficiency. Chapter 4 discusses the importance of anomalous dispersion properties in SOI waveguides, dispersion tailor-ing of SOI waveguides in order to realize anomalous dispersion at a wavelength around $1.5 \mu\text{m}$, and the possibility of soliton propagation in such a tailored waveguide. Chapter 5 provides a theoretical model for light propagation inside an SOI waveguide. The general formalism includes both the electronic and Raman responses of nonlinear light-material interaction. Chapter 6 considers the self-phase modulation process in SOI waveguides, with the emphasis on the role of

two-photon absorption and the consequent free-carrier effects. The maximum allowed repetition rate of pulse trains is presented to serve as a general guideline for using the self-phase modulation effect in real situations. This chapter also presents our experimental work on self-phase modulation showing significant spectral broadening and continuous spectral blue shift of pulses propagating through an SOI wave-guide. Chapter 7 describes supercontinuum generation in SOI waveguides with some preliminary experimental results. Chapter 8 considers cross-phase modulation and nonlinear polarization rotation for realizing an SOI waveguide based optical Kerr shutter. The theoretical work is given first. Our experiment results are given after the theory. They show that the experiment of all-optical switching based on nonlinear polarization rotation is successful, and sub-pico-second switching window is realizable using this technique. The required input peak power of the pump pulses can be as low as a couple of watts. Finally, Chapter 9 deals with the laser sources we used in our experiments on SOI waveguides. It first discusses a home-made mode-locked fiber laser and a commercial high-power mode-locked fiber laser, and then presents the measurements of the pulse widths.

Bibliography

- [1] L. Pavesi and D. J. Lockwood, Eds., *Silicon Photonics* (Springer, New York, 2004).
- [2] G. T. Reed and A. P. Knights, *Silicon Photonics: An Introduction* (Wiley, Hoboken, NJ, 2004).
- [3] M. Lipson, “Guiding, modulating, and emitting light on silicon—challenges and opportunities,” *J. Lightwave Technol.* **23**, 4222–4238 (2005).
- [4] T. Tsuchizawa, K. Yamada, H. Fukuda, T. Watanabe, J. Takahashi, M. Takahashi, T. Shoji, E. Tamechika, E. Itabashi, and H. Morita, “Microphotonic devices based on silicon microfabrication technology,” *IEEE J. Sel. Top. Quantum Electron.* **11**, 232–240 (2005).
- [5] R. A. Soref, “The Past, Present, and Future of Silicon Photonics,” *IEEE J. Sel. Top. Quantum Electron.* **12**, 1678–1687 (2006).
- [6] B. Jalali and S. Fathpour, “Silicon Photonics,” *J. Lightwave Technol.* **24**, 4600–4615 (2006).
- [7] A. Barkai, Y. Chetrit, O. Cohen, R. Cohen, N. Elek, E. Ginsburg, S. Litski, A. Michaeli, O. Raday, D. Rubin, G. Sarid, N. Izhaky, M. Morse, O. Dosunmu, A. Liu, L. Liao, H. Rong, Y. Kuo, S. Xu, D. Alduino, J. Tseng, H. Liu, and M. Paniccia, “Integrated silicon photonics for optical networks,” *J. Optical Networking* **6**, 25–47 (2007).

- [8] T. Barwicz, H. Byun, F. Gan, C. W. Holzwarth, M. A. Popović, P. T. Rakich, M. R. Watts, E. P. Ippen, F. X. Kärtner, H. I. Smith, J. S. Orcutt, R. J. Ram, V. Stojanovic, O. O. Olubuyide, J. L. Hoyt, S. Spector, M. Geis, M. Grein, T. Lyszczarz, and J. U. Yoon, "Silicon photonics for compact, energy-efficient interconnects," *J. Optical Networking* **6**, 63–73 (2007).
- [9] Q. Lin, O. J. Painter, and G. P. Agrawal, "Nonlinear optical phenomena in silicon waveguides: Modeling and applications," *Opt. Express* **15**, 16604–16644 (2007).
- [10] P. A. Anderson, B. S. Schmidt, and M. Lipson, "High confinement in silicon slot waveguides with sharp bends," *Opt. Express* **14**, 9197–9202 (2006).
- [11] T. Fujisawa and M. Koshiba, "Guided modes of nonlinear slot waveguides," *IEEE Photon. Technol. Lett.* **18**, 1530–1532 (2006).
- [12] Y. Fu, H. G. Yoo, D. B. Riley, and P. M. Fauchet, "Photon confinement in multi-slot waveguides," in *Conference on Lasers and Electro-Optics/Quantum Electronics and Laser Science Conference and Photonic Applications Systems Technologies 2008 Technical Digest* (Optical Society of America, Washington, DC, 2008), paper CThT4.
- [13] M. R. Lee, B. L. Miller, and P. M. Fauchet, "Two-dimensional photonic crystal slot microcavity sensor for virus-sized particle detection," *Integrated Photonics and Nanophotonics Research and Applications 2008*, paper ITuC4.
- [14] A. Liu, L. Liao, D. Rubin, H. Nguyen, B. Ciftcioglu, Y. Chetrit, N. Izhaky, and M. Paniccia, "High-speed optical modulation based on carrier depletion in a silicon waveguide," *Opt. Express* **15**, 660–668 (2007)
- [15] A. Liu, L. Liao, D. Rubin, J. Basak, H. Nguyen, Y. Chetrit, R. Cohen, N. Izhaky, M. Paniccia, "High-speed silicon modulator for future VLSI interconnect," *Integrated Photonics and Nanophotonics Research and Applications 2007*, paper IMD3.

- [16] A. W. Fang, H. Park, O. Cohen, R. Jones, M. J. Paniccia, and J. E. Bowers, “Electrically pumped hybrid AlGaInAs-silicon evanescent laser,” *Opt. Express* **14**, 9203–9210 (2006).
- [17] M. A. Green, J. Zhao, A. Wang, P. J. Reece, and M. Gal, “Efficient silicon light-emitting diodes,” *Nature* **412**, 805–808 (2001).
- [18] B. R. Koch, A. W. Fang, O. Cohen, and J. E. Bowers, “Mode-locked silicon evanescent lasers,” *Opt. Express* **15**, 11225–11233 (2007)
- [19] A. W. Fang, B. R. Koch, K. Gan, H. Park, R. Jones, O. Cohen, M. J. Paniccia, D. J. Blumenthal, and J. E. Bowers, “A racetrack mode-locked silicon evanescent laser,” *Opt. Express* **16**, 1393–1398 (2008)
- [20] T. Yin, R. Cohen, M. M. Morse, G. Sarid, Y. Chetrit, D. Rubin, and M. J. Paniccia, “31 GHz Ge n-i-p waveguide photodetectors on Silicon-on-Insulator substrate,” *Opt. Express* **15**, 13965–13971 (2007)
- [21] H. Tsang, C. Wong, T. Liang, I. Day, S. Roberts, A. Harpin, J. Drake, and M. Asghari, “Optical dispersion, two-photon absorption and self-phase modulation in silicon waveguides at 1.5 μm wavelength,” *Appl. Phys. Lett.* **80**, 416–418 (2002).
- [22] E. Dulkeith, Y. A. Vlasov, X. Chen, N. C. Panoiu, and R. M. Osgood, “Self-phase-modulation in submicron silicon-on-insulator photonic wires,” *Opt. Express* **14**, 5524–5534 (2006)
- [23] O. Boyraz, T. Indukuri, and B. Jalali, “Self-phase-modulation induced spectral broadening in silicon waveguides,” *Opt. Express* **12**, 829–834 (2004).
- [24] N. C. Panoiu, X. Chen, and R. M. Osgood, “Modulation instability in silicon photonic nanowires,” *Opt. Lett.* **31**, 3609–3611 (2006).

- [25] O. Boyraz, P. Koonath, V. Raghunathan, and B. Jalali, "All optical switching and continuum generation in silicon waveguides," *Opt. Express* **12**, 4094–4102 (2004).
- [26] R. Claps, D. Dimitropoulos, V. Raghunathan, Y. Han, and B. Jalali, "Observation of stimulated Raman amplification in silicon waveguides," *Opt. Express* **11**, 1731–1739 (2003).
- [27] H. Rong, A. Liu, R. Nicolaescu, M. Paniccia, O. Cohen, and D. Hak, "Raman gain and nonlinear optical absorption measurements in a low-loss silicon waveguide," *Appl. Phys. Lett.* **85**, 2196–2198 (2004).
- [28] O. Boyraz and B. Jalali, "Demonstration of a silicon Raman laser," *Opt. Express* **12**, 5269–5273 (2004).
- [29] H. Rong, A. Liu, R. Jones, O. Cohen, D. Hak, R. Nicolaescu, A. Fang, and M. Paniccia, "An all-silicon Raman laser," *Nature* **433**, 292–294 (2005).
- [30] H. Rong, A. Liu, R. Jones, O. Cohen, D. Hak, R. Nicolaescu, A. Fang, and M. Paniccia, "A continuous-wave Raman silicon laser," *Nature* **433**, 725–728 (2005).
- [31] H. Rong, S. Xu, O. Cohen, O. Raday, M. Lee, V. Sih, and M. Paniccia, "A cascaded silicon Raman laser," *Nature Photonics* **2**, 170–174 (2008).
- [32] R. Jones, A. Liu, H. Rong, M. Paniccia, O. Cohen, and D. Hak, "Lossless optical modulation in a silicon waveguide using stimulated Raman scattering," *Opt. Express* **13**, 1716–1723 (2005).
- [33] V. Raghunathan, R. Claps, D. Dimitropoulos, and B. Jalali, "Parametric raman wavelength conversion in scaled silicon waveguides," *J. Lightwave Technol.* **23**, 2094–2102 (2005).

- [34] H. Fukuda, K. Yamada, T. Shoji, M. Takahashi, T. Tsuchizawa, T. Watanabe, J. Takahashi, and S. Itabashi, "Four-wave mixing in silicon wire waveguides," *Opt. Express* **13**, 4629–4637 (2005).
- [35] Y. Kuo, H. Rong, V. Sih, S. Xu, and M. Paniccia, "Demonstration of wavelength conversion at 40 Gb/s data rate in silicon waveguides," *Opt. Express* **14**, 11721–11726 (2006).
- [36] M. Foster, A. C. Turner, J. E. Sharping, B. S. Schmidt, M. Lipson, and A. L. Gaeta, "Broad-band optical parametric gain on a silicon photonic chip," *Nature* **441**, 960–963 (2006).
- [37] Q. Lin, J. Zhang, P. M. Fauchet, and G. P. Agrawal, "Ultrabroadband parametric generation and wavelength conversion in silicon waveguides," *Opt. Express* **14**, 4786–4799 (2006).
- [38] Q. Lin and G. P. Agrawal, "Silicon waveguides for creating quantum-correlated photon pairs," *Opt. Lett.* **31**, 3140–3142 (2006).
- [39] J. E. Sharping, K. F. Lee, M. A. Foster, A. C. Turner, B. S. Schmidt, M. Lipson, A. L. Gaeta, and P. Kumar, "Generation of correlated photons in nanoscale silicon waveguides," *Opt. Express* **14**, 12388–12393 (2006).
- [40] Q. Lin, T. J. Johnson, R. Perahia, C. P. Michael, and O. J. Painter, "A proposal for highly tunable optical parametric oscillation in silicon micro-resonators," *Opt. Express* **16**, 10596–10610 (2008).
- [41] D. Marris-Morini, X. L. Rous, L. Vivien, E. Cassan, D. Pascal, M. Halbwax, S. Maine, S. Laval, J. M. Fefeli, and J. F. Damlencourt, "Optical modulation by carrier depletion in a silicon PIN diode," *Opt. Express* **14**, 10838–10843 (2006).
- [42] Q. Xu and M. Lipson, "Carrier-induced optical bistability in silicon ring resonators," *Opt. Lett.* **31**, 341–343 (2006).

- [43] F. C. Ndi, J. Toulouse, T. Hodson, and D. W. Prather, "All-optical switching in silicon photonic crystal waveguides by use of the plasma dispersion effect," *Opt. Lett.* **30**, 341–343 (2005).
- [44] C. Manolatou and M. Lipson, "All-optical silicon modulators based on carrier injection by two-photon absorption," *J. Lightwave Technol.* **24**, 1433–1439 (2006).
- [45] Q. Xu, V. R. Almeida, and M. Lipson, "Micrometer-scale all-optical wavelength converter on silicon," *Opt. Lett.* **30**, 2733–2735 (2005).
- [46] T. Tanabe, M. Notomi, S. Mitugi, A. Shinya, and E. Kuramochi, "Fast bistable all-optical switch and memory on a silicon photonic crystal on-chip," *Opt. Lett.* **30**, 2575–2577 (2005).
- [47] C. A. Barrios and M. Lipson, "Silicon photonic read-only memory," *J. Lightwave Technol.* **24**, 2898–2905 (2006).
- [48] <http://www.nanonics.co.il/lensed-fibers.html>
- [49] J. Singh, *Electronic and Optoelectronic Properties of Semiconductor Structures*, (Cambridge, 2003).
- [50] D. F. Prelewitz and T. G. Brown, "optical limiting and free-carrier dynamics in a periodic semiconductor waveguide," *J. Opt. Soc. Am. B.* **11**, 304–312 (1994).
- [51] S. J. McNab, N. Moll, and Y. A. Vlasov, "Ultra-low loss photonic integrated circuit with membrane-type photonic crystal waveguides," *Opt. Express* **11**, 2927–2939 (2003).
- [52] L. Yin, Q. Lin, and G. P. Agrawal, "Soliton fission and supercontinuum generation in silicon waveguides," *Opt. Lett.* **32**, 391–393 (2007).
- [53] G. P. Agrawal, *Lightwave Technology: Components and Devices*, (Wiley, 2004).

- [54] D. Dimitropoulos, V. Raghunathan, R. Claps, and B. Jalali, "Phase-matching and nonlinear optical processes in silicon waveguides," *Opt. Express* **12**, 149–160 (2004).
- [55] H. H. Li, "Refractive index of silicon and germanium and its wavelength and temperature derivatives", *J. Phys. Chem. Ref. Data* **9**, 561–658 (1980).
- [56] D. F. Edwards and E. Ochoa, "Infrared refractive index of silicon," *Appl. Opt.* **19**, 4130–4131 (1980).
- [57] L. Yin, Q. Lin, and G. P. Agrawal, "Dispersion tailoring and soliton propagation in silicon waveguides," *Opt. Lett.* **31**, 1295–1297 (2006).
- [58] D. E. Aspnes and A. A. Studna, "Dielectric functions and optical parameters of Si, Ge, GaP, GaAs, GaSb, InP, InAs, and InSb from 1.5 to 6.0 eV", *Phys. Rev. B*, **27**, 985–1009 (1983).
- [59] E. D. Palik, *Handbook of Optical Constants of Solids* (Academic, 1985).
- [60] A. B. Fallahkhair, K. S. Li, and T. E. Murphy, "Vector Finite Difference Mode-solver for Anisotropic Dielectric Waveguides", *J. Lightwave Technol.* **26**, 1423–1431 (2008).
- [61] T. E. Murphy, software available at <http://www.photonics.umd.edu>.
- [62] R. Scarmozzino, A. Gopinath, R. Pregla, and S. Helfert, "Numerical Techniques for Modeling Guided-Wave Photonic Devices", *J. Selected Topics in Quantum Electronics* **6**, 150–162 (2000).
- [63] <http://www.rsoftdesign.com/products.php?sub=Component>
- [64] E. A. J. Marcatili, "Dielectric rectangular waveguide and directional coupler for integrated optics", *Bell Sys. Tech. J.*, 2071–2102 (1969).

- [65] H. Rong, Y. Kuo, A. Liu, M. Paniccia, and O. Cohen, “High efficiency wavelength conversion of 10 Gb/s data in silicon waveguides,” *Opt. Express* **14**, 1182–1188 (2006).
- [66] G. P. Agrawal, *Nonlinear Fiber Optics*, 4th ed. (Academic, 2007).
- [67] Q. Lin, J. Zhang, G. Piredda, R. W. Boyd, P. M. Fauchet, and G. P. Agrawal, “Dispersion of silicon nonlinearities in the near infrared region”, *Appl. Phys. Lett.* **91**, 021111 (2007).
- [68] J. Zhang, Q. Lin, G. Piredda, R. W. Boyd, G. P. Agrawal, and P. M. Fauchet, “Optical solitons in a silicon waveguide,” *Opt. Express* **15**, 7682–7688 (2007)
- [69] J. M. Dudley, G. Genty, and S. Coen, “Supercontinuum generation in photonic crystal fiber,” *Rev. Mod. Phys.* **78**, 1135–1184 (2006).
- [70] J. Zhang, Q. Lin, G. Piredda, R. W. Boyd, G. P. Agrawal, and P. M. Fauchet, “Anisotropic nonlinear response of silicon in the near-infrared region”, *Appl. Phys. Lett.* **91**, 071113 (2007).
- [71] M. Dinu, F. Quochi, and H. Garcia, “Third-order nonlinearities in silicon at telecom wavelengths,” *Appl. Phys. Lett.* **82**, 2954–2956 (2003).
- [72] R. Claps, V. Raghunathan, D. Dimitropoulos, and B. Jalali, “Influence of nonlinear absorption on Raman amplification in silicon waveguides,” *Opt. Express* **12**, 2774–2780 (2004).
- [73] L. Yin and G. P. Agrawal, “Impact of two-photon absorption on self-phase modulation in silicon waveguides,” *Opt. Lett.* **32**, 2031–2033 (2007).
- [74] A. Zwick and R. Carles, “Multiple-order raman scattering in crystalline and amorphous silicon,” *Phys. Rev. B* **48**, 6024–6032 (1993).

- [75] H. K. Tsang and Y. Liu, “Nonlinear optical properties of silicon waveguides”, *Semicond. Sci. Technol.*, **23** 064007 (2008).
- [76] H. K. Tsang, C. S. Wong, T. K. Liang, I. E. Day, S. W. Roberts, A. Harpin, J. Drake, and M. Asghari, “Optical dispersion, two-photon absorption and self-phase modulation in silicon waveguides at $1.5\mu\text{m}$ wavelength”, *Appl. Phys. Lett.* **80** 416–419 (2002).
- [77] G. W. Rieger, K. S. Virk, and J. F. Young, “Nonlinear propagation of ultrafast $1.5\mu\text{m}$ pulses in high-index-contrast silicon-on-insulator waveguides”, *Appl. Phys. Lett.* **84** 900–902 (2004).
- [78] H. Yamada, M. Shirane, T. Chu, H. Yokoyama, S. Ishida, and Y. Arakawa, “Nonlinear-optic silicon-nanowire waveguides”, *Japan. J. Appl. Phys.* **44** 6541–6545 (2005).
- [79] M. A. Foster and A. L. Gaeta, “Wavelength Dependence of the Ultrafast Third-Order Nonlinearity of Silicon,” in *Conference on Lasers and Electro-Optics/Quantum Electronics and Laser Science Conference and Photonic Applications Systems Technologies 2007 Technical Digest* (Optical Society of America, Washington, DC, 2007), paper CTuY5.
- [80] I. Hsieh, X. Chen, J. I. Dadap, N. C. Panoiu, and R. M. Osgood, “Ultrafast-pulse self-phase modulation and third-order dispersion in Si photonic wire-waveguides,” *Opt. Express* **14**, 12380–12387 (2006).
- [81] X. Chen, N. C. Panoiu, and R. M. Osgood, “Theory of Raman-mediated pulsed amplification in silicon-wire waveguides,” *IEEE J. Quantum Electronics* **42**, 160–170 (2006).
- [82] R. Dekker, A. Driessen, T. Wahlbrink, J. Niehusmann, and M. Först, “Ultrafast Kerr-induced all-optical wavelength conversion in silicon waveguides using $1.55\mu\text{m}$ femtosecond pulses,” *Opt. Express* **14**, 8336–8346 (2006).

- [83] J. K. Ranka and R. S. Windeler, “Visible continuum generation in air silica microstructure optical fibers with anomalous dispersion at 800 nm”, *Opt. Lett.* **25**, 25–27 (2000).
- [84] N. Akhmediev and M. Karlsson, “Cherenkov radiation emitted by solitons in optical fibers”, *Phys. Rev. A* **51**, 2602–2607 (1995).
- [85] L. Yin, J. Zhang, P. M. Fauchet, and G. P. Agrawal, “Optical switching using nonlinear polarization rotation inside silicon waveguides,” *Opt. Lett.* **34**, 476–478 (2009)
- [86] V. R. Almeida, C. A. Barrios, R. R. Panepucci, M. Lipson, M. A. Foster, D. G. Ouzounov, and A. L. Gaeta, “All-optical switching on a silicon chip,” *Opt. Lett.* **29**, 2867–2869 (2004).
- [87] T. Liang, L. Nunes, T. Sakamoto, K. Sasagawa, T. Kawanishi, M. Tsuchiya, G. Priem, D. Van Thourhout, P. Dumon, R. Baets, and H. Tsang, “Ultrafast all-optical switching by cross-absorption modulation in silicon wire waveguides,” *Opt. Express* **13**, 7298–7303 (2005).
- [88] Y. Liu and H. K. Tsang, “Time dependent density of free carriers generated by two photon absorption in silicon waveguides,” *Appl. Phys. Lett.* **90**, 211105 (2007).
- [89] G. P. Agrawal, *Applications of Nonlinear Fiber Optics*, 2nd ed. (Academic, 2008).
- [90] Rick Trebino, *Frequency-Resolved Optical Gating: The Measurement of Ultra-short Laser Pulses* (Springer, 2002).
- [91] N. G. Usechak, G. P. Agrawal, and J. D. Zuegel, “FM Mode-Locked Fiber Lasers Operating in the Autosoliton Regime”, *IEEE J. Quantum Electronics*, **41**, 753–761 (2005).

- [92] N. G. Usechak, “Mode Locking of Fiber Lasers at High Repetition Rates”, Ph.D. Thesis, Institute of Optics, University of Rochester, 2006.